DEVELOPMENT OF AN ELECTROCHEMICAL IMMUNOSENSOR FOR THE DETECTION OF STEVIOL GLYCOSIDES BY EXPERIMENTAL AND COMPUTATIONAL METHODS

By:

PHATHISANANI HLOMA

(Reg. No: 21215083)

Submitted in fulfilment of the requirements of the degree of Master of Applied Science in Chemistry in the Faculty of Applied Sciences at the Durban University of Technology

April 2020

DECLARATION

I, **Phathisanani Hloma,** declare that the thesis submitted for the degree of Master of Applied Science in Chemistry at the Durban University of Technology is the result of my investigation and has not already been accepted in substance for any degree and is not being concurrently submitted for any other degree. All the work was done by the author.

Student name **: Phathisanani Hloma**

Student signature

Supervisor name **: Professor K. Bisetty**

Supervisor signature

Co-Supervisor name **: Dr. MI Sabela**

Co-Supervisor signature

Co-Supervisor name **: Dr. S Kanchi**

Co-Supervisor signature

DEDICATION

The author dedicates this thesis to his big family, for their firmly undivided support that they have shown throughout his studies. The big family extends from his grandparents, parents, siblings and cousins, and the great-grandchildren of the "**Xhate** clan, **Xesibe**, **Mganu**, **Malandelwa**, malandelwa yintombi ithi mayizekwe".

The author acknowledges and appreciates the sacrifices made by his family so that he can pursue his dreams and he would like to place it on record that, all that he is doing is for bettering his and their lives.

ACKNOWLEDGEMENTS

I acknowledge the assistance and guidance from different spheres of life for the realisation of this dream, and all praise is directed to GOD, for providing wisdom, strength, and courage to pursue this route.

I would like to wholeheartedly extend my sincere gratitude to my supervisor, Professor K Bisetty, for his constant involvement, support, and direction-giving pieces of advice throughout the project. I am grateful to have been supervised by a profound researcher of his kind. I am gratefully acknowledging my co-supervisors, Dr MI Sabela and Dr S Kanchi, for always making time to assist and guide me throughout the project, their shared experience and support is highly appreciated. I would also like to acknowledge Mrs Mavis Xhakaza, Mrs Mpume Cele, and Miss Avy Naicker, for providing a healthy working environment in the laboratory and assistance while performing experiments.

My acknowledgements extend to all Computational Modelling and BioAnalytical Chemistry (CMBAC) research group colleagues and friends (Lyndon Naidoo, Calvin Harilal, Matshidiso Lephalala, Majola Senzekile, Nomnotho Jiyane and Kwanele Kunene), who have motivated and assisted me countless times throughout my project. I would not be fair not to acknowledge DUT Steve Biko library staff, especially Miss A. Finlayson, for writing assistance and training workshops.

I am forever grateful to my mother and father, **Nonyameko Prelly Hloma** and **Bulelani Emanuel Zimase** and the rest of my family, who have never left my corner with every decision I have taken in my life.

Lastly, the research has been carried out with financial support from the Council of Scientific and Industrial Research (CSIR) and the Durban University of Technology. The authors would like to express their acknowledgment to the Centre for High Performance Computing, an initiative supported by the Department of Science and Technology of South Africa.

ABSTRACT

An electrochemical immunosensor employs antibodies as a capture and detection mechanism to produce an electrical charge for the quantitative analysis of target molecules. The current analytical methods for the separation and detection of stevia glycosides can be tedious in terms of sample preparation and the lack of selectivity. However, electrochemical immunosensors provide selective, sensitive and cost-effective detection routes for these widely consumed sweeteners.

In this study, the author developed an electrochemical immunosensor for the detection and quantification of steviol glycosides, a non-nutritive sweetener widely employed in the food and beverage industries. Most of the artificial sweeteners are low-calorie sweeteners recommended for health-related illnesses. The stability of these sweeteners at even high temperatures has increased their applications in foodstuffs widely. Constant exposure to these sweeteners is somehow associated with health complications, as some are cancer-causing agents. Although there are no reports on stevia glycosides as a health risk sweetener, its widespread use in the food industry needs to be regulated.

Herein, the developed immunosensor was achieved by fabricating the platinum electrodes with graphene oxide (GO) assimilated in Zinc Oxide nanoparticles (ZnONPs) with multiwalled carbon nanotubes (MWCNTs) and immobilized with the human sweet receptor subunit T1R2. The electrochemical detection of the natural sweetening compound, Rebaudioside A (Reb A) was evaluated qualitatively and quantitatively using cyclic and differential pulse voltammetry, respectively under optimised conditions in pH 11 borate buffer from -0.4 V to 0.8 V vs Ag/AgCl.

The GO/MWCNT/ZnONPs nanocomposite was characterized using High-resolution Transmission Electron microscope (HR-TEM), Thermogravimetric Analysis (TGA), Attenuated Total Reflection Mode Fourier transform infrared (ATR-FTIR) and UV-VIS spectroscopy characterization techniques. Also, asymmetric flow-field-flow fractionation and centrifugal flow-field-flow fractionation equipped with a UV-vis and multi-angle angle light scattering detectors were used to separate and characterize the

size distribution of the synthesised ZnO nanostructures. The field flow fractionation (FFF) is one of the efficient separation techniques known, and centrifugal flow field-flow fractionation separates different particle sized nanoparticles by density, thus determining size variation within the synthesised batch. The results obtained using FFF were compared and validated with the conventional characterisation techniques described above.

Computational studies were used to supplement experimental results using docking and adsorption methods. Adsorption studies were carried out to better understand the mechanistic aspects between T1R2, the nanocomposite used to modify the platinum working electrode, and the analyte Reb A. Docking studies between the T1R2 receptor and the steviol glycosides were used to explore the interaction and mechanism of the immunosensor detection.

The results of this study may contribute to the development of an immunosensor that can potentially be used to quantify steviol glycosides in the food and beverage industry.

Keywords: Steviol glycosides; Rebaudioside A; Zinc Oxide Nanoparticles; Human Sweet Taste Receptor T1R2; Density functional theory (DFT); Molecular docking.

TABLE OF CONTENTS

LIST OF TABLES

LIST OF FIGURES

LIST OF ACRONYMS AND SYMBOLS

AF4 : Asymmetric Field Flow Fractionation

anti-TSH : thyroid stimulating hormone antibody

ATD : Amino-terminal Domain

ATR-FTIR : Attenuated Total Reflection Mode Fourier Transform Infrared

AuNPs : Gold Nanoparticles

CE : Capillary Electrophoresis

CF4 : Centrifugal Field Flow Fractionation

C-GPCR : Class C of G-protein coupled receptor

CMEs : Chemically Modified Electrodes

COMPASS : Condensed-phase optimized molecular potentials for atomistic simulation studies

CV : Cyclic Voltammetry

CVD : Chemical Vapour Deposition

DAD : Diode Array Detector

DESI : Desorption Electrospray Ionization

DFT : Density Functional Theory

DPV : Differential Pulse Voltammetry

DSC : Differential scanning calorimeter

E_{pa} : Anodic Peak Potential

E_{pc} : Cathodic Peak Potential

ESI-MS : Electrospray Ionization Mass Spectrometry

FFF : Field Flow Fractionation

GC : Gas Chromatography

GO : Graphene Oxide

hcp : Hexagonal Compact

HPLC : High-Performance Liquid Chromatography

HPTLC : High-performance Thin-layer Chromatography

ICP-MS : Inductively coupled plasma mass spectrometry

I_{pa} : Anodic Peak Current

I_{pc} : Cathodic Peak Current

LC : Liquid Chromatography

LOD : Limit of Detection

LOQ : Limit of Quantification

MAR : Macro-porous Adsorption Resin

MC : Metropolis Monte Carlo

MD : Molecular Dynamics

MM : Molecular Modelling

MS : Mass Spectrometry

MSP : Modified Spray Pyrolysis

MWCNTs : Multi-Walled Carbon Nanotubes

NMR : ..... Nuclear Magnetic Resonance

NPs : ..... Nanoparticles

OP : ..... Organophosphorus

OTA : ..... Ochratoxin A

PLD : ..... Pulsed Laser Deposition

PSA : ..... Prostate Protein Antigen

Pt-E : ..... Platinum Electrode

PVD : ..... Physical Vapour Deposition

Reb A : ..... Rebaudioside A

SFS : ..... Supercritical Fluid Chromatography

SGs : ..... Steviol Glycosides

SP : ..... Spray Pyrolysis

spICP-MS : ..... Single-particle inductively coupled plasma mass spectrometry

STR : ..... Sweet Taste Receptor

Stv : ..... Stevioside

TA : ..... Thermal Analysis

TEA : ..... Triethanolamine

TEM : ..... Transmission Electron Microscope

TGA : ..... Thermogravimetric Analysis

TMD : ..... Transmembrane Helical Domain

TSH : ..... thyroid stimulating hormone

tTG : ..... tissue transglutaminase

UFF : ..... Universal force field

UV-Vis : ..... Ultraviolet/Visible

ZnONPs : ..... Zinc Oxide Nanoparticles

LIST OF CONFERENCES

Oral Presentations

Phathisanani Hloma, *"Synthesis and Characterization Studies of ZnO nanostructures"*, **3rd interdisciplinary research and innovation conference (DUT)**, held at Coastlands on Ridge Conference Centre in Durban between 18 and 20 of September **2018**.

Phathisanani Hloma, *"Synthesis and Characterization Studies of ZnO nanostructures"*, **3rd International Conference on Composites**, Biocomposites and Nanocomposites (ICCBN 2018), held at the Nelson Mandela Bay Stadium in Port Elizabeth, South Africa from 7-9 November **2018**, and formed part of the African Advanced Manufacturing and Composites Show (AAM&CS).

Phathisanani Hloma, *"Synthesis and Characterization Studies of ZnO nanostructures"*, **SACI/ChromSA** postgraduate research colloquium, held at Hotel School, Durban University of Technology, Ritson Campus, Ritson Road on the 6th of March **2019**.

Phathisanani Hloma, *"Development of an electrochemical immunosensor for the detection of steviol glycosides by experimental and computational methods"*, **4th interdisciplinary Research and Innovation Conference**, held at Hilton Hotel, Walnut Rd, Durban, South Africa, between 17 and 20 of September **2019**, for an oral talk on

Poster Presentation

P. Hloma, M.I. Sabela, S. Kanchi, and K Bisetty, *"Development of an electrochemical immunosensor for the detection of steviol glycosides by experimental and computational methods",* **70th Annual Meeting of the International Society of Electrochemistry** in Durban, South Africa, in August **2019**, under the theme *"Trends in Electroanalysis and Low-Cost Electrochemical Sensors"*.

P. Hloma, M.I. Sabela, S. Kanchi, and K Bisetty, *"Development of an electrochemical immunosensor for the detection of steviol glycosides by experimental and*

computational methods", **Faculty of Applied Sciences Research Day 2019** held in Durban, South Africa on the 11th of November 2019.

CHAPTER 1: INTRODUCTION

This chapter provides details about electrochemical immunosensors and deals with the classification of artificial sweeteners, with emphasis on non-nutritive sweeteners, as they are now widely used in the food and beverage industry. Details on the analyte under consideration in this study, steviol glycoside (Rebaudioside A), is presented. The chapter presents the overall aim and objectives, followed by an outline of the thesis.

1.1 Electrochemical immunosensors

Biosensors are compact analytical devices that employ nucleic acids, enzymes, antibodies, animal or plant tissues as sensitive biological elements, for converting the protein-ligand complex electrical signals by immobilizing the recognition elements on the surface of transducers for converting the protein-ligand complex electrical signals. Immunosensors are a subdivision of biosensors. Immunosensors specifically use antibodies or antibody fragments as the sensitive biological elements for the specific analyte (antigen) to form the stable antibody-antigen complexes that are recognized by transducers through concentration-dependent signals (Lim and Ahmed 2016).

Different types of transducers used immunosensors are classified into different types; on that basis, electrochemical immunosensors employ the working electrode as the transducer for measuring the current generated by the redox analyte upon application of voltage. Electrochemical immunosensor's principle of operation is characterized by the three-electrode system consisting of a reference electrode, counter electrode, and the working electrode, where the reaction of interest takes place (Felix *et al.* 2018).

Immunosensors find significant applications in different fields, and the food industry has now substantially relied on the application of electrochemical immunosensors as these have an ability to provide specificity, rapid and inexpensive determinations of

pathogens and other food-based electro-active species in food. Researchers have paid great attention in the modification of working electrode surfaces (transducers) of electrochemical immunosensors in this regard, novel nanomaterials such as carbon nanotubes, graphene and metallic nanoparticles are used to increase the sensitivity of the developed immunosensor. This study was based on developing an electrochemical immunosensor for the detection of Rebaudioside A in food samples by employing Pt/ZnONPs/GO/MWCNTs/T1R2 nanocomposite.

1.2 Background and Problem Statement

Stevia rebaudiana Bertoni is a herbaceous perennial plant of the family Asteraceae and is indigenous to Paraguay and Brazil. The leaf extract of *Stevia rebaudiana* is used in Japan, Korea and South America to sweeten soft drinks, soju, soya sauce, yoghurt and other foods, whereas in the United States it is used as a dietary supplement. The Rebaudioside A (Reb A) is a major low-calorie diterpene steviol glycosides in the leaves of *Stevia rebaudiana* (Wingard *et al.* 1980; Jaitak *et al.* 2009). Reb A is a glycoside that contains only glucose as its monosaccharide moiety. It contains four glucose molecules in total, with the central glucose of the triplet connected to the main steviol structure at its hydroxyl group, and the remaining glucose at its carbonyl group forming an ester functional bond. The leaves of *Stevia rebaudiana* is known to contain more than 35 *ent*-kaurene-type diterpene glycosides, with these diterpene glycosides (Reb A) together with Stevioside (Stv) are in abundance compared to other types of stevia glycosides (Bathinapatla *et al.* 2016).

In the food industry it is confirmed that the detection of steviol glycosides (SGs)has primarily been based on the chromatographic techniques such as high-performance liquid chromatography (Woelwer-Rieck *et al.* 2010), high performance thin layer chromatography, hydrophilic interaction chromatography (Liang *et al.* 2015), liquid chromatography mass spectrometry (Gardana *et al.* 2010). Specifically, capillary electrophoresis is used to generate charged species by using applied voltage within the capillary, thus resulting in the separation of analytes based on different mobilities (Bathinapatla *et al.* 2016). The techniques mentioned above are sensitive, but they are

subjected to high solvent consumption and less selectivity. As a result, this has prompted studies involving electrochemical techniques.

Electrochemical techniques counteract the disadvantages of the fundamental techniques, as it is possible to develop a sensor that is faster, less expensive, sensitive and selective to a compound of interest. This study is aimed at developing an electrochemical immunosensor with electrocatalytic activity and conductivity by fabricating a nanocomposite onto a bare rotating disc platinum electrode (Pt-E). Electrode modifications have gained widespread recognition lately. Accordingly, the proposed immunosensor will be designed with T1R2/ZnONPs-MWCNTs/GO nanocomposite. The MWCNTs are highly electro-conductive and characterized by a large surface area with excellent chemical and physical stabilities (Yu *et al.* 2015). They also act as good support for the preparation of nanocomposites using materials such as GO and ZnONPs. The selectivity of the proposed immunosensor will be achieved by converting the bare electrochemical sensor into an electrochemical immunosensor by immobilizing the human sweet taste receptor subunit T1R2 onto the nanocomposite coated on the surface of the bare platinum electrode. Human sweet taste receptor (STR) is a heterodimer composed of two subunits, T1R2 and TIR3 which belongs to class C of G-protein coupled receptor (C-GPCR) family. Sucrose, glucose, sucralose and related sugars bind to active sites of ATD of both T1R2 and T1R3 subunits, whereas dipeptidyl sweeteners such as aspartame, neotame bind only to ATD of T1R2 and can be considered as an orthostatic agonist (Mayank and Jaitak 2015).

The results of this study will contribute to the development of an immunosensor that can potentially be used to quantify steviol glycosides in the food and beverage industry. This research will form the basis for further research and development in this area which can lead to the design of a portable *in-situ* monitoring device.

Computational chemistry is utilized in this study to understand the molecular-level behaviour of the system and to validate the experimental outcomes. Computational studies provided a better, detailed understanding and visualization of the interaction phenomena used to validate the experimental studies and to investigate the structural,

electronic, and vibrational properties of the molecular system, as well as the molecular behaviour when subjected to different reaction mediums. The computational studies provided a better understanding of the interaction phenomena used to validate the experimental studies and to investigate the molecular properties of the system (structural, electronic, and vibrational) as well as the molecular behaviour under certain conditions.

The computational aspect ranged from construction of nanostructures used for electrode modification in the development of the immunosensor, and Forcite-Geometry-based structural analysis, density functional theory (DFT) calculations, molecular dynamics (MD) simulations and Metropolis Monte Carlo (MC) adsorption studies.

1.3 Aim and objectives

This study is aimed at developing a novel and selective electrochemical immunosensor for the detection of steviol glycosides in selected food beverages experimentally and to use computational chemistry to understand better the interactions between the nanomaterial used for electrode fabrication and the analyte of interest (Steviol Glycoside).

Objectives

- To hydrothermally synthesize Zinc Oxide Nanoparticles (ZnONPs).
- To characterize the newly synthesized Zinc Oxide nanoparticles using UV-Vis spectroscopy, Transmission Electron Microscope (TEM), Attenuated Total Reflection Mode Fourier Transform Infrared (ATR-FTIR), Thermogravimetric Analysis (TGA), and Field Flow Fractionation (FFF) in asymmetric mode (AF4).
- To prepare nanocomposite of GO/MWCNTs/ZnONPs/T1R2 step by step and fabricate the surface of the platinum working electrode.
- To optimize experimental parameters (such as pH, Scan rates, Deposition time and Deposition Potential) for the immunosensor development.
- To analyse Reb A electrochemically by employing cyclic voltammetry or qualitative determination and by employing differential pulse for quantifying Reb.

- To perform validation of electrochemical results with computational results in terms of adsorption and docking methods to assess the interaction between the sweet taste receptor (T1R2) and steviol glycosides.

1.4 Thesis outline

Following **Chapter 1**: Introduction, the remaining chapters of this thesis are outlined below:

Chapter 2: In this chapter, steviol glycosides' properties and major components are explained in detail, with the analytical techniques used for their detection entailed. The chapter also discusses biosensing methods used for the detection of steviol glycosides and different methods employed for the synthesis of ZnO nanostructures.

Chapter 3: This chapter details the theoretical principles of experimental and computational chemistry employed in this study. It is in this chapter that computational chemistry's interdependency to experimental work is explained.

Chapter 4: Experimental and computational methodologies are presented in this chapter, experimentally this includes methodologies for the synthesis of zinc oxide nanoparticles, construction of the immunosensor for the detection of Reb A in various food samples, electrochemical characterization of the developed immunosensor and interference studies. This chapter acquaints the reader with the computational methodologies undertaken in this study.

Chapter 5: This chapter presents experimental and computational results, with synergies between the two sets of results discussed and interpreted. Characterization findings for the nanomaterial used for fabricating the immunosensor are presented and discussed into detail in this chapter and lastly the chapter details electrochemical behaviour of the developed immunosensor on Reb A.

Chapter 6: This chapter highlights major findings both experimentally and computationally, with entertaining trends and synergies between experimental and

computational results, concluding remarks are proposed. The chapter also recommends future work on the electrochemical determination of Reb A, emphasising in the application of the developed immunosensor.

References: The references used in this thesis are enclosed.

CHAPTER 2: LITERATURE REVIEW

This chapter highlights the overview of steviol glycosides and their chemical and physical properties with applications mostly in the food and health industries. A review of the electrophoretic and chromatographic techniques primarily used for qualitative and quantitative purposes of steviol glycosides is discussed. Additionally, current trends in the electrochemical detection of steviol glycosides, including electrochemical immunosensor development, are presented here. This review is aimed at novel applications of nanomaterials and antibodies used for the development of an immunosensor.

2.1 Steviol Glycosides

Non-nutritive sweeteners are low-calorie substances used to replace sugar and other caloric ones. Determination of these sweeteners in foods is important to ensure consistency in product quality. These sweeteners help control the body weight and insulin levels as they provide no or little calories (Yang and Chen 2009).

Stevia rebaudiana is a herbaceous perennial plant that has been in existence for hundreds of years now, and Guarani Indians have been using this Paraguay and Brazil native plant as a natural sweetener for years (Jaitak *et al.* 2009). Facilities have now been put in place for farming *Stevia rebaudiana* in several countries such as Asia, Canada, China, Brazil and Paraguay.

Apart from *Stevia* extracts having therapeutic, hypoglycaemic, and hypotensive properties, they contain a high level of sweetening compounds, known as steviol glycosides, contributing to the antioxidant, antimicrobial and antifungal activities(Mayank and Jaitak 2015). *Stevia* consists of more than 150 species, but amongst that, only *Stevia rebaudiana* is wildly applied in the food industry as they are

the only ones possessing sweetening properties. The steviol glycosides are natural sweeteners, with organoleptic properties and consist of multiple ent-kuarene diterpene glycosides, extracted from *Stevia rebaudiana* (Bertoni) which belongs to the Asteraceae family. *Stevia* sweeteners are obtained from the leaves of *Stevia species*. It is extracted with hot water, and the extract is passed through an adsorption resin to trap and concentrate the steviol glycosides.

These compounds are approximately 400-600 times sweeter than sugar and are thermally stable even at temperatures of up to 200 ^{0}C, making them suitable for the use in cooked foods (Kroger *et al.* 2006). The frequently increased application of Reb A as a sweetener requires controlled safety in foodstuffs (Zygler *et al.* 2009).

Out of the whole composite of the *Stevia* leaves, 6 to 10% is made up of Stevioside, 2 to 4% is taken up by rebaudioside A, and the other minor steviol glycosides compensate for 1 to 2% of the total 16% SGs in *stevia* extracts.

2.1.1 Properties of Steviol Glycosides

Nowadays steviol glycosides are one of the researched compounds, these compounds find application in many different fields. Steviol glycosides are readily available as they are obtained from plants. SGs are wildly used in the food and health industry because of their high intensity sweetening properties and the health benefits(Jaitak 2015; Mayank and Jaitak 2015)

2.1.2 Rebaudioside A

The Joint Expert Commission for Food Additives stated that 2 to 4 mg/kg body weight is the acceptable daily intake of steviol glycosides (Bathinapatla *et al.* 2016). Steviol glycosides (SG's) are extracted from *stevia rebaudiana* leaves, with Rebaudioside A being one of the significant constituents of SG's (Figure 2.1). Economic and Scientific's interests have been attracted by "Sweet Leaf", as Reb A is famously known owing to its non-nutritive sweetening ability and therapeutic properties.

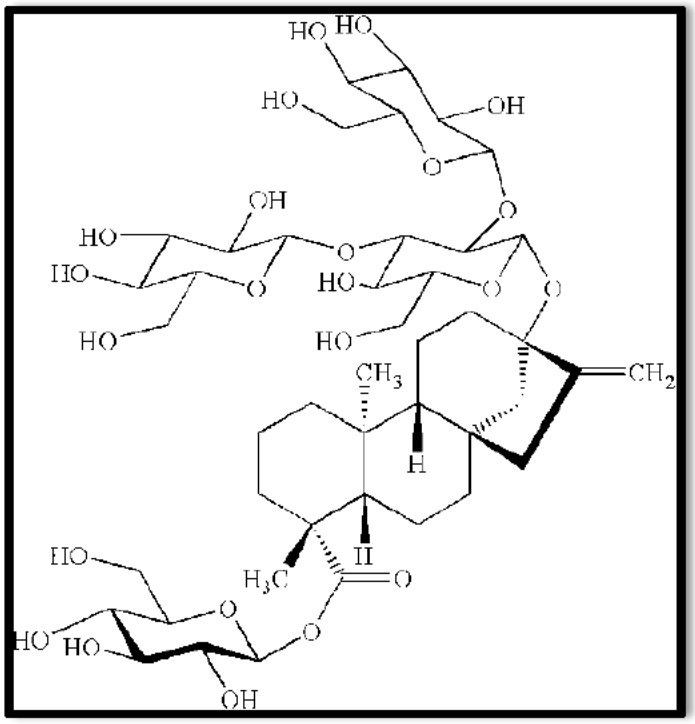

Figure 2-1: Showing chemical Rebaudioside A, a high potency diterpenoid glycoside Sweetener(Carakostas *et al.* 2008).

Reb A's extraction and isolation are from the *stevia rebaudiana* plant as it is with the other coexisting steviol glycosides. When compared to sucrose, *stevia* extracts are said to be 3 to 300 times sweeter. Hence they are the alternatives as non-nutritive sweeteners (Prakash *et al.* 2015).

2.2 Separation methods for the detection of Reb A

The presence of steviol glycosides in food beverages raises a matter of concern for the quality assurance departments as the consumption of these beverages is on the increase, and the number of steviol glycosides consumed must be regulated. Literature survey reveals that chromatography and capillary electrophoresis are widely used in the determination of artificial sweeteners in food technology (Woelwer-Rieck *et al.* 2010; Pavlíček and Tůma 2017). Liquid chromatography (LC) has been the most popular choice for the determination of the sweeteners (Samah *et al.* 2013). However,

only a few are suitable for the simultaneous determination of several sweeteners. Because the physicochemical, electrochemical, and spectral properties of the non-nutritive sweeteners are significantly different, a method for the simultaneous determination of the components is always restricted. Although the high-performance liquid chromatographic methods have high separation efficiency, their sensitivity is compromised (Yang and Chen 2009).

Steviol glycosides are a group of chemical species closely resembling each other due to the similarities in their functional groups and chemical behaviour. Chromatography is one of the wildly powerful techniques used for separating such species, from there chromatographic separations of these species can provide qualitative information about the species of interest and lately the separated species can be quantified (Skoog *et al.* 2013). Chromatography is a separation technique, in which the separation of different components of a mixture is based on their relative speeds of the components as they are carried through a stationary phase by a gaseous or liquid mobile phase.

Steviol glycosides are mainly separated using column chromatography. Chromatography is classified into two types, mainly column chromatography and planar chromatography. In column chromatography, the stationary phase is stashed and held in a very narrow tube, and for the separation of different compounds of interest, the analyte caring mobile phase is forced through the tube by applying pressure using gravity. On the other hand, planar chromatography also separates components on a stationary phase supported on a flat plate or on the pores of a paper, carried by the mobile phase where no pressure is applied, and capillary action and gravity influence are at play. Examples of column chromatography include but not limited to, gas chromatography (GC), liquid chromatography (LC), high-performance liquid chromatography (HPLC) and supercritical fluid chromatography (SFS). HPLC is found to be the most widely used technique for separating and quantifying steviol glycosides (Reb A), where the instrument is coupled to various detectors such as Ultraviolet/visible (UV-Vis) detector (Samah *et al.* 2013), diode array detector (DAD) (Liang *et al.* 2015), and mass spectrometric (MS) detectors (Shafii *et al.* 2012).

Capillary electrophoresis is also reported as the separation technique used for separating and quantifying steviol glycosides coupled to various types of detectors such as diode array detector (Ayyappa *et al.* 2015). Electrophoresis is a macro size separation technique that is based on the different mobilities/rates of migration that the charged species have in an applied dc electric field. Scientists rely on the strength of electrophoresis with its unique ability to separate charged macromolecules under analysis. Capillary electrophoresis was introduced whereby these macromolecule separations were performed in micro amounts of the sample in a fused silica capillary cube, bringing in more resolution, less time for analysis and a room for automation. Appendix A tabulates different analytical procedures for simultaneous determination of Rebaudioside A in samples of different food products.

Clearly, the techniques mentioned above are sensitive, but they are subjected to high solvent consumption and less selectivity; as a result, this has prompted studies involving electrochemical techniques. Recent developments have been made in the detection of Reb A electrochemically (Bathinapatla *et al.* 2016). Electrochemical techniques counteract the disadvantages of the fundamental techniques as it is possible to develop a sensor that is faster in response time, low cost, sensitive and selective to that compound of interest. This study was aimed at developing an electrochemical immunosensor with electrocatalytic activity and conductivity by immobilizing a nanocomposite (GO/MWCNTs/ZnONPs/T1R2) onto a bare rotating disc platinum electrode for detecting Rebaudioside A in food samples. Appendix A: Table 2-2 highlights and briefly describes methods that have been reported for the determination of Reb A and other major steviol glycosides.

2.3 Biosensing Methods

2.3.1 Immunosensors

The monitoring of the amount of biological (pathogenic bacteria) and chemical contaminants in food is of high importance for both food safety and quality. In recent developments, the analysis of such compounds is replaced with biosensors, instead of the sophisticated hyphenated techniques (Bathinapatla *et al.* 2016). Biosensors are compact analytical devices that rely on transducers for the detection and conversion of electrical signals that are resulting from antigen-antibody complexes for processing, recording, and displaying (Moina and Ybarra 2012).

Biosensors employ enzymes, nucleic acids, animal or vegetable tissues, and antibodies as sensitive biological elements, immobilized on the surfaces of transducers. The above-explained compact devices are called immunosensors when antibodies or antibody fragments are utilized as the sensitive biological element for the specific analyte (antigen) to form the stable antibody-antigen complexes that are recognized by transducers (Ricci *et al.* 2007). Depending on the type of transducer that is used, this can divide immunosensors into different types being electrochemical, optical and piezoelectric immunosensors, which are briefly discussed below.

The formation of the antibody-antigen complex is the principle of operation under which an immunosensor significantly depends on, and this period is termed incubation time. The incorporation of nanoparticles instead of bare antibody immobilization into the surface of the working electrode in the case of electrochemical immunosensors has proven to decrease incubation time. This inclusion of nanomaterials consequently improves the overall performance of the immunosensor (Cheemalapati *et al.* 2013).

This study developed an electrochemical immunosensor employing human sweet taste receptor (STR) subunit T1R2 as the sensitive biological element for the detection of Reb A where surface of the transducer (Pt electrode) was fabricated with graphene oxide (GO), assimilated in Zinc Oxide nanoparticles (ZnONPs) with multiwalled carbon nanotubes (MWCNTs).

2.3.1.1 Components of an Immunosensor

The components of the biosensor (Figure 2.2) concurrently work together in collecting, transmitting and converting the chemical or biological information into an understandable signal. A typical immunosensor is composed of a transducer, sensitive biological element and signal processing unit. The transducers have to recognize and measure the chemical changes or property changes that occur when the sensitive selectively binds with the analyte of interest, forming stable enzyme-substrate, antibody-antigen and stable complexes.

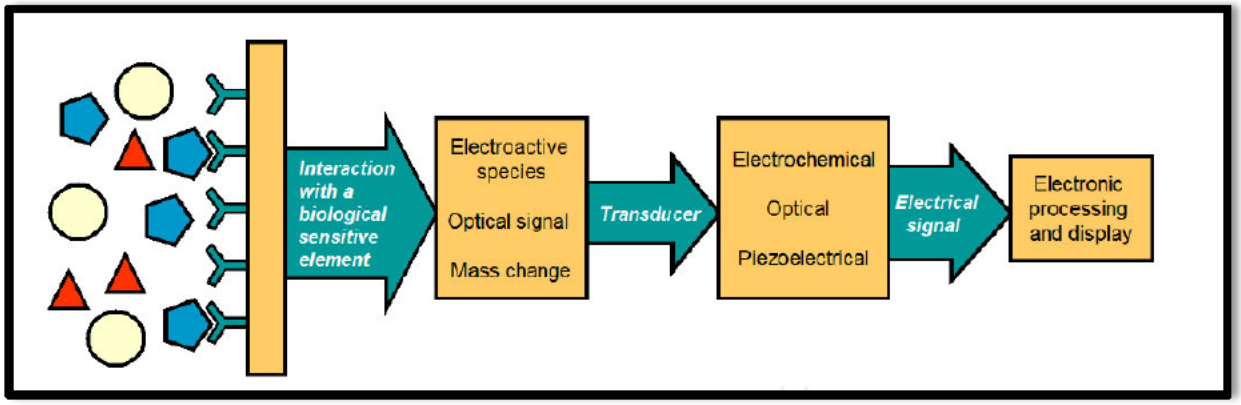

Figure 2-2: Schematic representation of components of a biosensor working in conjunction with each other (Moina and Ybarra 2012).

2.3.1.2 Types of Immunosensors

(i) Electrochemical Immunosensors

Electrochemical immunosensors are voltammetric techniques relying on measuring current because of varying the applied potential in a specific range; as a result, these are known as amperometric measurements. Electrochemical immunosensors function based on the three-electrode system consisting of the working electrode as a transducer to measure the current resulting from the redox reactions at specific potentials.

Amongst the three types of immunosensors discussed in this study, due to their unique characteristics such as low-cost, robustness, fast time of response, low sample

volumes required, easiness and sensitivity, electrochemical immunosensors have been prominently applied more than the other discussed types (Felix *et al.* 2018).

(ii) Optical Immunosensors

As explained previously, the difference in transducer response from the interaction of the target analyte with the sensitive biological element will depict which type of immunosensor is being studied. In optical immunosensors, the transducer interprets the response from antibody-antigen complex/interaction by form an optical signal, and this is usually the resultant change in optical properties such as emission, refractive index, absorbance, reflectance and optical path (Moina and Ybarra 2012). The information gathered by the transducer is measured in terms of photons (Borisov and Wolfbeis 2008).

(iii) Piezoelectric Immunosensors

Piezoelectric transducers incorporate quartz microbalances and microcantilevers, to measure any mass change due to the formation of the antibody-antigen complexes. The quartz crystal is highly precise and oscillator for measuring mass changes occurring from immunological reactions(Ricci *et al.* 2007).

2.3.1.3 Cytochrome c modified nanocomposite electrochemical biosensor

According to literature studies, (Bathinapatla *et al.* 2016) developed an ultrasensitive novel biosensor for the detection of Reb A in different food samples. Cytochrome C is the sensitive biological component immobilized on platinum fabricated with graphene oxide assimilated with gold nanoparticles decorated with multi-walled carbon nanotubes. The developed biosensor was able to detect Reb A down to 0.075–1.25 mM.

2.4 Nanoparticles used in this study

2.4.1 Zinc oxide nanoparticles

Nanotechnology has received significant attention over the past decade. Nanoparticles (NPs) with a smaller size ranging from 1 nm to 100 nm have unique physical and chemical properties. Due to the presence of greater reactive sites, NPs are more chemically active compared to their bulk counterparts (Sharma *et al.* 2018). The size and morphology of the desired NPs are determined by the employed method for their synthesis. Hence these have a direct effect on the biological properties the NPs possess (Javed *et al.* 2017).

The methods employed for the synthesis of NPs for different metals are not limited to but include polyol and solvothermal synthesis (Alves *et al.* 2018), wet chemical synthesis (Samanta 2017), pyrolysis method (Saravanakkumar *et al.* 2018), and hydrothermal synthesis (Saleh *et al.* 2017). In this study, Zinc oxide nanoparticles (ZnONPs) are successfully synthesized by employing an electric pressure-assisted hydrothermal synthesis on Zinc gluconate precursor (Laber *et al.* 2016).

Semiconductor metal oxide NPs is a subsection in nanotechnology given immense focus due to their undesirable optoelectronics, drugs delivery, environmental monitoring, control of chemical processes, photocatalysis, energy storage and biomedical diagnosis properties (Ahmad *et al.* 2011; Kumar *et al.* 2015).

2.4.1.1 Basic properties of Zinc oxide nanoparticles

Zinc oxide crystallizes into three different forms, hexagonal wurtzite, sphalerite structure and halite (assembling sodium chloride (NaCl)). ZnO crystals in wurtzite form are favoured in terms of thermodynamic stability compared to the other forms and possess the following lattice parameters where a = 3.2495 Å and c = 5.2069 Å in a hexagonal compact (hcp) structural arrangement, based on p63mc space group, shown in Figure 2.3 below (Alves *et al.* 2018).

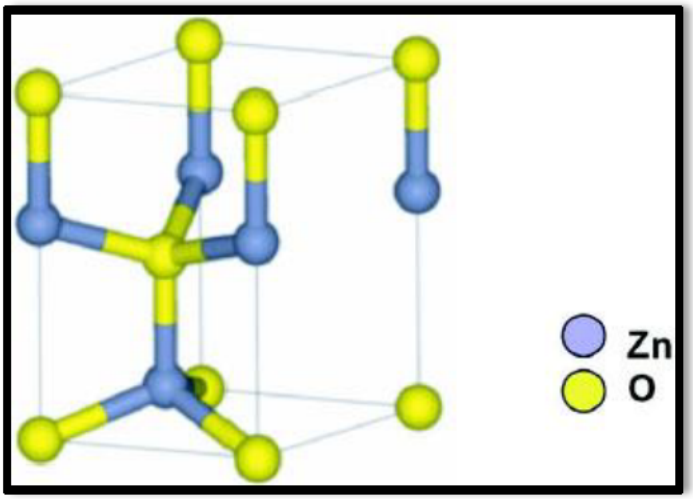

Figure 2-3: ZnO wurtzite crystal structure (Samanta 2017).

Zinc oxide is a semiconductor known for intrinsic structural defects due to atomic vacancies, this feature, size control, and morphology can be manipulated in ZnONPs synthesis and used to scientific researcher's advantage (Becheri *et al.* 2008). The wurtzite ZnO structure is highly polar due to Zn^{2+} cation surrounded by four O^{2-} anions. Given all the above properties, chemical reactions can be employed with thermodynamics conditions to favour certain route growths to achieve ZnONPs with the desired shape and sizes, in turn, this understanding of controlling parameters is utilized in this study for synthesizing ZnONPs for electrochemical sensing applications(Alves *et al.* 2018).

2.4.1.2 Mechanical properties of Zinc oxide nanoparticles

Zinc nanoparticles are regarded as one of the nanomaterials possessing exceptional mechanical strengths and more than singular study has confirmed a significant boost in mechanical properties of nanosized materials compared to their bulk counterparts (Yadav *et al.* 2006).

2.4.1.3 Electrical properties of Zinc oxide nanoparticles

Zinc oxide is characterized by a bandgap of 3.37 eV, due mainly to the doping effects near the UV region and at room temperature exhibits a high excitonic binding energy of 60 meV (Sirelkhatim *et al.* 2015).

2.4.1.4 Different synthesis types of Zinc oxide nanoparticles

(i) Sol-gel Method

Sol-gel is a chemical procedure with a constant formation of a diphasic gel-like liquid and solid phase resulting from initial colloidal (Sol) solution conversion. In this process, sedimentation and centrifugation are used to accelerate the rate of phase separation producing morphologies ranging from discrete to continuous polymer networks. Sol-gel for synthesizing zinc oxide nanoparticles is not only famous for being cheap, reliable, repeatable and simple to perform when well equipped, but produces zinc oxide nanoparticles with good optical properties (Vafaee and Ghamsari 2007). Vafaee and colleagues reported a sol-gel synthesis of zinc oxide for the first time in which triethanolamine (TEA) was used as a surfactant producing particle size of 3 nm and 4 nm.

(ii) Atomic Layer Deposition Method

The atomic layer deposition method (Figure 2.4) of nanomaterial synthesis utilizes gaseous metal precursors to produce films on substrates post-exposure to these gaseous species, unlike vapour deposition procedure, in this method, the metal precursors are never present in the reaction vessel at the same time.

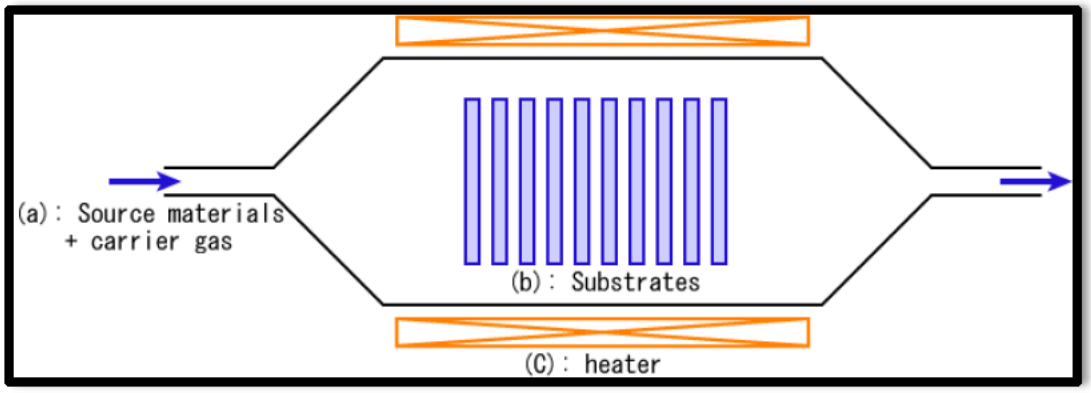

Figure 2-4: Schematically representation of thermal chemical vapour deposition method of nanomaterial synthesis (Midson *et al.* 2017).

Instead, these are introduced individually and non-overlapping. Nano-thick zinc oxide nanofilms were successfully coated for UV-absorption applications on silicon dioxide and titanium dioxide nanoparticles using a fluidized bed reactor (King *et al.* 2008).

(iii) Vapour Deposition Method

The vapour deposition method is categorized into physical vapour deposition (PVD) or chemical vapour deposition (CVD), employed to produce high-performance and high-quality solid materials under vacuum, with semiconductor industry using it for production of thin films. Gas-phase synthesis of nanoparticles provides numerous advantages compared to other methods but are least understood and employed, CVD, in particular, provides a researcher with better control in particle morphology and crystallinity (Polarz *et al.* 2005).

The easily accessible $[CH_3ZnOCH(CH_3)_2]_4$ volatile organometallic precursor of Zinc was employed for synthesizing zinc oxide nanoparticles with controlled morphological and crystallinity properties, allowing a detailed gaseous view of agglomerates formation (Polarz *et al.* 2005).

(iv) Co-Precipitation Method

Wet chemical methods are cost-effective, easy to perform and easily repeatable where the growth of the metal nanostructures is occurring at lower temperatures prone to structural defects (Samanta 2017).

(v) Electrodeposition Method

Recently, electrodeposition methods involving electroplating have emerged as an exciting method of application for the synthesis of nanomaterials. Electrodeposition principle depends on the electrolysis of metals or alloys on conductive surfaces in the presence of an electrolyte (Jayakrishnan 2012). Zinc carbonate and zinc oxide nanoparticles were electrochemically synthesized, where parameters such as the concentration of zinc precursor in an electrolyte solution, sweep rate of the electrolyte and its composition during electrodeposition process, the range of the applied voltage had a direct influence on the desired particle size deposited (Pourmortazavi *et al.* 2015).

(vi) Pulsed-Laser Deposition Method

Pulsed laser deposition (PLD) method in contrast to other deposition methods provides numerous advantages in producing nanoscale thin films and nanoparticles. This is attributed to the fact that the films deposit at an atomic rate and the slow film growth allows more variable control resulting in nanofilm deposition (Zawadzka *et al.* 2016).

(vii) Spray Pyrolysis Method

A conventional spray pyrolysis (SP) technique for nanomaterial requires costly equipment, and this was prone to limitations as one could only obtain thin films or nanoscale particles if the spraying were done on glass or transparent substrate. Saravanakkumar D and colleagues overcame the conventional spray pyrolysis limitations when synthesizing hybrid ZnO-CuO nanocomposites powders, by spraying the solution on a hot copper plate and later studying the antimicrobial properties of the hybrid nano-powders, referred to as a modified spray pyrolysis (MSP)s method (Saravanakkumar *et al.* 2018).

2.4.1.5 Applications of Zinc oxide nanoparticles

Zinc oxide is widely known for possessing chemical stability, non-toxicity and therefore, many research areas such as catalysis, gas sensing technology, dye-sensitized solar cells, ultraviolet emitting diodes, and photovoltaic devices employ zinc oxide. Cosmetic industries employ zinc oxide nanofilms as UV-absorbers in manufactured sunscreens, and the literature reveals a method for successfully using a fluidized reactor bed for coating titanium and silicon dioxide nanoparticles with nanofilms of zinc oxide (King *et al.* 2008). The textile industry has been in the study to enhance fabric properties where acrylic binders were employed to immobilize zinc oxide nanoparticles onto the surface of the fabrics. The nanoparticle functionalized fabric showed vast UV-absorbing properties(Yadav *et al.* 2006). Due to nano photocatalysis properties of ZnONPs, these structures are widely used in the cement industry as an additive to improve the setting time of concrete materials and facilitate hydration (Nochaiya *et al.* 2015).

Electrochemistry researchers are currently capitalizing on developing sensitive and selective chemically modified electrodes (CMEs) by the inclusion of nanomaterials

such as zinc oxide nanoparticles, redox and conductive polymers for determination electro-active compounds in different fields(Karimi-Maleh *et al.* 2016). Hybrid zinc oxide-multiwalled carbon nanotube electrochemical sensors developed for food technology applications, mainly used low-calorie artificial sweeteners, with relatively low detection and quantification limits compared with the unmodified electrode (Balgobind *et al.* 2016).

This study exploits the previously detailed properties of ZnONPs with incorporation of graphene oxide and human taste receptor T1R2 anchored on multi-walled carbon nanotubes, by developing a novel electrochemical immunosensor for the detection of the relatively abundant steviol glycoside, Rebaudioside A (Reb A).

2.4.2 Binding Agents

The immobilization of antibodies and enzymes onto surfaces of chemically modified electrodes, require stabilization of these sensitive biological elements to be adsorbed onto the surface. The treatment of a modified surface or modifying nanomaterials with a crosslinking agent is also characterised binding agents.

Glutaraldehyde can react with several functional groups of proteins, such as amine, thiol, phenol, and imidazole because the most reactive amino acid side-chains are nucleophiles and because of that, the linear 5-carbon dialdehyde has found applications as enzyme immobilisation. The achievement of stable crosslink with proteins/enzymes significantly depends on crosslinking agent/enzyme ratio, the pH of immobilization, and a general understanding of the mechanism followed by the crosslinking agent to produce stable crosslinking/enzyme intermolecular crosslinking instead of intramolecular links(Migneault *et al.* 2004).

Glutaraldehyde is still wildly used as the crosslinking agent; recently glutaraldehyde's crosslinking abilities were tested on characteristics of chitosan-based films that were alkaline post-treated (Frick *et al.* 2018), whereas on another study different concentrations of genipin and glutaraldehyde were varied in checking their crosslinking characteristics (Liu *et al.* 2019). In biosensing technology, glutaraldehyde was recently used as a crosslinking agent in biosensing detection of organophosphorus (OP) pesticides (Pundir and Malik 2019).

In most cases, the crosslinking agents are nucleophilic and attack electron-deficient functional groups the proteins or enzymes inducing covalent bonding; besides glutaraldehyde, there are other organic compounds useful for the same process. Formaldehyde has been known to crosslink proteins to proteins and proteins to DNA. The crosslinking ability of formaldehyde is attributed to its dipole nature with nucleophilic carbon. The compound (Formaldehyde), forms protein-DNA, protein-protein intermediate as it readily reversely attacks functional groups (amines) in proteins/DNA (Kaufman *et al.* 2000).

Recently, to study protein-protein interactions through capillary electrophoresis, the crosslinking capabilities of formaldehyde were compared with those of glutaraldehyde (Ouimet *et al.* 2018). The small size advantage of formaldehyde and its dual functionality permits it to crosslink macromolecules up to approximately 2 Å (Ramanathan *et al.* 2019). These bifunctional crosslinkers such as Glutaraldehyde (Dialdehyde molecule) have advantages such as high specific activity and less contamination or interference from support material as it is possible for their application without the support material (Velasco-Lozano *et al.* 2016).

N-hydroxysuccinimide (NHS) esters are also widely employed organic compounds in promoting covalent interactions with proteins and ligands in question through amine bonding (Kalkhof and Sinz 2008). Immunosensor development solely depends on stable immobilization of the molecular recognition elements, which is achieved by the inclusion of cross-linking agents.

2.4.3 Antibodies

Any sensor specificity is achieved by immobilisation of a molecular recognition element that reacts exclusively with the analyte of interest. In immunosensor development, *antibodies* are the most utilized molecular recognition elements since these are proteins with specificity towards the analyte and are immobilized on the surface of the electrode through different techniques such as covalent attachment, polymer entrapment, adsorption and many other. **Appendix B** shows A summary of antibodies employed in electrochemistry for development of immunosensors

2.4.3.1 T1R2 G analyte coupled receptor

Receptors are chemical message carriers made up of proteins. The classification of receptors depends on their location and on whether they relay, integrate or amplify the chemical signal in biological systems (Huang *et al.* 2019). G-Protein linked hormone receptors and ion-channel linked receptors are classified as transmembrane receptors.

Class C of G-protein coupled receptor (C-GPCR) family comprising two subunits heterodimers T1R2 and T1R3 make up the human sweet taste receptor (STR) (Jaitak 2015). T1R2 as one of the dominant subunits of STR uses the extracellular cysteine-

rich domain (CRD) that is common to all classes of C-GPCR in aid of joining its large amino-terminal domain (ATD) to a seven-transmembrane helical domain (TMD).

The large amino-terminal domain of T1R2 holds 500-600 residues together with binding sites of different functionalities to the ligands. Food and pharmaceutical industries are making steviol glycoside relevant for their application as sweeteners, with dipeptidyl sweeteners covalently binding selectively to the binding sites T1R2 subunit of STR through hydrogen bonding. In this study, citing from (Jaitak 2015), the antibody is then applied as a molecular recognition element in developing an electrochemical immunosensor for the detection of Rebaudioside A in food samples.

CHAPTER 3: THEORETICAL PRINCIPLES

This chapter focuses on the theoretical principles underlying the experimental and computational methods employed in this work. A description of the broad range of characterisation tools, including electrochemistry tools is described. In addition, the theoretical principles underlying Field Flow Fractionation (FFF), undertaken for the first time are discussed in this chapter.

The supporting role of computational chemistry in the construction of an electrochemical immunosensor is highlighted. Furthermore, the equations and rigorous foundation of three foremost quantum chemical methods, i.e., density functional theory (DFT), Metropolis Monte Carlo (MC), and molecular dynamics (MD) simulations, are presented.

3.1 Experimental characterisation techniques

3.1.1 Electrochemical techniques

Electrochemical techniques rely on the measurement of potential, charge, or current for quantitative analysis where analyte concentration is determined and for qualitative analysis where the analyte's chemical reactivity is investigated.

3.1.1.1 Cyclic voltammetry

Voltammetric methods are electroanalytical techniques that mainly depend on measuring the current of the system as the applied potential. Voltammetry measures the current of the electrochemical cell, where the rate of oxidation or reduction of the analyte is limited by the rate of mass transfer of that analyte from the solution (supporting electrolyte) to the surface of the working electrode.

Cyclic voltammetry (CV) is one of the most common electroanalytical techniques seldom used in quantitative analysis but finds its wide utilization in qualitative studies

such as oxidation/reduction reactions, the detection of reaction intermediates and studying the properties of the products formed at electrodes (Skoog *et al.* 2013). In a typical Cyclic voltammetry experiment, the current is measured while the potential is first ramped in one direction, and then the potential is ramped in the opposite direction, this mentioned current here is that of the working electrode which is at rest in a closed electrochemical cell purged by the inert gas. The properties of the analyte and the composition of the sample determines the direction of the potential scan, forward scan is obtained when the current is ramped to more negative potentials while reverse scan is obtained in the opposite direction, this, in turn, produces a cyclic voltammogram with significant parameters for qualitative distinction, such as cathodic and anodic peak potentials, and cathodic and anodic peak currents, shown in Figure 3.1.

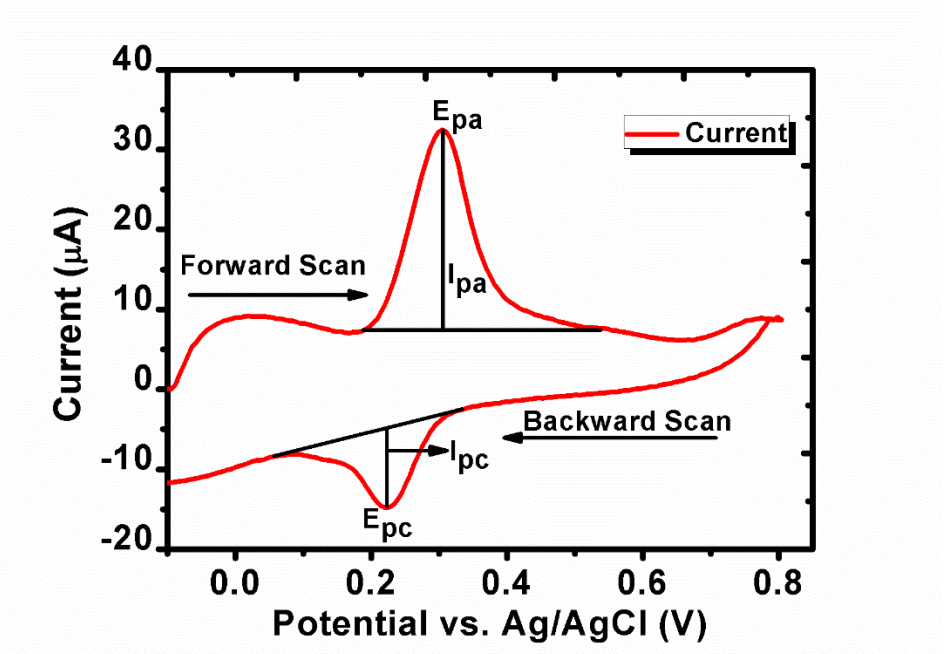

Figure 3-1: Typical cyclic voltammogram, a plot of change in current as the potential of the system is being ramped in the forward and the backward scan in a three-electrode system consisting of a working electrode, counter electrode, and a reference electrode. The parameters have their usual meanings, where Epa is anodic peak potential, Ipa anodic peak current, with Epc being the cathodic peak potential and Ipc being cathodic peak current.

3.1.2 Structural and morphological techniques

This section entails theoretical principles of structural and morphological characterisation techniques. Attenuated total reflection mode transform infrared spectroscopy, UV-Visible spectroscopy, thermogravimetric techniques are some of the structural characterizations while high-resolution transmission spectroscopy is employed for morphological characterisation of nanomaterials.

3.1.2.1 Attenuated total reflection mode Fourier transform infrared (ATR-FTIR)

Internal-reflection spectroscopy is a technique for obtaining IR spectra of samples that are difficult to deal with, such as solids of limited solubility, films, threads, pastes, adhesives, and powders. The major advantage of ATR spectroscopy is its ability on a wide variety of sample types with a minimum of preparation, for obtaining absorption spectra (Skoog *et al.* 2017).

The principle of operation of ATR spectroscopy significantly relies on reflection as it occurs when a beam of radiation passes through a dense medium to a less dense medium as shown in Figure 3.2. Before the complete reflection of the radiation beam, there is a linear relationship between the amount of reflected initial beam and the incident angle of the beam. Scientists have long established that before reflection occurs, the incident beam of radiation penetrates a certain distance into the less dense medium (sample). The distance of penetration is also dependent upon the angle of the incident beam with respect to the interface, the different wavelengths, and refraction indexes of the more and less dense medium(Atitar *et al.* 2015).

Upon the correct adjustment of the incident angle, the evanescent wave is absorbed by the less dense medium with an ATR spectrum obtained, like that of an ordinary IR spectrum.

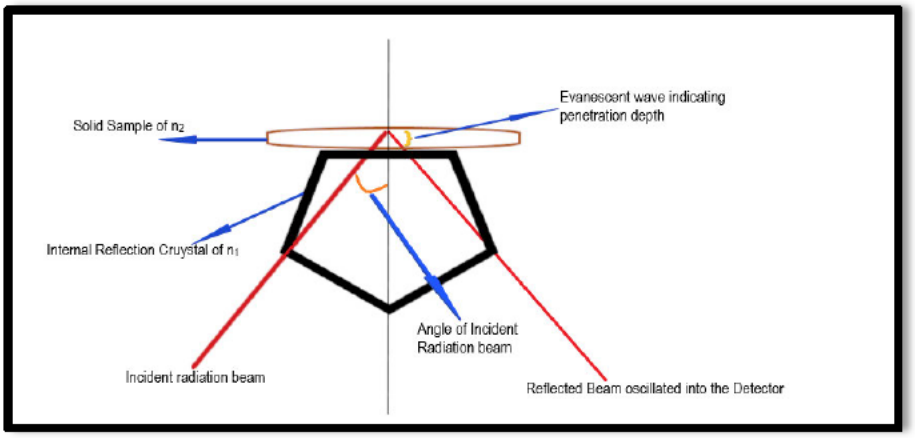

Figure 3-2: ATR schematic diagram showing a solid sample of lower refractive index mounted on an ATR internal crystal comprising of a higher refractive index. The materials used as ATR crystals include KRS-5, AgCl, Ge, and Si materials(Skoog *et al.* 2017).

3.1.2.2 High-resolution transmission electron microscopy (HR-TEM)

The transmission electron microscope is one of the most sophisticated, expensive, and widely used instrumentation in scientific research. This microscopic technique utilizes a beam of electrons that form a sample image after transmittance through the medium. The advantage of TEM lies in its ability to be employed in determining the structural and physical properties of the sample down to the atomic level. The interaction of the sample matter with the beam of electrons results in an image that can be magnified and focused on the imaging device. This study applied a high-resolutions transmission electron microscope for determining the size of the synthesized nanoparticles, the distribution, and morphology of the nanomaterials used for fabricating the platinum electrode in immunosensor development.

3.1.2.3 UV-Visible spectroscopy

Across the face of industry UV-Vis spectroscopy, based on electromagnetic radiation in the wavelength region of 190 to 800 nm, is applied in diverse fields such as chemistry, biology, forensic science, clinical chemistry, and many other fields, but what is common is its principle of operation. Spectroscopic techniques such a UV depend

on interactions of the radiation energy with matter leading to the researcher obtaining information about the sample of interest(Bakeev 2010).

Most liquid and gas phase UV-vis spectroscopic measurements rely on the well-known Lambert-Beer Law with the equation which links the concentration of the measured sample to its absorbance:

$$A\lambda = \varepsilon bc \qquad \textbf{[Eqn 3.1]}$$

where A is absorbance, ε is the molar absorption coefficient in units of L/(mol cm), b is the path length of the measurement in units of cm, and C is the concentration in units of mol/L. The index λ indicates that the Lambert-beer law is restricted to monochromatic radiation only.

Ultraviolet and visible spectroscopy is widely used for the quantitative determination of many inorganic, organic, and biological species, as well as for the qualitative characterization of these mentioned compounds based on their distinct wavelengths of maximum absorbance upon interaction with the monochromatic radiation.

3.1.3 Field flow fractionation characterization technique

Field flow fractionation (FFF) is a high-resolution separation technique for a wide range of compounds ranging from nanomaterials to polymers, distinguished into asymmetric field flow fractionation (AF4) and centrifugal field flow fractionation (CF4). The two powerful aspects of FFF can separate colloids up to 1 micron and nanoparticles ranging between 1 nm and 100 nm (Sogne *et al.* 2017).

In Chromatography, the separation is attributed to the partitioning of the separated species resulting in chemical interactions between them and the stationary phase, whereas in field flow fractionation, the separation is brought about by physical forces. In AF4, species are separated by application of a cross-flow in a ribbon-like channel, and in CF4 species achieve separation by application of a circular cross-flow as shown in Figure 3.3.

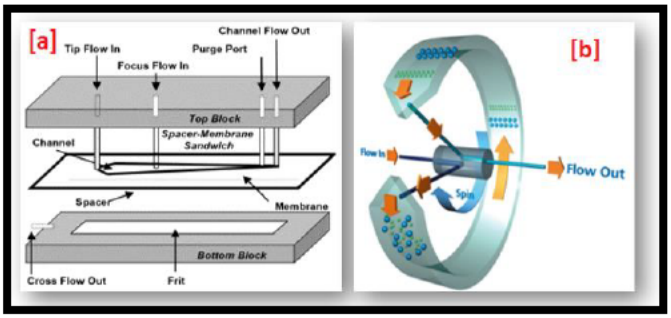

Figure 3-3: **[a]** Separation unit for asymmetric field flow fractionation comprising of two blocks sandwiching a ribbon-like channel held by spacer membrane **[b]** Separation unit for centrifugal field flow fractionation consisting of the circular channel for species separation (Poda *et al.* 2011).

The FFF multi-detector (UV and Light scattering detectors) coupling allows this technique to be a versatile tool in particle and colloidal analysis, obtaining physio-chemical properties such as the molar mass of macromolecules and particle size for nanoparticles of interest (Dubascoux *et al.* 2010). Field Flow Fractionation is employed in zinc oxide nanoparticles size characterization for this study, which is then applied in electrochemical immunosensor development for food technology application.

3.1.4 Inductively-coupled Plasma mass spectrometer

Inductively coupled plasma mass spectrometry (ICP-MS) is important instrumentation capable of measuring up to the lowest detection limits of almost every element in the periodic table. It is one of the leading methods for bulk compositional characterization although it has been proven to be more than efficient single-particle characterization. Single-particle inductively coupled plasma mass spectrometry (spICP-MS) can swiftly analyse aqueous dispersed metal nanomaterials, giving the researcher information such size, size distribution, particle concentration (Montaño *et al.* 2016). In this study, spICP-MS is used for determining the size of hydrothermally synthesized ZnONPs.

3.1.5 Thermogravimetric characterization technique

A Differential scanning calorimeter (DSC) is the instrument designed for measuring the energy that flows into or out of the sample. The heat flows into or out of the sample material are observed with the DSC technique as the temperature is ramped to observe

material transitions such as melting or recrystallization and with heat flow curves being recorded (Charsley *et al.* 2019).

Thermal analysis (TA) is defined as the analysis of sample thermodynamic property changes (mass, volume, heat, enthalpy, etc.) that are brought about by the alteration of imposed temperature (temperature-programmed or sample-controlled), in a controlled and programmed atmosphere. Thermogravimetric analysis (TGA) falls under TA and refers to the measurement of the change of sample mass as a result of subjecting it to temperature changes(Gaisford *et al.* 2016).

Instrumentation of an ordinary TGA equipment is comprised of an intensively sensitive thermobalance, a furnace covering ambient temperature up to 1000 °C, a purge gas line for providing inertness into the system or for improving reactivity of species to be analysed, and lastly for the control of the instrument, data acquisition and processing, the computer system is one vital component of TGA.

3.2 Computational chemistry

Computational chemistry or molecular modelling is comprised of numerous tools employable to exhaust chemical questions outside wet chemical lab. These tools include molecular dynamics and mechanics, semiempirical and density functional theory, and *ab* initio. Depending on the application of molecular modelling, it can be utilized to understand chemical reactivity of a system, energy of molecules and their transition states, molecular geometry, physical properties of substances and to understand the interaction of substrate of with the protein or enzyme of interest. This study's application of molecular modelling was mainly used for understanding the ligand-protein interaction through molecular docking studies, schematically shown in Figure 3.4.

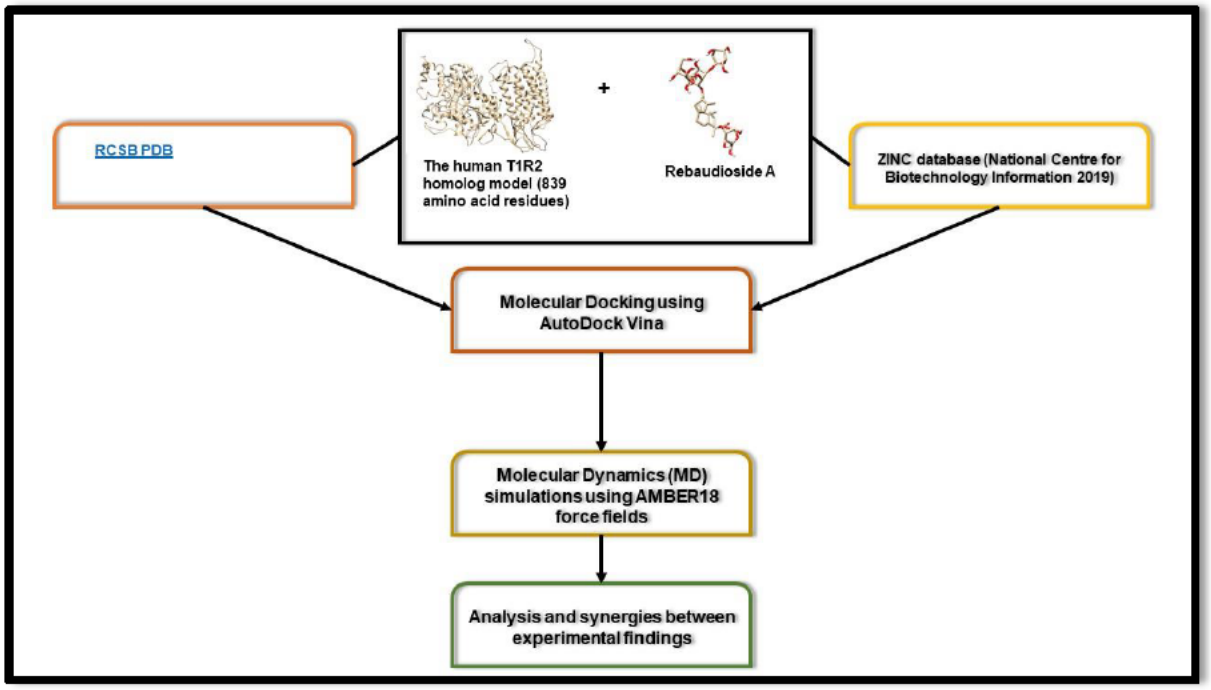

Figure 3-4 : Schematic representation of molecular modelling approaches employed in this study.

3.2.1 Density functional theory (DFT)

Density functional theory (DFT) was developed in the 1960s by Hohenberg and Kohn, deducing that a functional of the charge density with minimal energy can be employed to cast ground state properties of the systems. DFT modifies the Schrödinger equation, which is used to describe the behaviour of electrons in a system, such that approximate solutions are mimicking conditions for realistic materials(Jain *et al.* 2016). Hohenberg and Kohn had theorems which suggested using initial guess of the charge density instead of discarding all of Schrödinger's findings. DFT has led to a paradigm change in computational materials science, whereby theorists are not only able to help explain and interpret the properties of materials but also have an active role in predicting completely new materials with specific properties for different applications. DFT is a fundamental tool used by scientists for studying electron behaviour, which in turn helps to measure the performance of these materials in application fields.

3.2.2 DFT-based DMOL3 code

The accuracy of DFT calculations is largely linked to the choice of functionals used. Although up to date, no exact energy functional has not been determined, approximate models are in place and accurately predict behaviours for many materials(Jain *et al.* 2016). Kohn and Sham revised the fundamental equations of DFT in aiming to obtain the most complex electron interactions through an "exchange-correlation" functional, where they concluded by basing approximations of this functional on gas models, but up to date the exact form of this functional is not exactly known.

- **Born-Oppenheimer approximation**

This approximation separates the motion of nuclei and electrons by virtue of their difference is mass, where electrons are much smaller and therefore move much faster, hence the basis of the approximation is that the nuclei in a molecule are stationary with respect to the electrons. The Born-Oppenheimer approximation, therefore, reduces the Hamilton operator Equation (3.2) and effectively simplifying the Schrödinger equation.

$$\hat{\mathrm{H}}_{elec} = -\frac{1}{2}\sum_{i=1}^{N} 1\nabla_i^2 - \sum_{i=1}^{N} 1 \sum_{A=1}^{M} \frac{Z_A}{r_{iA}} + \sum_{i=1}^{N} 1 \sum_{j>i}^{N} \frac{1}{r_{ij}} = \check{\mathrm{T}} + V_{Ne} + V_{ee} \qquad \textbf{[Eqn 3.2]}$$

- **The Hartree-Fock Approximation**

Hartree-Fock theory was developed to solve the Schrödinger equation, it is considered an output determinant capable of lowering the average value of the Hamilton operator. It is an approximation an electron wave function by using an anti-symmetrised product, known as a Slater determinant (Φ_{SD})

$$\Psi_0 \approx \Phi_{SD} = \frac{1}{\sqrt{N}} \begin{vmatrix} x_1(\vec{x}_1) & x_2(\vec{x}_1) & \cdots & x_N(\vec{x}_1) \\ x_1(\vec{x}_2) & x_2(\vec{x}_2) & & x_N(\vec{x}_2) \\ \vdots & \vdots & & \vdots \\ x_1(\vec{x}_N) & x_2(\vec{x}_N) & \ldots & x_N(\vec{x}_N) \end{vmatrix} \quad \textbf{[Eqn 3.3]}$$

- **The Hohenberg–Kohn Theorems**

The first of these two theorems states that the electron density determines ground state properties using only 3 spatial coordinates, thus determining the Hamilton operator and enabling computation of the wave functions of all states and all material properties. The second Hohenberg–Kohn Theorem establishes a variational principle. The theorem states that the energy and density of the ground state correspond to a functional delivering the lowest energy, provided that the input density is the true ground state density. These theorems enable the calculation of molecular properties from the electron density.

- **The Kohn-Sham equation**

This approach makes use of a fictitious non-interacting reference electron system in which density is the same as that of the interacting electrons of a real system. This reference system is built from a set of one electron functions and enables the determination of a systems kinetic energy. The Kohn-Sham approach makes use of orbitals to calculate the non-interacting kinetic energy using the following equation.

$$\left[-\tfrac{1}{2} \sum_{i}^{N} 1 \nabla_i^2 + V_{ext}\ (r) + \int \frac{\rho(r`)}{|r - r`|}\, dr` + v_{xc}\ (r) \right] \phi_i(r) = \varepsilon_i \phi_i\ (r) \quad \textbf{[Eqn 3.4]}$$

DMoL3 is a computer modelling program that utilises DFT to simulate chemical reactions and predicts properties of atoms, molecules, clusters, surfaces, and other materials in all three phases of matter. Some of DMol3 capabilities include; *geometry*

optimization; transition-state search and optimization, enabling geometry stabilisation by bringing the energy of the structure to a stationary point; and *molecular dynamics*, which permit the simulation of atom motion as a function of time taking account temperature effects. DMol3 also performs numerous calculations such as; *total and single-point energy*, which is generally negative and corresponding to a bound state; *elastic constants*, providing mechanical properties of a substance by an elastic constants tensor calculated from energies corresponding to an applying finite displacement distortion; *reaction kinetics,* estimated from the transition state theory; and *electron transport,* which enables the calculation of electron transmission or currents.*(*BIOVIA *Materials Studio, 2019)*.

3.2.3 Molecular docking

In structural molecular biology and computer-assisted drug design, molecular docking is a widely employed tool. Experimentally, conventional characterization techniques like X-ray crystallography and nuclear magnetic resonance (NMR) are used to predict and determine unknown protein structures whereas drug discovery has been utilizing molecular modelling as a tool for drug discovery. Molecular docking methodology explores the behaviour of small molecules in the binding site of a target protein(Pagadala *et al.* 2017). Molecular docking aims to predict predominant binding mode(s) between 3-dimensional micro or molecular molecules. ligand-protein docking methods employ a search algorithm to predict the binding mode(s) of the ligand to the 3-dimensional protein of interest, where these docking scores orderly rank dockings with lower energy scores desirable. The search procedure evaluates the conformation of the ligand repeatedly until the convergence to the minimum energy is reached.

Finally, an affinity scoring function, ΔG [U total in kcal/mol], is employed to rank the candidate poses as the sum of the electrostatic and van der Waals energies. The driving forces for these specific interactions in biological systems aim toward complementarities between the shape and electrostatics of the binding site surfaces and the ligand or substrate. In this study, molecular docking is used to determine the

affinity of the recognition element (T1R2) to Rebaudioside A, as the antibody (T1R2) was used in electrode modification for immunosensor development.

3.2.4 Molecular dynamics simulation

The understanding of detailed structure and thermodynamics of biomolecular systems have significantly dependant on molecular dynamics (MD) simulations. MD simulations are further applicable for understanding physical behaviours of biological macromolecules, writing off the initial rigid viewing of proteins, and taking into consideration the internal motions and changes in conformation to later interpret the behaviour of these systems(Karplus and McCammon 2002).

3.2.4.1 Force fields

In biomolecular simulations, for the past few decades, molecular force fields have instrumental benefiting materials scientists. There have been recent developments in method parameterization and representation of nonbonded interactions of all-atom, nucleic acid, and small molecule forcefields(Nerenberg and Head-Gordon 2018).

Numerous proteins and relatively short peptides have been successfully simulated using force fields such as AMBER ff94, CHARM22, and OPLS-AA. Small single domain proteins with approximately 100 amino acids are feasible to be simulated in these force fields, whereas experimental findings have indicated difficulties in simulating intrinsically disordered molecules. In molecular modelling(MM), a force field is defined and applied in atomic systems or coarse-grained particles for determining potential energy of that systems by applying derivatisation forms from mathematical models and parameter settings.

(i) COMPASS

Condensed-phase optimized molecular potentials for atomistic simulation studies (COMPASS) force field's basis of formulation was to be applied in material science, whereas other well-known force fields such as AMBER, CHARMM, and MM3 were also designed to study biological molecules of concern in the recent applications (Bunte and Sun 2000). The COMPASS force field has been proven to be relatively

faster than other *ab* initio methods and finds its application in predicting properties of molecules such as molecular vibrations, structures, and conformations. The only noted limitation for this force field is that it is not suitable to study reactions, hence, the need to develop a reactive force field when studying reactions.

The validation of COMPASS force field parametrization is achieved by performing molecular mechanics and dynamics calculations (Sun *et al.* 1998).

(ii) Universal force field

Universal force field (UFF) is widely applied in unstrained and uncongested organic molecules for predicting their structures, calculating bond lengths and angles. Other force field types, such as MM2 and MM3 were used for validation and comparison without varying molecules of interest (Casewit *et al.* 1992). Universal Force Field employs general force field rules when deriving basic parameters depending on the element under study, it's hybridization and connectivity (Rappe *et al.* 1993).

(iii) Dreiding

DREIDING is a simple generic force field that is useful for predicting structures and dynamics of organic, biological, and main-group inorganic molecules.

We report the parameters for a new generic force field, DREIDING, that we find useful for predicting structures and dynamics of organic, biological, and main-group inorganic molecules. The philosophy in DREIDING is to use general force constants and geometry parameters based on simple hybridization considerations instead of the individual force constants and geometric parameters that depend on the combination of atoms involved in the bond, angle, or torsion terms. Thus, all bond distances are derived from atomic radii, and there is only one force constant each for bonds, angles, and inversions and only six different values for torsional barriers. Parameters are defined for all possible combinations of atoms, and new atoms can be added to the force field rather simply. This paper reports the parameters for the "non-metallic" main-group elements (B, C, N, O, F columns for the C, Si, Ge, and Sn rows) plus H and a few metals (Na, Ca, Zn, Fe). The accuracy of the DREIDING force field is tested by comparing with (i) 76 accurately determined crystal structures of organic compounds

involving H, C, N, O, F, P, S, Cl, and Br, (ii) rotational barriers of a number of molecules, and (iii) relative conformational energies and barriers of a number of molecules. (Mayo *et al.* 1990).

(iv) General amber force field (GAFF)

General Amber force field (GAFF) for organic molecules. GAFF is designed to be compatible with existing Amber force fields for proteins and nucleic acids and has parameters for most organic and pharmaceutical molecules that are composed of H, C, N, O, S, P, and halogens. It uses a simple, functional form and a limited number of atom types but incorporates both empirical and heuristic models to estimate force constants and partial atomic charges. (Wang *et al.* 2004a).

CHAPTER 4: MATERIALS AND METHODS

This chapter focuses on the experimental and computational methods employed in this study, including the hydrothermal synthesis procedure for ZnONPs employed in the fabrication of the developed immunosensor. The stages of the study from the bare platinum electrode to the final T1R2 immunosensor, are discussed with their sensitivities and optimized parameters being stated. This is followed by a series of computational methods employed in this work.

4.1 Experimental methods

4.1.1 Instrumentation

Under this section, methodologies and experimental parameters are stated, starting from characterization techniques for nanomaterials used for modifying platinum working electrode to electrochemical instrumentation of obtaining redox properties of Reb A.

4.1.1.1 Electrochemical techniques

Electrochemical experiments were measured at room temperature using the 797 VA Computrace system supplied by Metrohm, Durban, South Africa. This system utilizes three electrodes, reference, working, and counter/auxiliary electrode as shown in Figure 4.1. For this study, the rotating disc platinum electrode modified with ZnONPs/GO/MWCNTs/T1R2 was used as the working electrode, with a graphite electrode as the counter and Silver/Silver Chloride (Ag/AgCl reference electrode) as the reference electrode.

797 VA Computrace permits the user to perform qualitative and quantitative measurements. All qualitative measurements were done using cyclic voltammetry (CV)

to study the electrochemical behaviour of the developed immunosensor thoroughly. The quantitative methods use Differential Pulse Voltammetry (DPV) as one of the tools for measuring analyte concentration in real samples. This included calibration curve formation where at optimized electrochemical conditions standards were measured.

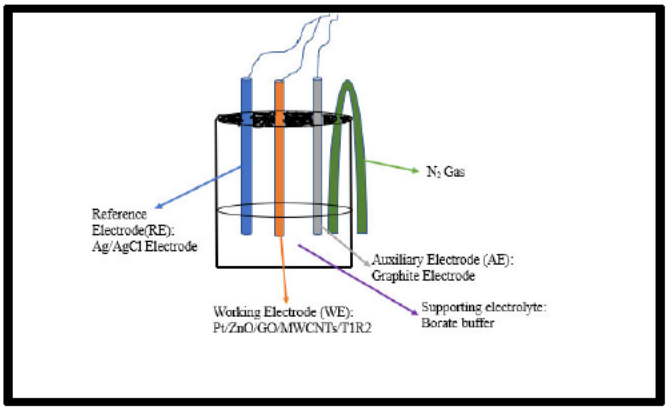

Figure 4-1: Schematic representation of a three-electrode electrochemical cell system, composed of the reference electrode, auxiliary electrode, working electrode, supporting electrolyte, and inert gas for purging.

4.1.2 Reagents and materials

Disodium tetraborate ($Na_2B_4O_7 \cdot 10H_2O$, 99.5% assay) supplied by Merck, Rebaudioside A ($C_{44}F_{70}O_{23}$, assay ≥95% HPLC, MW: 967.01 g/mol) supplied by SIGMA-ALDRICH, Germany, Hydrochloric acid (HCl, Specific gravity of 32%), Anti-TAS1R2 (Extracellular Domain, Antibody produced in Rabbit, supplied by SIGMA-ALDRICH, Saint Louis, United States of America), Graphene Oxide 2 mg/mL dispersion in H_2O supplied by SIGMA-ALDRICH, Saint Louis, United States of America, Multi-Walled Carbon Nanotubes, Zinc gluconate hydrate ($C_{12}H_{22}Zn \cdot xH_2O$, AR, 97% purity) was supplied by Alfa Aesar chemical reagent company, potassium hydroxide (KOH, ≥85% Assay) was supplied by Saarchem Merck Chemicals, Gauteng, South Africa, Methanol (CH_3OH, ≥99.9% purity for HPLC) was supplied by SIGMA-ALDRICH chemical company, 0.2% Novachem supplied by Postnova analytics (Germany). The Pt working electrode was supplied by Metrohm Ion Analysis. All the reagents were of analytical grade and were used without any further purification with deionized water used for the preparation of samples, not unless stated otherwise.

4.1.2.1 Preparation of working solutions

(i) Preparation of borate buffer

Borate buffer with a concentration of 0.1M and a pH of 9.25 was prepared in a 100 mL volumetric flask by quantitatively transferring 3.8137 g of disodium tetraborate salt, after dissolving, deionized water was used to calibrate to the mark. 0.3994 g of sodium hydroxide was quantitatively weighted into 100 mL volumetric flask to prepare 0.1 mol/L, and hydrochloric acid volume was calculated from 1.1493 g/mL density to prepare 0.1 mL in 100 ml volumetric flask. These solutions were used to adjust and obtain the required pH, in a pH meter (pH 211 Microprocessor pH meter from HANNA Instruments) calibrated using pH 4 and 7 buffers. The prepared borate buffer solution was stored in the refrigerator at 4 ^{o}C after use. Below are calculations for the supporting electrolyte preparation:

(ii) Preparation of 1000 mg/L Reb A stock solution

A 1000 mg/L of Reb A stock solution was prepared in deionized water, using standard dilution procedure, 100 mg/L Reb A working standards solutions were prepared. Redox properties of Reb A were studied with the working standards on the working electrode from the bare platinum rotating disc electrode to the modified sensor. After use, the stock solution and working standards were kept refrigerated.

(iii) Preparation of T1R2 antibody solution

The T1R2 antibody was always kept refrigerated at -4 ^{o}C when not use. Before use, the antibody was allowed to liquify on room temperature,20 µL of T1R2 antibody was quantitatively drop-casted unto the platinum electrode modified with ZnONPs, GO, and MWCNTs. The fabricated electrode was allowed to stand for 60 min at room temperature before electrochemical measurements of Reb A were taken.

4.1.3 Synthesis of nanostructures

In recent years nanotechnology has had major developments with researchers putting more effort into developing new applications for nanomaterials in this field. This has led to the reporting of numerous green and hazardous free chemical methods for synthesizing NPs with the desired size and shape. This study based its ZnONPs synthesis on the modified hydrothermal method (Ahmad *et al.* 2011; Laber *et al.* 2016).

4.1.3.1 Synthesis of ZnONPs by the hydrothermal method

In the following synthesis, the three factors that influence the morphology of the synthesized flower-like nanostructures of ZnO are the temperature of the pressure cooker, the concentration of the alkali and the delay time the nanostructures spend on the pressure cooker (Laber *et al.* 2016). The synthesis was divided into two batches as follows, with a summary of parameters presented in Table 4.1 below:

Batch 1: Pressure varying on the Pressure Cooker

Procedure: 1.1392 g of zinc gluconate and 0.1403 g in a molar ratio of 1:1 were dissolved in 50 mL distilled water with vigorously magnetic starring at 850 rpm for 30 min. The solution remained white in colour and was stirred at room temperature. After that, the resulting suspension was hydrothermally treated in a Russel Hobbs 6L electric pressure cooker presented in Figure 4.2, under manual setting with a delay timer of 6 h at low pressure (temperature = 104 °C and exact pressure= 17 kPa).

The resulting white precipitate was collected by centrifugation at 2500 rpm for 30 min using HeHich universal centrifuge (L1G3). The white precipitates were oven-dried at 60 °C for 10 h. Finally, for calcination, Scientific oven (MODEL: Series 2000) was used at 250 °C for 3 h. The ZnO products were ready for characterization, and the above procedure was repeated with 30 and 70 kPa in the electric pressure cooker.

Table 4-1: The following table sums up parameters in the hydrothermal synthesis of ZnONPs.

The pressure was then investigated variable		
Batch 1,1	0.05 mol/L Zinc gluconate and 0.05 mol/L potassium hydroxide	Low pressure: temp = 104 °C pressure approx. 17 kPa
Batch 1,2	0.05 mol/L Zinc gluconate and 0.05 mol/L potassium hydroxide	Medium pressure: temp = 107 °C pressure approx. 30 kPa
Batch 1,3	0.05 mol/L Zinc gluconate and 0.05 mol/L potassium hydroxide	High pressure: temp = 115 °C pressure approx. 70 kPa

Batch 2: Varying concentrations of KOH

The concentration of potassium hydroxide was investigated as a variable affecting the morphology of ZnO flower-like nanoparticles.

In different beakers, 0.2805 g, 0.4208 g, and 0.5611 g were mixed with 1.1312 g of zinc gluconate, and the salts were dissolved in 20 mL of distilled water with vigorously magnetic starring at 850 rpm for 30 min. The solutions remained white in colour and were stirred at room temperature. After that, the resulting suspensions were hydrothermally treated in a Russel Hobbs 6L electric pressure cooker (MODEL NO. RHEP7), under manual setting with a delay timer of 6 h at low pressure (temperature = 104 °C and exact pressure= 17 kPa).

The resulting white precipitate was collected by centrifugation at 2500 rpm for 30 min using HeHich universal centrifuge (L1G3). The white precipitates were oven-dried at 60 °C for 10 h. Finally, for calcination, Scientific oven (MODEL: Series 2000) was used at 250 °C for 3 h. The ZnO products were ready for characterization.

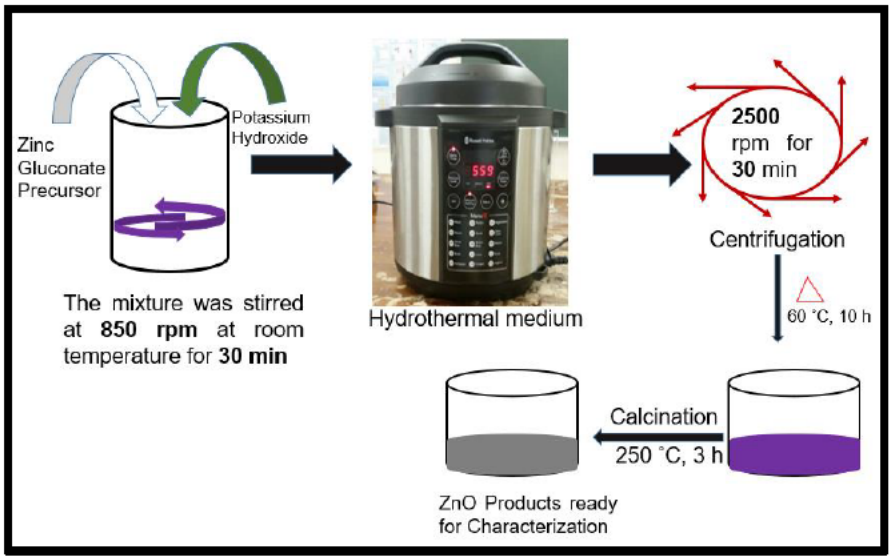

Figure 4-2: Schematic representation for Hydrothermal synthesis of zinc oxide nanoparticles employing an electric pressure cooker from a zinc gluconate precursor is shown.

4.1.4 Structural characterization techniques

This section entails theoretical principles of structural and morphological characterisation techniques. Attenuated total reflection mode transform infrared spectroscopy, UV-Visible spectroscopy, thermogravimetric techniques are some of the structural characterizations while high-resolution transmission spectroscopy is employed for morphological characterisation of nanomaterials.

4.1.4.1 Attenuated total reflection mode Fourier transform infrared (ATR-FTIR)

For functional group characterisation, Attenuated Total reflection infrared spectroscopy was used as the molecule absorbed IR energy because of change in its dipole moment due to vibrations or rotations. The ATR characterization of ZnONPs was performed in the range of 4000 to 500 cm^{-1}.

4.1.4.2 High-resolution transmission electron microscopy (HR-TEM)

The morphological characterization of the nanocomposite used for electrode modification was done with high-resolution transmission microscopy. A JEOL 2100 High-resolution Transmission Electron Microscope (brightfield, darkfield, diffraction STEM, EDX) was used for optical microscopic viewing of the Biocomposites employed in electrode fabrication, at 200 k V acceleration voltage. The samples were dissolved in ethanol and sonicated for an hour before being placed on a carbon film, for microscope viewing after drying at room temperature.

4.1.4.3 UV-Visible spectroscopy

Single beam UV-Visible spectroscopy (Cary 50, version 1.00) was employed for obtaining optical properties of the synthesized zinc oxide nanoparticles, over a broad wavelength range of 200 nm to 800 nm. In this instrument, the blank and sample solution were separately placed in vial or cuvette, which is then inserted into the radiation path within the instrument.

4.1.4.4 Field flow fractionation characterization technique

Field flow fractionation (FFF) is a technique with different modes that are capable of characterising and separating large particles, polymers, colloids that are usually suspended or dissolved. This study applied two modes of field flow fractionation, asymmetric and centrifugal field flow fractionation, for particle size characterization of zinc oxide nanoparticles suspended in 0.2 % NovaChem.

i. AF4

AF4 mode of field flow fractionation with the injection volume of 19,7 µL, for particle size analysis of ZnONPs had the following dimensions: The AF4 system is furnished with the solvent degasser (PN7520) compatible with aqueous solutions, 2 Piston HPLC pump (PN1130) with aqueous compatibility, an autosampler (Perkin Elmer PN 5300 Autosampler), Perkin Elmer online Multi-Angle Light Scattering MALS detector (PN 3621/21 Angle Detector) and Perkin Elmer 4-channel UV/vis detector (PN3241 DAD). The radii of gyration of the different ZnONPs were determined by employing MALS

detector with different (21 to be specific), angles with 90º angle being used as optimum for radii of gyration determinations. The applied angle showed the best fit with the sphere model. The detectors, MALS detector, were set to 20% LP, whereas that of the UV-vis detector was set to be CH1: 280 nm, CH2: 220 nm, CH3: 254 nm, and CH4: 320 nm. The system is equipped with a 10 kDa regenerated cellulose membrane, Aqu/Org, 10-70°C, and following size dimensions: 294 mm ×30 mm, 10 PC.s

Ultrapure water was used to prepare 0.2 % Novachem eluent, which was used throughout the experiment.

ii. CF4

CF200 mode of field flow fractionation with the injection volume of 19,7 µL, for particle size analysis of ZnONPs had the following dimensions: The CF4 system is furnished with the solvent degasser (PN7520) compatible with aqueous solutions, 2 Piston HPLC pump (PN1130) with aqueous compatibility, an autosampler (Perkin Elmer PN 5300 Autosampler), Perkin Elmer online Multi-Angle Light Scattering MALS detector (PN 3621/21 Angle Detector) and Perkin Elmer 4-channel UV/vis detector (PN3241 DAD). The radii of gyration of the different ZnONPs were determined by employing MALS detector with different (21 to be specific), angles with 90º angle being used as optimum for radii of gyration determinations. The applied angle showed the best fit with the sphere model. The detectors, MALS detector, was set to 20% LP, whereas that of the UV-vis detector was set to be CH1: 280 nm, CH2: 220 nm, CH3: 254 nm, and CH4: 320 nm.

Ultrapure water was used to prepare 0.2 % Novachem eluent, which was used throughout the experiment. A summary of working parameters is shown in Table 4.2 below.

Table 4-2: Summary of Field Flow Fractionation working parameters for the separation of ZnONPs.

AF4		CF4	
Detector flow (mL/min)	0.50	Flow rate (mL/min)	0.50
Injection flow (mL/min)	0.20	Injection Volume (µL)	20
Injection time (min)	5	Injection time (min)	1.2694
Spacer (µm)	350	Spacer (µm)	250
Run Time (min)	55.3	Rotor speed (rpm)	1500
Crossflow (mL/min)	1	Run Time (min)	64.37
Focus pump (mL/min)	0.1	Focusing time (min)	
Tip pump (mL/min)	0.10		
Injection volume (µL)	21.5		

4.1.4.5 Inductively coupled plasma mass spectrometer

A PerkinElmer NexION Inductively coupled plasma mass spectrometry furnished with Syngistix Nano Module was used for the single-particle analysis of the hydrothermally synthesized ZnONPs.

4.1.4.6 Thermogravimetric characterization technique

The thermogravimetric analysis (TGA) technique was used for studying the thermal stability of the nanomaterial used for platinum electrode modification. The weight changes of the samples were measured as the temperature profile was ramped from 0 ºC to 1000 ºC. The calibration of the TGA was obtained using Indium standards. This TGA model was comprised of an MX1/XP1 balance type consisting of a 70 µL aluminium sample holder. Nitrogen purge gas was used for the inertness of the system. TGA's compatibility various sample types were utilized in obtaining the thermal stability of nanomaterial used in this study for electrode modification.

4.1.5 Fabrication of sensors

4.1.5.1 Preparation and fabrication of GO/ZnONPs/T1R2/Pt-E for detection of Reb A

Zinc oxide nanoparticles synthesized from zinc gluconate precursor hydrothermally were homogenised with graphene oxide, multiwalled carbon nano cubes, and T1R2 as a recognition element for electrochemical immunosensing Reb A. Zinc oxide powder nanoparticles were dispersed in water to prepare 1 mg/ml solution. This resulting ZnONPs dispersion was then ultrasonicated for an hour to improve monodispersity while lowering agglomeration effects. Graphene Oxide solution was prepared according to (Bathinapatla *et al.* 2016), by quantitatively measuring 1 ml of graphene oxide into 10 ml of deionized water. The ZnONPs/GO nanocomposite was achieved by mixing ZnONPs water dispersion and GO water dispersion in a ratio of 1:1 and sonicating for one hour to obtain a homogenized mixture. ZnONPs/GO/MWCNTs nanocomposite was obtained by mixing bare MWCNTs dispersed in DMF with the previously prepared ZnONPs/GO nanocomposite.

The resulting ZnONPs/GO/MWCNTs were also homogenized by ultrasonication for 1 hour to obtain a black paste for platinum working electrode modification. T1R2 which serves as a biological recognition element for Reb A was drop-casted on the last stage of electrode modification, with the modified electrode left to stand at room temperature for an hour before analysis.

Before the modification of the nanomaterial unto the surface of the platinum electrode, cleaning to ensure removal of the chemisorbed and physiosorbed materials. This cleaning stage was obtained by gently polishing the surface of the electrode against alumina (≤ 3 μm) followed by rinsing off with deionized water. The manual cleaning was then followed by electrochemical by measuring current responses in acidified water while the potential was ramped from -1 V to 1 V Vs Ag/AgCl. During the step by step modification, shown in Figure 4.3, a 5 μL of the nanocomposite was carefully drop-casted onto the surface of the platinum working electrode and oven-dried at 40 ^{0}C for 20 min.

The step by step fabrication of the electrochemical immunosensor for studying Reb A is shown in Figure 4.3.

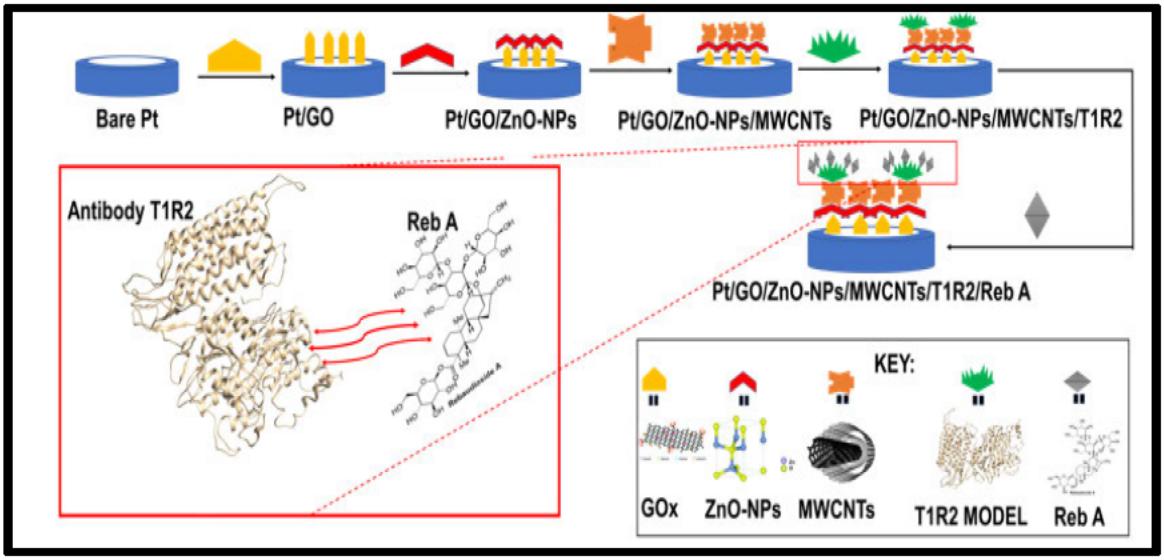

Figure 4-3: Schematic mechanism of electrode fabrication for immunosensing of Reb A

4.1.6 Electrochemical characterization

4.1.6.1 Cyclic voltammetry (CV)

Cyclic voltammetry provided qualitative electrochemical behaviour of Rebaudioside A in 0.1 mol/L pH 11.0 borate buffer (supporting electrolyte) from a potential range of -0.4 V to 0.8 V vs Ag/AgCl. The development of this Reb A sensor's parameters was optimized from bare Pt electrode to ZnONPs/GO/MWCNTs/T1R2/Pt electrode, using cyclic voltammetry.

4.1.6.2 Electrochemical measurement of Reb A

Electrochemical measurements of Reb A employed cyclic voltammetry for qualitative studies and differential pulse for quantitative studies at room temperature in a three-electrode system electrochemical cell. The three-electrode system consisted of Platinum as the working electrode, graphite electrode as the counter electrode, and silver/silver chloride as the reference electrode. For measurements, the 20 ml

electrochemical cell was filled with 10 ml of 0.1 M pH 11.0 borate buffer, 20 µL of 100 mg/L of Rebaudioside A working standard.

4.2 Computational studies

4.2.1 Template selection

Due to the absence of a crystal structure of the human taste receptor 1 (T1R2), the sequence obtained from (Uniprot ID: Q8TE23) was modelled by homology modelling using the Chimera software as an interface to the Modeller Software version 9.1.

4.2.2 Molecular docking of the human T1R2-Reb A complex

The human T1R2 homolog was docked onto Reb A, retrieved from the PubChem database using Autodock Vina. This software performs the prediction of the bound conformation based on free energy, which was calculated on the basis of the empirical force field and the Lamarckian Genetic Algorithm. The Grid module was used to create a grid box of dimensions X= 56, Y= 70 and Z= 56 along the centre X= 14.542, Y= -16.714 and Z= 63.662 with a spacing of 0.375Å. The efficiency of the predictions was amplified by setting the parameters associated with the Lamarckian genetic algorithm to the maximum efficiency values. The docked T1R2-Reb A conformation with the highest docking score was selected for the molecular dynamics (MD) simulations. The resulting human T1R2-Reb A complex was used for all subsequent methods performed in this study.

4.2.3 Molecular dynamics (MD) simulations

The molecular dynamics simulations were performed on the docked complex using the AMBER 18 molecular dynamics package (Wang *et al.* 2004a). The bonded and non-bonded description of the interactions between the various atoms has been described using the AMBER18 force fields which include the GAFF force field parameters. Due to the lack of parameters needed for Reb A in the Cornell *et al* force field, the missing parameters were created. Optimization of the Reb A was performed at the HF/6-31G*

level with the Gaussian 09 package. The human T1R2 homolog was energy minimized and equilibrated via molecular dynamics simulations and discussed as follows. The standard AMBER force field for bioorganic systems (ff03) was used to define the topology and parameter files for the T1R2 homolog and Reb A using “GAFF” force field parameters based on the atom types of the force field model developed by Cornell *et al*. The topology and coordinate files were generated using the antechamber module of AMBER 18, and the missing hydrogen atoms were added and saved for the T1R2 homolog using the LEaP module inside AMBER 18. Thereafter, the docked T1R2-Reb A complex was solvated in the octahedron box of TIP3P water model with buffering distance of 10 Å between the protein surface and the box boundary as well as the neutralization was performed by adding Na^+ counterions to mimic the biological pH. Cubic periodic boundary conditions were imposed, and the long-range electrostatic interactions were treated with the particle-mesh Ewald method implemented in AMBER 18 with a non-bonding cut-off distance of 10 Å.

Initially, a series of energy minimization steps are performed to eliminate any bad contacts in the initially built structures while restraining the solute with 500 kcal/mol/$Å^2$ harmonic force constant. The above system was minimized for 1000 cycles of steepest descent followed by 2000 cycles of the conjugate gradient. The entire system was freely minimized for 1000 iterations. Heating was performed for 50 ps from 0 to 300 K with harmonic restraints of 5 kcal/mol $Å^2$ using a Langevin thermostat with a coupling coefficient of 1/ps. The entire system was then equilibrated at 300 K with a 2-fs time step in the NPT ensemble for 500 ps and Berendsen temperature coupling was used to maintain a constant pressure at 1 bar. The SHAKE algorithm was employed on all atoms so as to constrain the bonds of all hydrogen atoms.

With no restraints imposed, a production run was performed for 100 ns in an isothermal isobaric (NPT) ensemble using a Berendsen barostat with a target pressure of 1 bar and a pressure-coupling constant of 2 ps for analysis of the energy stabilization and RMSD values of the complex. The coordinate file was saved every 1ps and the trajectory was analysed every 1ps using the Ptraj module implemented in AMBER 18.

The thermodynamic property of the system was calculated. The free binding energy of Reb A to the human T1R2 homolog active site was analysed by the Molecular Mechanics/Generalized Born Surface Area (MM/GBSA) method. A single trajectory approach was used with 100000 snapshots at 100 ps interval of each simulation. From each snapshot, free binding energy (ΔG_{bind}) was computed from the following equation:

$$\Delta G_{bind} = G_{hT1R2\text{-}Reb\ A} - G_{hT1R2} - G_{Reb\ A} \qquad \textbf{(Eqn 4.1)}$$

Where ΔG_{bind} is the free binding energy; $G_{hT1R2\text{-}Reb\ A}$ is the energy of the human T1R2-Reb A complex; G_{hT1R2} is the energy of the human T1R2, and $G_{Reb\ A}$ is the energy of the Reb A. Due to the high computational cost in the entropy calculation, 100 snapshots were extracted from the last equilibrated 100 ns trajectory of the simulation with 100 ps time intervals.

To theoretically evaluate the reliability of the calculated ΔG values, the standard error (SE) of the calculated free binding energy was estimated by using equation 2, which is related to the number (N) of snapshots chosen for the calculations (Morris *et al.* 1998).

$$SE = RMSF / N \qquad \textbf{(Eqn 4.2)}$$

Initially, a series of energy minimization steps are performed to eliminate any bad contacts in the initially built structures. The above system was minimized for 1000 cycles of steepest descent, followed by 2000 cycles of the conjugate gradient. Initial energy minimization, with a restraint potential of 500 kcal/mol $Å^2$ applied to the solute, was carried out with the aid of the SANDER module of the AMBER 18 program using the steepest descent method in AMBER 18 for 1000 steps followed by conjugate gradient protocol for 2000 steps.

After the energy minimization, the system was slowly heated up to 300 K in 40 ps MD using 1 fs integration time step, while restraining the solute with 500 kcal/mol/$Å^2$ harmonic force constant.

Initially, the neutralized system was energetically minimized using the steepest descent, and the conjugate gradient algorithms with a convergence criterion of 0.005 kcal/mol and the restraints were applied to the structure of the ligands before the equilibration phase.

The entire system was freely minimized for 1000 iterations. Heating was performed for 50 ps from 0 to 300 K with harmonic restraints of 5 kcal/mol $Å^2$ using a Langevin thermostat with a coupling coefficient of 1/ps. The entire system was then equilibrated at 300 K with a 2 fs time step in the NPT ensemble for 500 ps, and Berendsen temperature coupling (Berendsen *et al.* 1984) was used to maintain a constant pressure at 1 bar. The SHAKE algorithm (Ryckaert *et al.* 1977) was employed on all atoms to constrain the bonds of all hydrogen atoms.

The obtained docked complexes were subjected to MD simulations using the PMEMD module in AMBER 18 modelling package The GAFF force field parameters for the T1R2-Reb A complex was calculated using the antechamber module of AMBER 18. Hydrogen atoms of the proteins were added using the Leap module in AMBER 18 (Case *et al.* 2005). The docked T1R2 Reb A complex was solvated in an octahedron box of TIP3P water with a buffering distance of 10 Å between the protein surface and the box boundary (Jorgensen *et al.* 1983). Neutralization was performed by adding (Na^+) counter-ions to mimic the biological environment more closely.

Cubic periodic boundary conditions were imposed, and the long-range electrostatic interactions were treated with the particle-mesh Ewald method implemented in AMBER 18 with a non-bonding cut-off distance of 10 Å.

The partial atomic charges for Reb A was obtained using “antechamber” (Jakalian *et al.* 2000) module of AMBER 18.

Initial energy minimization, with a restraint potential of 500 kcal/mol $Å^2$ applied to the solute, was carried out with the aid of the SANDER module of the AMBER 18 program using the steepest descent method in AMBER 18 for 1000 steps followed by conjugate gradient protocol for 2000 steps.

Due to the lack of parameters needed for the ligand in the Cornell *et al.* force field (Cornell 1995), the missing parameters were created. Optimization of the ligands is first performed at the HF/6-31G* level with the Gaussian 03 package(Frisch MJ *et al.* 2004). The standard AMBER force field for bioorganic systems (ff03) (Duan *et al.* 2003) was used to define the topology and parameter files for the protein and Reb A using "gaff" (Wang *et al.* 2004b) based on the atom types of the force field model developed by Cornell *et al.* (Cornell *et al.* 1996).

4.2.3 Nanomaterials modelling

All nanoclusters were built using Materials Studio (MS) BIOVIA (Ulicny and Kozar 2018). Geometry optimization of the nanomaterials were performed with the Forcite module(Sun 1998) as implemented in the MS software. Forcite in the MS software is a classical molecular mechanics tool, designed to perform a range of tasks including fast energy calculations and geometry optimizations for single molecules as well as periodic systems. Detailed knowledge of surface interactions plays a key role in the design of many materials and processes. An important first step in such a study is the preparation of a model of molecules adsorbed onto the surface with optimized geometry (that is, energy minimized). Among the different steps involved in the modelling approach is the construction of the surface from the pure crystal, the addition of the molecules near to the surface, the definition of the potentials (by the forcefield) to study the nanomaterial interaction, followed by the geometry optimization calculation.

4.2.3.1 Adsorption Studies

Here, the Adsorption Locator (AL) module as implemented in the MS software can be used as a preparatory and screening tool with the forcefield method to obtain a ranking of the energies for each generated configuration, thereby indicating the preferred adsorption sites. Since the adsorbate can be adsorbed at different locations of choice on the GO surface, the AL module was used to deduce the best adsorption site on the surface. The AL applies Monte Carlo simulations within a lattice dynamics approach to

obtain the best configuration. Modelling and visualization were carried out with VMD (Humphrey *et al.* 1996) and Gauss View, and MS.

A 3-D model of the GO surface comprising of a pristine graphite structure, conforming to the standard structural database in the MS software was built with oxygen atoms manually added. A 3-D model of ZnONPs was built to conform to the standard structural database in MS. A supercell structure (6x6x1) of ZnO was built and the symmetry was set to have a non-periodic boundary. The unit cell of the bulk ZnO (110) was geometry optimized using the Forcite module, with an 8 x 8 x 8 Monkhorst-Pack mesh k-points and a kinetic energy cut-off of 4.5Å. The unit cell was then relaxed using the conjugate gradient method until the total forces acting on each atom were 8.401e-04 kcal/mol/A. The ZnO (110) surface was geometry optimized by solving the Kohn-Sham equation self-consistently under spin-unrestricted conditions. The double-layered MWCNT (n=10, m=10) was built using the Build option in the MS software. To observe the feasibility of all structures, their primitive structures were optimized by Forcite module with fine-COMPASS force field. The convergence criteria for the maximum values of energy alteration, force, stress, and displacement were set at 2 x 10^{-5} kcal/mol, 0.001 kcal/mol/Å, 0.001 GPa, and 10^{-5} Å respectively. Frequency calculations were carried out to determine if the compounds are at the lowest surface energy and to deduce physical interaction energies i.e. adsorption.

The adsorption energies were calculated using the following equation:

$$E_{ads} = E_{adsorbate} + E_{surface} - E_{adsorbate/surface} \quad \textbf{(Eqn 4.3)}$$

Where $E_{adsorbate}$ is the energy of the adsorbate energy without the surface, $E_{surface}$ is the surface energy of the ZnO nanoparticles and $E_{adsorbate/surface}$ is the total energy of the surface and the adsorbate. In this case, if $E_{ads} < 0$; the adsorption energy implies stability and the chemical process is exothermic, with a more negative value implying stronger adsorption energy.

CHAPTER 5: RESULTS AND DISCUSSION

Experimental and computational results are presented in this chapter. The experimental results discuussed are, but not limitted to, characterization results of the hydrothermally synthesized ZnONPs and nanomaterial employed in electrode surface modification. Electrochemical behaviour of Reb A is entailed in this chapter using the developed immunosensing electrode. On the other hand, molecular modelling were employed for an in-depth understanding of molecular properties of the nanomaterial employed for electrode modification and the recognition element. The synergies between experimental and computational results are detailed in this chapter.

5.1 Experimental

Under this section, results are discussed, starting from the characterization techniques for studying the compositions and properties of nanomaterials used for modifying the platinum working electrode to the electrochemical redox properties of Reb A.

5.1.1 Characterization of bare ZnONPs

Prior application of any desired nanomaterial in any field of nanotechnology, it is very crucial to study properties of these materials, such as size, stability, surface composition, shape, and purity, as these traits significantly contribute to their performances. Below is the discussion of the techniques employed in this study for nanomaterial characterization.

5.1.1.1 Structural, morphological and optical evaluation

(i) Attenuated total reflection mode Fourier transform infrared (ATR-FTIR) analysis

The ATR-FTIR spectrum of precursor salt of zinc gluconate used for ZnONPs hydrothermal synthesis, and that of the newly synthesized ZnONPs is presented in Figure 5.1. All the FTIR analysis was carried out on an Agilent Cary 630 FTIR employing microLab software from the spectrum range of 4000 cm^{-1} to 650 cm^{-1}. The ZnO absorption spectra at 1392 cm^{-1} in figure 5.1 were also observed by Reddy and colleagues (Gnanasangeetha and SaralaThambavani 2013). The absorption peak at 3247 cm^{-1} is characteristic of the -OH stretching vibration, whereas the -C=O stretching vibration is characterized by the peak at 2949 cm^{-1}, and at 1574 cm^{-1} the -C-H stretching vibration is evident (Becheri *et al.* 2008).

[a] [b]

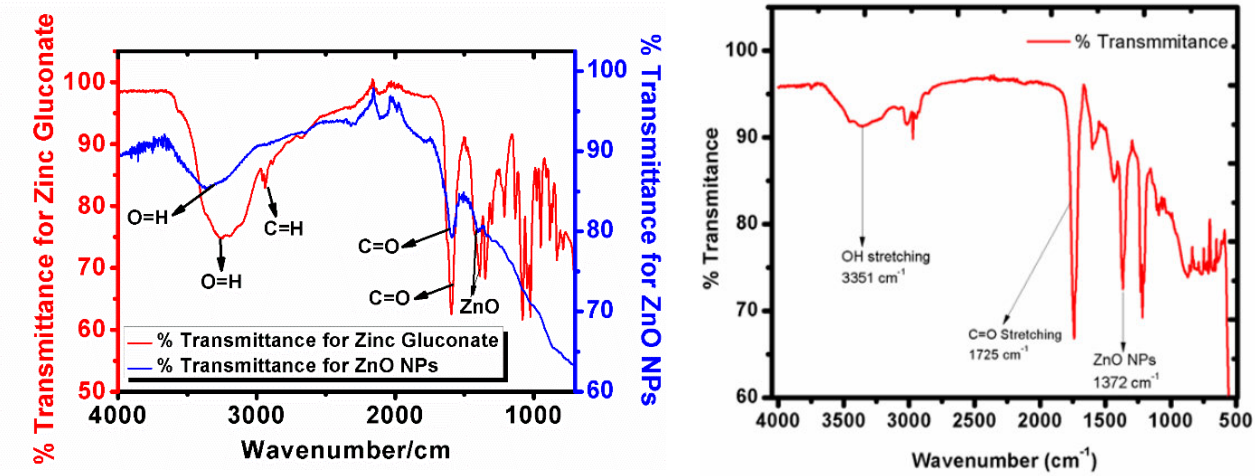

Figure 5-1: [a] Infra-red spectrum overlay of Zinc Gluconate in red and ZnONPs in blue. **[b]** Attenuated total reflectance Infra-red spectrum of ZnONPs with its characteristic absorption peak at 1372cm^{-1}

(ii) High-resolution transmission electron microscopy (HR-TEM) analysis

TEM images of the hydrothermally synthesized ZnONPs are shown in Figure 5.2, and there is moderate monodispersity in the ZnONPs dispersed in ethanol before TEM analysis. There is an evident aggregation of nanoparticles which contribute to large diametrical sizes. The conditions under which the nanomaterials are synthesized

significantly affect properties such as size and morphology. In one of the ZnONPs synthesis review, it was deduced that the aggregation is at its optimum under the aqueous synthesis of ZnONPs (Becheri *et al.* 2008). The rectangle highlighted area was analysed using ImageJ software for particle size.

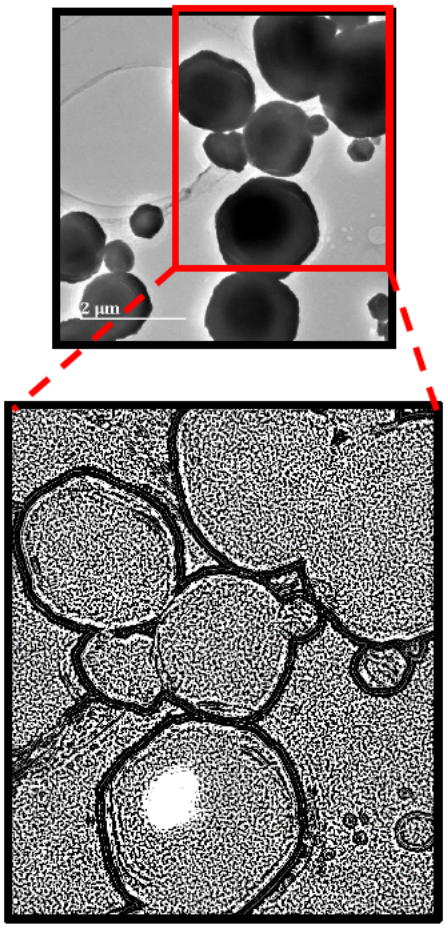

Figure 5-2: High-resolution transmission electron microscope image of hydrothermally synthesized ZnONPs viewed and calibrated by ImageJ.

(iii) UV-Visible spectroscopy analysis

The optical properties of the newly synthesized ZnONPs were studied using UV-Vis spectroscopy from the wavelength range of 200 to 800 nm. It is reported that the maximum light absorption of bare ZnONPs is expected from around 300 to 395 nm (Song *et al.* 2016). The experimental band gap of the synthesized ZnONPs was deduced by linear extrapolation from the absorption peak in the UV Spectrum to be

3.22 eV, which is in good agreement with the ZnONPs energy band gaps previously reported by literature and by (Javed *et al.* 2017). Figure 5.3 displays the linear extrapolation to obtain the energy band gap of ZnONPs.

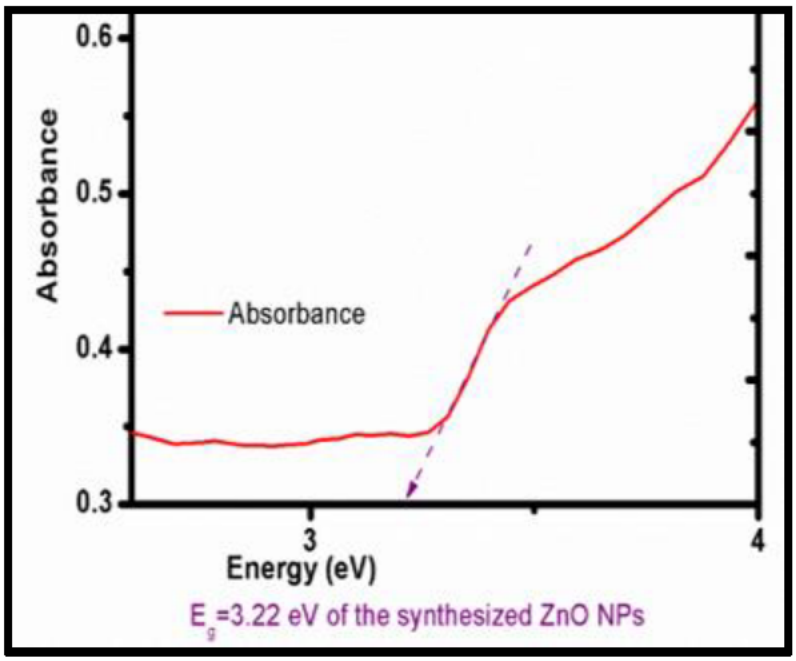

Figure 5-3: Uv-visible absorption spectrum of hydrothermally synthesized ZnONPs from 200 to 800 nm was used to obtain the optical energy band gap to be 3.22 eV.

(i) Thermogravimetric characterization analysis

Thermogravimetric profiles of hydrothermally synthesized ZnONPs through employing a pressure cooker together with nanomaterials (GO,MWCNTs) used for electrode modification are presented in Figure 5.4 [a] and [b], respectively. The thermal stability and behaviour of ZnONPs and nanomaterial used for electrode modification were studied by thermogravimetric analysis. The TG curve ascends from the temperature onset until it reaches 172 ^{0}C. The TG profile illustrates three weight loss intermediates upon obtaining the pure phases of ZnONPs. Theoretically, there is an expected 22% weight loss attributed to the physically adsorbed water from the temperature range of 50 to 135 ^{0}C (Zak *et al.* 2011). The resulting weight loss amounting to 2.10% is attributed to chemically bound functional groups, the TG profile then levels up to around 540 ^{0}C.

[a] [b]

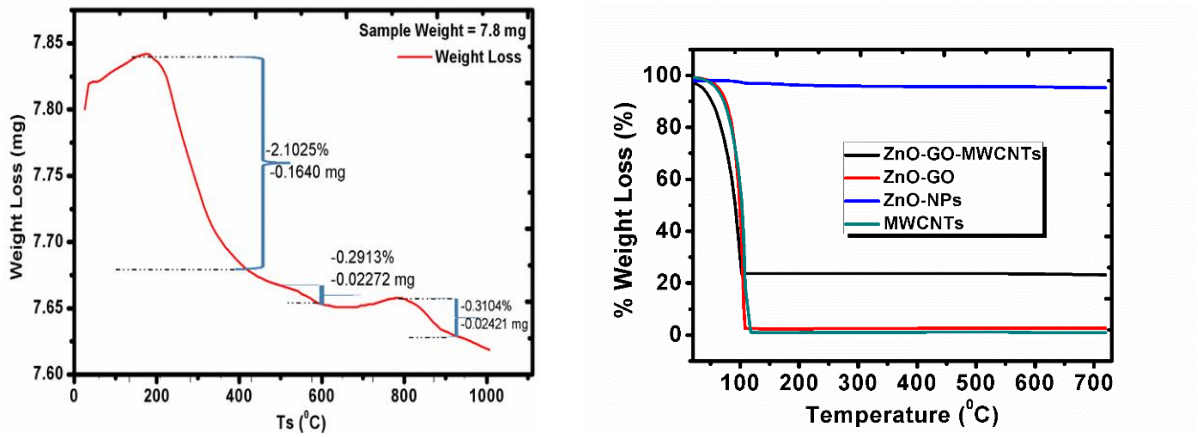

Figure 5-4: [a]: TGA analysis of ZnONPs synthesized by electric pressure cooker assisted hydrothermal method. **[b]:** TGA analysis of ZnONPs synthesized by electric pressure cooker assisted hydrothermal method, bare MWCNTs, ZnONPs/GO nanocomposite, and ZnONPs/GO/MWCNTs nanocomposite used in Pt-E modification for Reb A detection.

(ii) Field flow fractionation characterization analysis

Field flow fraction's subsection asymmetric field flow fractionation (AF4) was employed for hydrodynamic diameter characterization of ZnONPs. Prior analysis of the synthesized ZnONPs samples, the separation efficiency of the instrument and coupled detectors (UV detector and MALS detector) was tested via a mixture of Latex particle calibration. All fractograms were recorded using both UV and MALS detector in a 0.2 % Novachem100 as the dispersion surfactant and the high separation ability for AF4 is presented as overlay fractograms of Latex particle mixture in Figure 5.6 [a]. The linear calibration of Latex particles versus Retention Times is presented in Figure 5.6 [b], with an R^2 value of 0.9861.

Calibration of MALS detector with latex standards:

[a] [b]

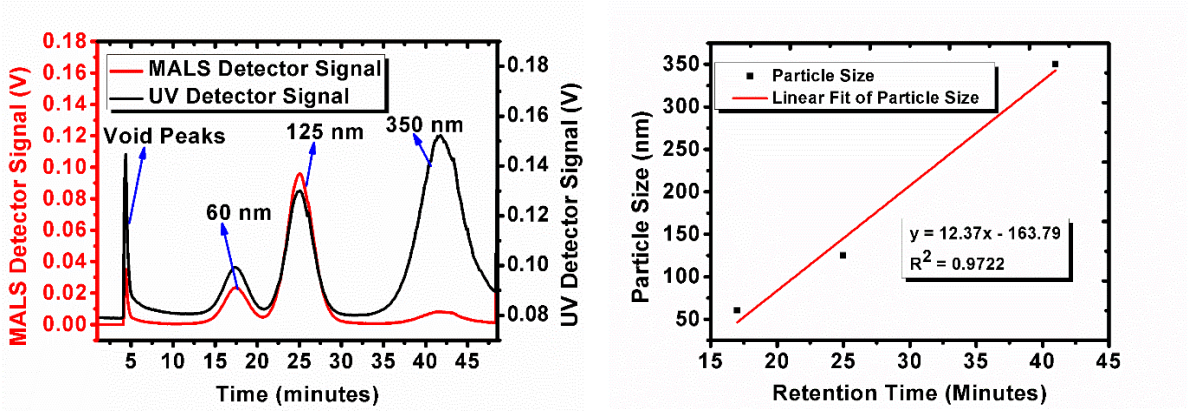

Figure 5-5: [a]: Overlay of triplicate FFF(AF4)-UV and MALs fractograms of Latex calibration standards with 60 nm, 125 nm, and 350 nm particle sizes. AF4 separation conditions were 1.0 mL/min channel flow and 1.0 ml/min crossflow. **[b]:** linear regression calibration function using 60, 125, and 350 nm Latex Standards showing retention times related to particle sizes obtained from UV detector at 280 nm wavelength in 0.2% NovaChem100 surfactant.

The experimental radius of gyration (R_g)values for the different sized Latex mixtures were obtained after integrating the different regions of interest, fitting a sphere calibration curve. Table 5.1 displays the theoretical and experimental R_g values of the different sized (60, 125, 350 nm Latex standards.

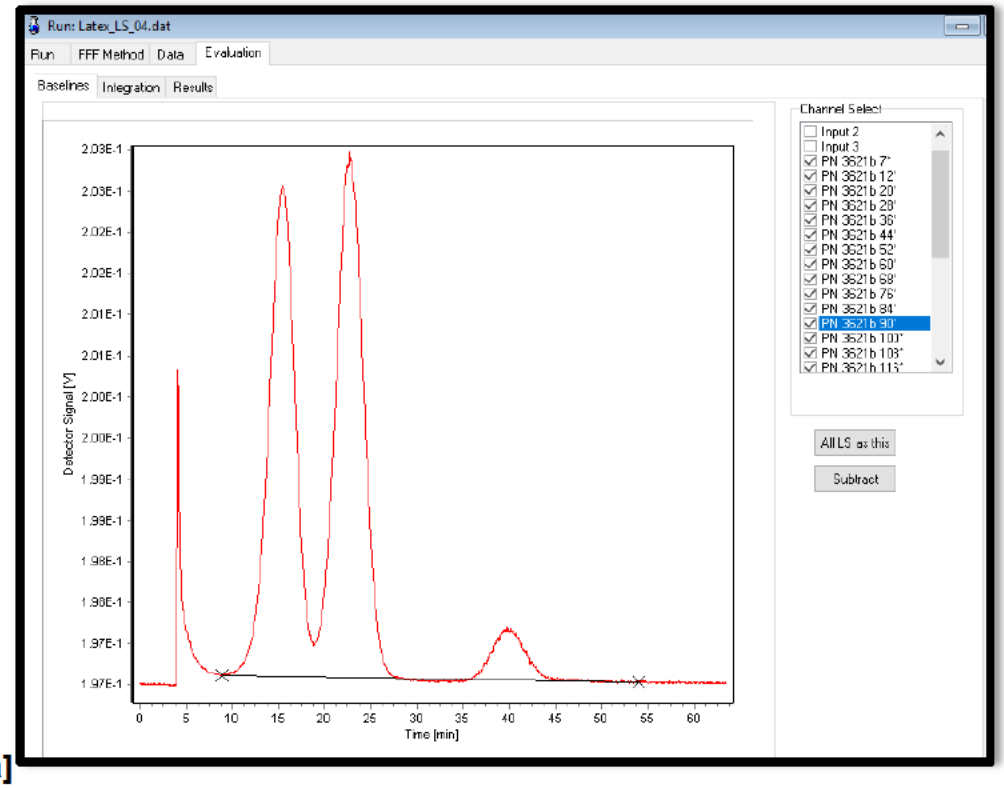
Run: Latex_LS_04.dat
Run
FFF Method
Data
Evaluation
Baselines
Integration
Results
Channel Select
Input 2
Input 3
PN 3621b 7°
PN 3621b 12°
PN 3621b 20°
PN 3621b 28°
PN 3621b 36°
PN 3621b 44°
PN 3621b 52°
PN 3621b 60°
PN 3621b 68°
PN 3621b 76°
PN 3621b 84°
PN 3621b 90°
PN 3621b 103°
PN 3621b 113°
All LS as this
Subtract
Detector Signal [V]
Time [min]

[a]

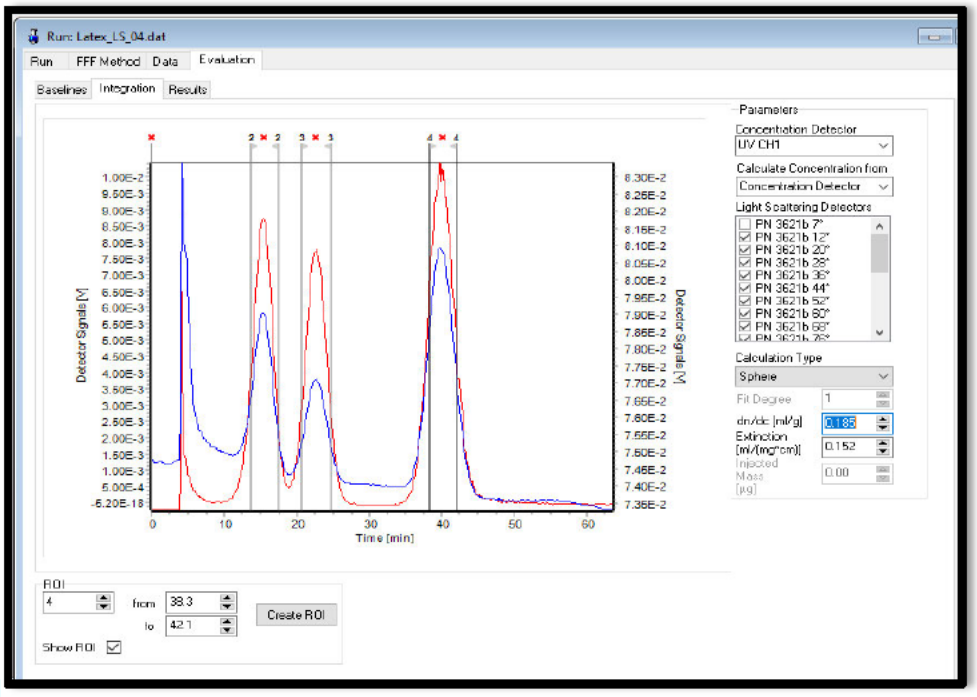
Run: Latex_LS_04.dat
Run
FFF Method
Data
Evaluation
Baselines
Integration
Results
Parameters
Concentration Detector
UV CH1
Calculate Concentration from
Concentration Detector
Light Scattering Detectors
PN 3621b 7°
PN 3621b 12°
PN 3621b 20°
PN 3621b 28°
PN 3621b 36°
PN 3621b 44°
PN 3621b 52°
PN 3621b 60°
PN 3621b 68°
Calculation Type
Sphere
Fit Degree
dn/dc [ml/g]
Extinction [ml/(mg*cm)]
Injected Mass [µg]
ROI
from
to
Create ROI
Show ROI
Detector Signals [V]
Time [min]

[b]

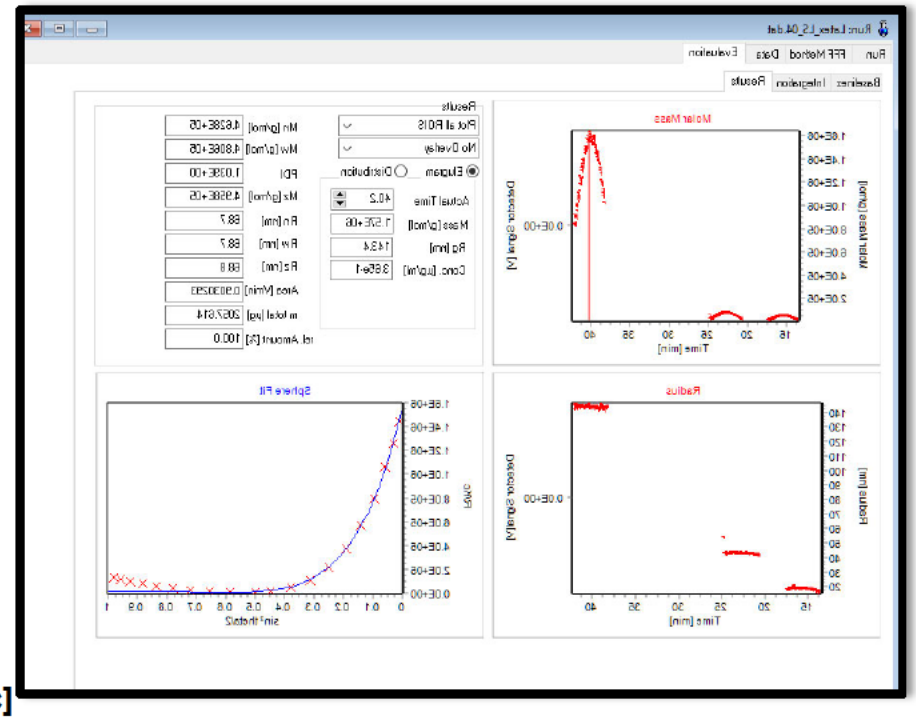

[c]

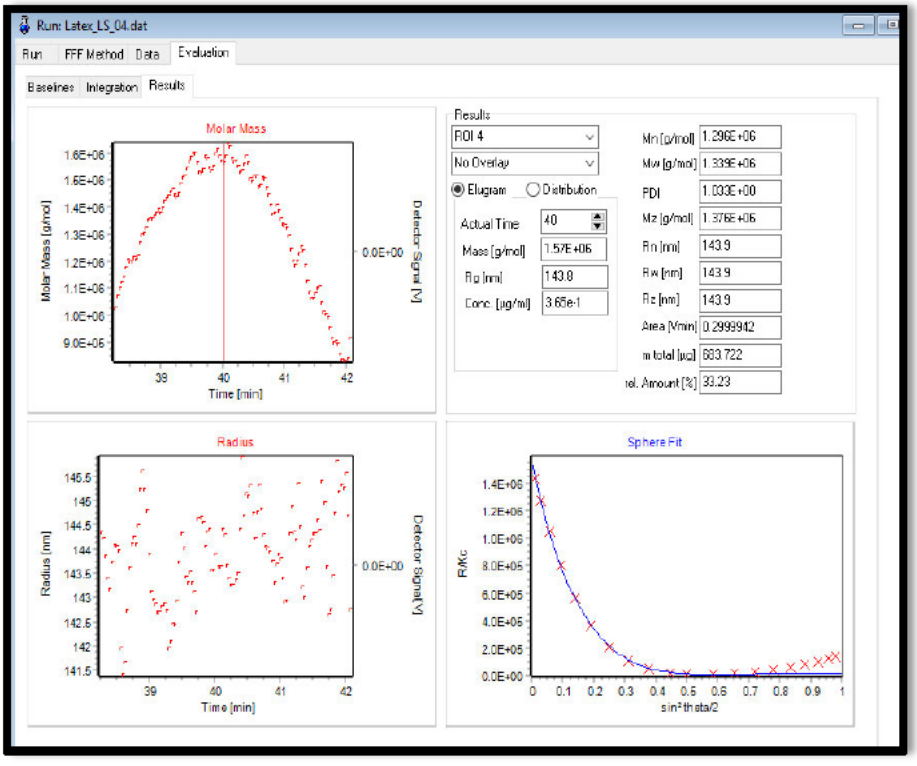

[d]

Figure 5-6 : [a]: Opened the evaluation file showing how to draw a baseline prior integration. **[b]:** Integration sheet showing regions of interests (ROIs), where further evaluation is performed within defined ROIs. **[c] and [d]:** Results sheet, showing results tab for the performed analysis in the elution mode.

Table 5-1 : Latex calibration standards of 60, 125, and 350 nm different particle sizes summarized.

Latex	Hydrodynamic diameter (nm)	Hydrodynamic radius (nm)	Radius of gyration (nm)	Rg (exp) (nm)
L60	60	30	23.3	19.3
L125	125	62.5	48.4	43.1
L350	350	175	135.6	143.9

In this case, the measured size of ZnONPs is slightly higher in AF4 compared with ZnONPs ICP-MS, discussed shortly after this sub-heading. The difference in sizes is attributed to the technique measuring hydrodynamic diameter as opposed to the particle diameter(Poda *et al.* 2011). Figure 5.10 shows an AF4-UV detector fractogram of hydrothermally synthesized ZnONPs After integration of the region of interest in a random coil fitting calculation type curve, the experimental radius of gyration was found to be 46 nm and diameter of gyration equalling to 118 nm.

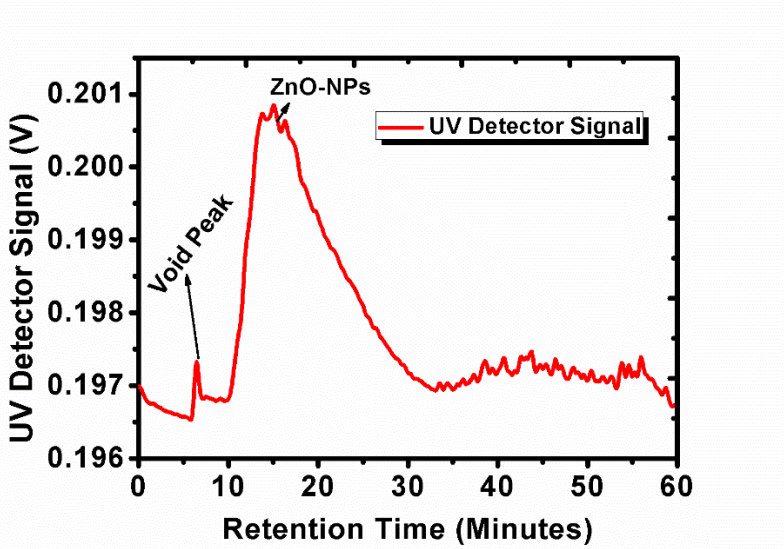

Figure 5-7 : AF4 UV fractogram of hydrothermally synthesized ZnONPs, the separation conditions were 1.0 ml/min Crossflow and 1.30 ml/min Focus pump flow.

(iii) Inductively Coupled Plasma analysis

Inductively coupled plasma was used for the size characterization of ZnONPs. ICP-MS size distribution histograms for the calibration using ZnONPs dissolved standard and for hydrothermally synthesized ZnONPs are seen in the Figures, 5.8 and 5.9, respectively. The 70 nm ZnONPs standard used for calibration was diluted in a ratio of 1: 100000, whereas the synthesized ZnONPs were diluted in a 1: 10000, using ultra-pure water (Donovan *et al.* 2016). For calibration, the size stated by the manufacture for ZnONPs standard was 70 nm, and after sonication to reduce aggregation, and the most frequent and mean size of 71 nm and 74.45 nm. For the synthesized NPs, the most frequent and mean size obtained by ICP-MS were 93 nm and 90.88 nm, respectively.

In Sigle-particle ICP-MS analysis, the major difficulty faced by researchers is the inability to measure nanomaterials less than 20 nm in size. This is not the case with PerkinElmer's NexION® 2000 ICP-MS, as it is equipped Syngistix™ Nano Application Software Module, with a distinguished RF generator, being able to measure nanoparticles less than 10 nm even when in mixtures.

Sample	Analyte	Most Freq. Size (nm)	Mean Size (nm)
Zn 70 nm STD	Zn 65.926	71	74.45179

[a] [b]

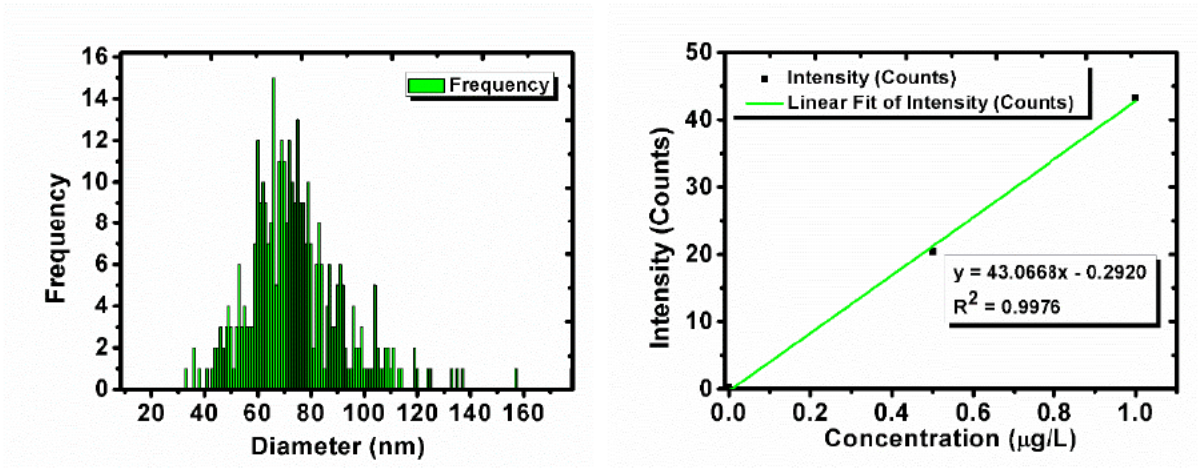

Figure 5-8 : [a]Size distribution histogram for ZnONPs dispersion Type A-Nonionic 70 nm standard using dissolve calibration with the most frequent and mean sizes of 71 nm and 74.45 nm, respectively . **[b]** particle calibration for 70 nm ZnONPs STD.

Sample	Analyte	Most Freq. Size (nm)	Mean Size (nm)
Zn Sample 1 10000	Zn 65.926	93	90.87952

[a] [b]

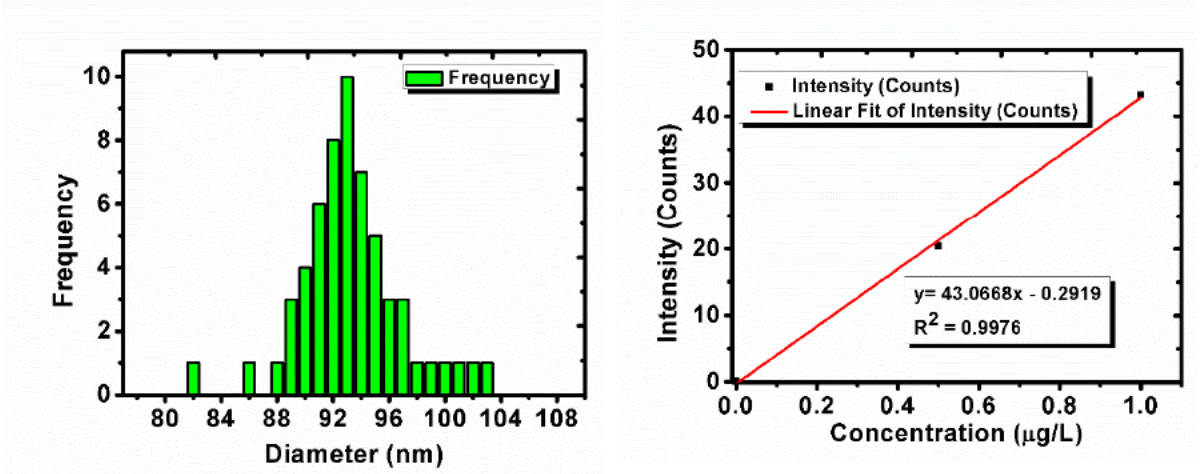

Figure 5-9: [a]: Size distribution histogram for the synthesized ZnONPs with the most frequent and mean sizes of 93 nm and 90.88 nm using dissolved calibration. **[b]:** Particle calibration of the synthesized ZnONPs.

5.1.2 Electrochemical characterization behaviour of ZnONPs

The main aim of this study was to develop an electrochemical sensor for detection Rebaudioside A. Cyclic voltammograms of 100 mg/L Reb A are presented in Figure 5.10, at bare Pt electrode against the ZnONPs/MWCNTs/GO/T1R2 modified Pt-E pH 11.0 in aqueous 0.1 M borate buffer. Redox properties of Reb A were studied by applying the bare and modified Pt-Es. In Figure 5.10, it is evident from current-potential responses, that there are low oxidation and reduction peak currents when sensing Reb A, using bare Pt-E compared to when the working electrode is modified with the ZnONPs/MWCNTs/GO/T1R2 nanocomposite.

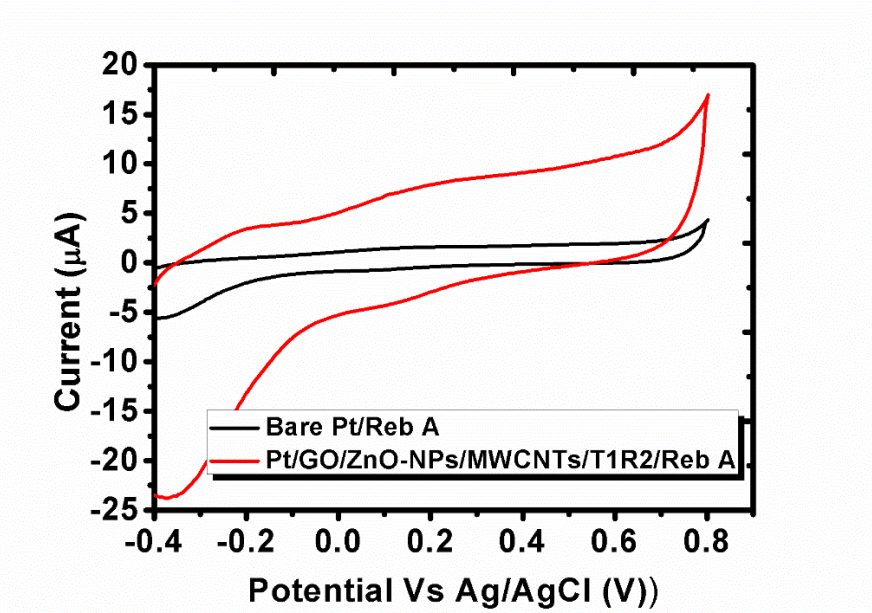

Figure 5-10 : Cyclic voltammogram of 100 mg/L Reb A in pH 11.0 0.1 M borate buffer solution at a bare Pt electrode and T1R2/ZnONPs/MWCNTs/GO/Pt-E.

i. Characterization of GO/ZnONPs/T1R2/Pt-E

Comparative cyclic voltammograms of different electrodes under this study, showing oxidation peak currents of Reb A are displayed in Figure 5.11. The analytical peak of Reb A in Figure 5.11 is evident at 0.2 V vs Ag/AgCl with the bare Pt electrode and a

slight shift to more negative potentials vs Ag/AgCl The bare Pt electrode showed a broad and weak peak intensity of Reb A response compared to the well distinct analytical peaks of the modified electrodes. According to literature (Bathinapatla et al. 2016) the analytical peak attributed to the reverse reduction of the carboxyl group was observed at -0.1 V vs Ag/AgCl. The difference in surface areas of the bare and modified platinum electrode was studied using 100 mg/L Reb A solution at pH 11.0 in the presence of 1 M $K_3[Fe(CN)_6]$ as the redox mediator solution. The ferro/ferricyanide redox couple is amongst the most studied in electrochemistry and is identifiable by on heterogeneous electron transfer with n = 1 (Bathinapatla et al. 2016).

The electro-active surface of the modified electrode can be estimated by using the $K_3[Fe(CN)_6]$ probe solution employing and following Randles-Servick equation (Kaur *et al.* 2013) :

$$I_p = 2.69 \times 10^5 \times A \times D^{1/2} \times n^{3/2} \times v^{1/2} \times C \qquad \textbf{(Eqn 5.1)}$$

Where symbols have their usual meanings, with I_p referring to the peak current, n being the number of electrons transferred in the reaction, A is the electroactive area (cm^2), D is the diffusion coefficient of the bulk concentration of the redox probe (cm^2/s), *v* is the scan rate (V/s) and C is the concentration of the probe molecule in the bulk solution (mol/cm^3s).

The cyclic voltammetry analysis of Reb A in the scan rate from 0.01 V/s to 0.2 V/s, linearly increased anodic and cathodic peak heights, whereas the anodic peak potentials were shifted to the right. The concentrations of the electroactive species (Γ) were deduced from the slope of the plot of anodic and cathodic currents versus the scan rates, according to the following equation:

$$I_p = \frac{n^2 \times F^2 \times A \times \Gamma \times v}{4 \times R \times T} \qquad \textbf{(Eqn 5.2)}$$

Where I_p represents peak current, n is the number of electrons that are partaking in the reaction, with F being the Faraday's constant, A is the geometric surface area of the working electrode (cm^2), Γ (mol/cm^2) refers to the surface coverage, *v* is the scan rate (V/s), R is gas law constant (L×atm/mol×K) and the temperature at K. The concentration of the electroactive species at the surface of the modified working electrode is determined from the slope of the anodic current versus scan rate.

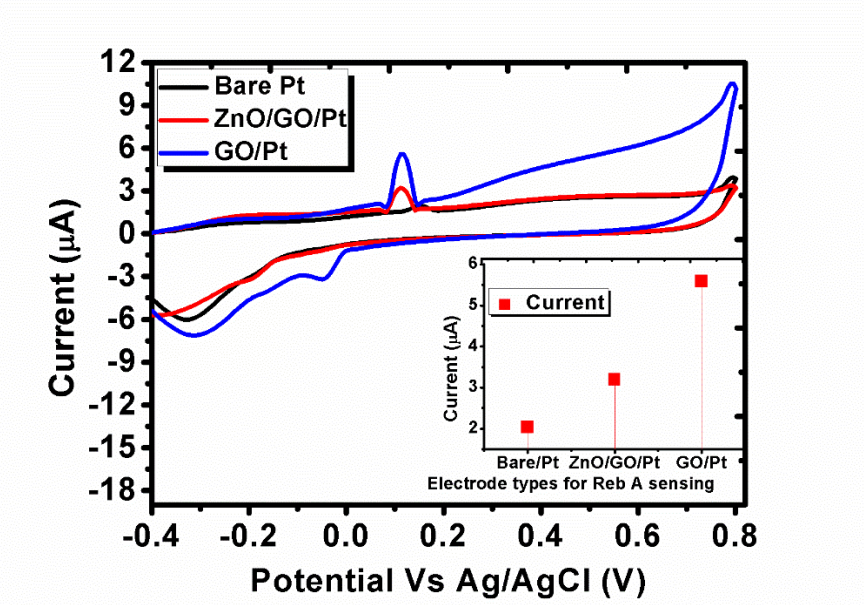

Figure 5-11 : Current-potential responses of Reb A at the different modified Pt-E's.

1. Effects of pH and scan rate at peak current and position

Cyclic voltammetry is a powerful technique for qualitative analysis of electroactive compounds. In this study, prior to quantification of Reb A with the developed electrochemical sensor under DPV mode, cyclic voltammetry is employed in determining optimum parameters such as pH and scan rates for effective of Reb A.

A 0.1 M borate buffer supporting electrolyte in a pH range of 4.0 to 11.0 was used to study the changes on the peak current and peak potential of Reb A on the modified working electrode. There is a gradual increase in peak current as the pH of the electrolyte is increased, with pH 11.0 of 0.1 M borate buffer being the optimum pH for further analysis. The lower concentration of hydronium ions in more basic medium resulted in less interference with the carboxylic reduction peak. This motivated the study to be carried out in pH 11 borate buffer due to high electron transfer and less interference. The pH of the supporting electrolyte also has a direct effect on the peak potential of the electroactive species to be analysed, this was evident on this study, as the anodic peak potential shifted to the right and cathodic peak shifted to the left when the supporting electrolyte pH was ramped from lower to higher values. Figure 5.12 graphically represents the pH effect on peak current and potential of Reb A against the modified electrode. The changes in the peak current and the potential of Reb A are attributed to the reduction abilities of the carboxylic group within the structure. The reduction capacity of carboxyl group is highly pH dependent, hence there is a shift in peak potentials with the change in pH of the supporting electrolyte (Bathinapatla *et al.* 2016).

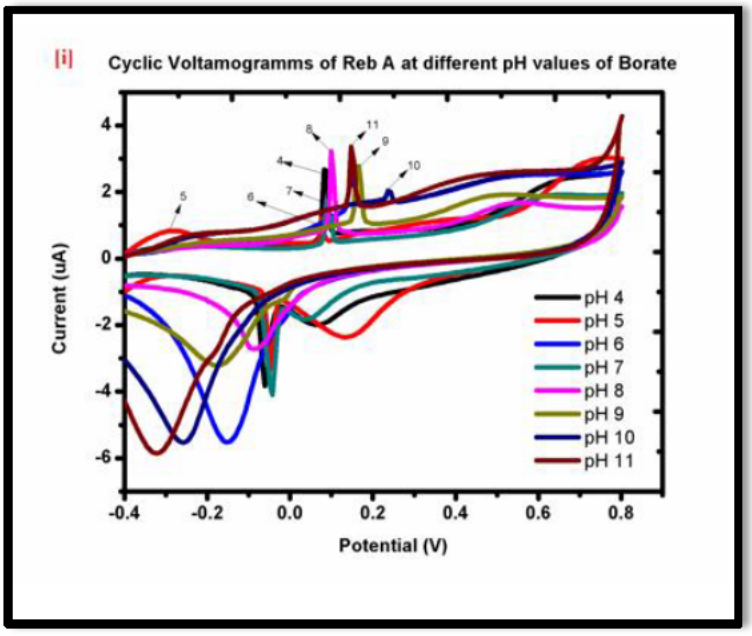

[i]

[ii]

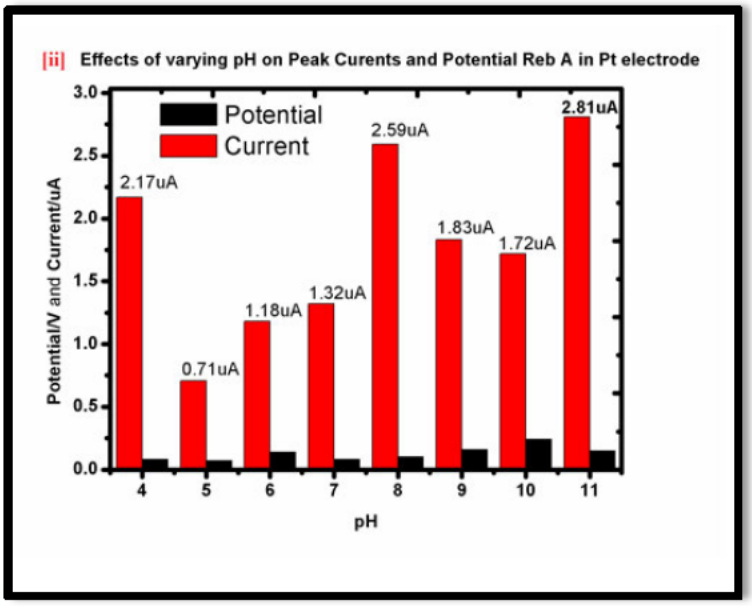

Figure 5-12: [i]: Cyclic voltammograms of Reb A recorded at different pH values of 0.1 M borate buffer with 100 mg/L Reb A standard on recorded at platinum electrode modified with T1R2/ZnONPs/MWCNTs/GO/Pt-E nanomaterial. **[ii]:** Graphical representation of the dependence of oxidation peak current of Reb A on T1R2/ZnONPs/MWCNTs/GO/Pt-E immunosensor.

The effect of the scan rate on the peak current and potential of Reb A was investigated using 100 mg/L Reb A in 0.1 M borate buffer at 11.0. Figure 5.13 shows cyclic voltammograms of 100 mg/L at Pt/GO/T1R2 working electrode displaying scan rates ranging from 0.01 V/s to 0.2 V/s. As the scan rate is increased, the oxidation and reduction peak current increase linearly as the scan rates are ramped from 0.01 V/s to 0.2 V/s. The shifts in anodic peak potential to the more positive potentials and in cathodic peak potentials to the fewer negative potentials were observed as the sweep rate was increased from 001 V/s to 0.2 V/s. This linear relationship between the scan rate and the oxidation peak current of Reb A is indicating that the electrochemical behaviour of Reb A at the modified surface is adsorption controlled. This direct proportionality is confirmed by the regression coefficient (R^2) equalling to 0.99317 with the regression equation of y = 12.807x + 0.25343.

[i] [ii]

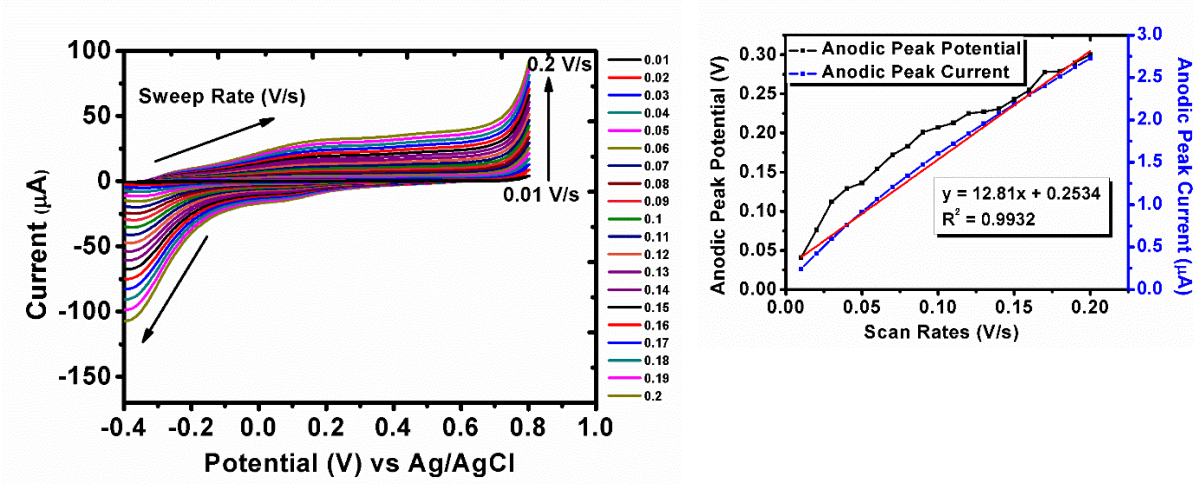

Figure 5-13 : [i] Cyclic voltammograms of Rebaudioside A at pH 11.0 borate buffer from 0.01 V/s to 0.02 V/s scan rates **[ii]** Graphical representation of the dependence of oxidation peak current and potential of Reb A on different scan rates (0.01 V/s to 0.2 V/s) of Pt/GO/MWCNTs/T1R2 immunosensor.

ii. Electrochemical behaviour of GO/T1R2/Pt on Reb A

The electrochemical and catalytic behaviour of reduced graphene oxide with immobilized T1R2 was investigated by measuring current responses of Reb A as the result of applied potential. The three-electrode system comprised of Ag/AgCl as the reference electrode, counter electrode as graphite and the platinum working electrode was modified with hydrophobic reduced graphene oxide and multi-walled carbon nanotubes. The catalytic capabilities of the nanocomposite were investigated through qualitative and quantitative electrochemical techniques, that is cyclic voltammetry and differential pulse voltammetry, respectively.

5.1.3 Quantification of Rebaudioside A

Differential pulse voltammetry (DPV) is an analytical tool comprising of advantages such as short pulse time and sensitivity for both quantitative analysis and understanding chemical reaction kinetics, thermodynamics, and mechanisms. In this study, because of its sensitivity, DPV was used to accurately quantify Reb A at GO/T1R2/Pt and under optimized electrochemical parameters (pH 11.0, scan rate: 0.09 V/s, and deposition time: 40 s)

The DPV measured current responses as a result of applied potential in 0.1 M borate buffer at pH 11 for different concentrations of Reb A at the modified working electrode. Figure 5.14 displays anodic peak currents of concentrations from 0.1996 mg/L to 1.5748 mg/L at 0.2 V vs Ag/AgCl with a linear relationship between anodic currents and the change in Reb A concentration, with a linear regression equation of I_{pa} = -0.9913x + 7.1462 and R^2 value of 0.9729. The LOD and LOQ for this developed method were found to be 0.6346 mg/L and 1.923 mg/L indicating the ability and effectiveness of the developed method for electrochemical sensing of Reb A. When indirect quantification of the analyte of interest is employed, the anodic/cathodic peak current is noted to decrease with the increase in analyte concentration.

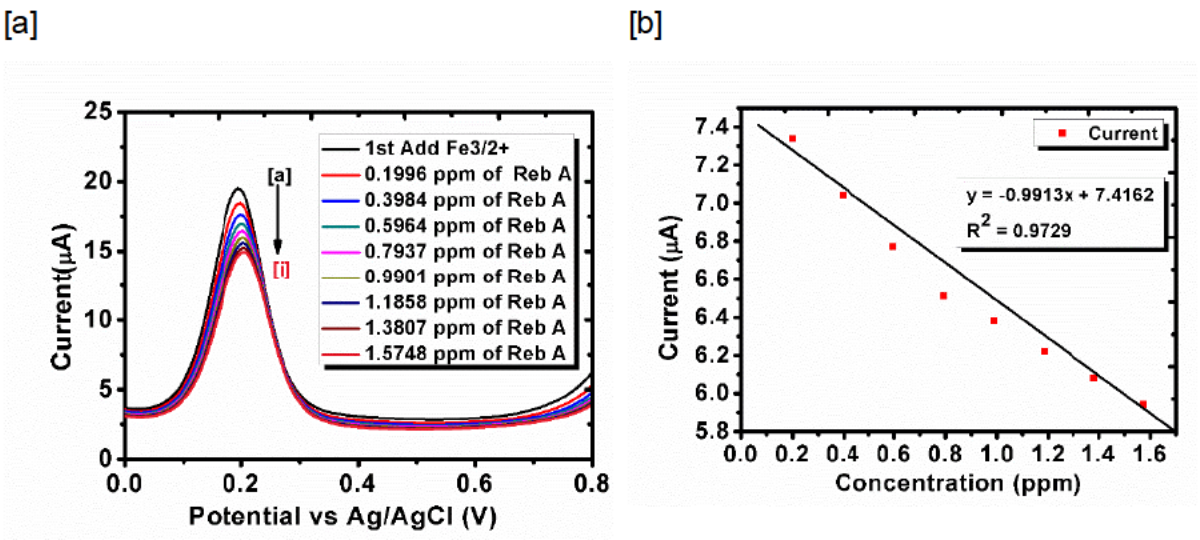

Figure 5-14: [a]: DPV of Reb A at pH 11.0 borate buffer using Pt/GO/T1R2 immunosensor. **[b]:** Graphical representation of the linear relation between the concentration of Reb A and Oxidation peak current.

Figure 5.15 illustrates step by step fabrication of the bare Pt-E into the fully modified electrochemical immunosensor for the detection of Reb A. The top view of the schematic representation details mechanism of detection undergone by Reb A through the unstable carbonyl system of the structure.

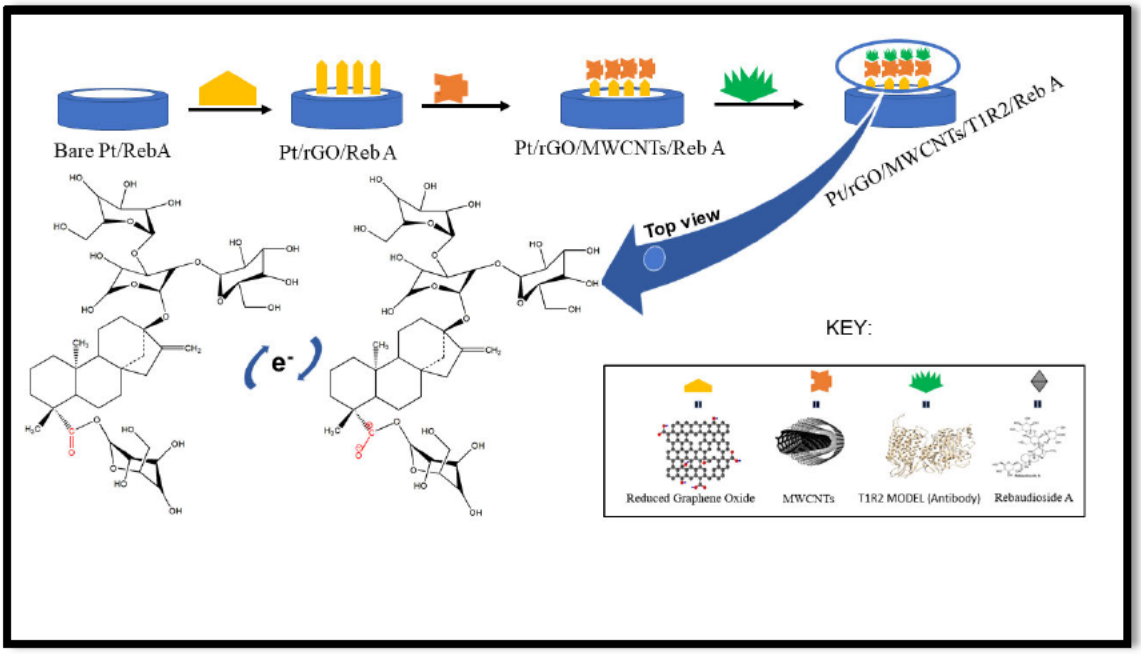

Figure 5-15: Bare Pt-E modification with nanocomposite with the mechanism illustrating electrochemical behaviour of Reb A.

5.1.3.1 The linearity and sensitivity of electrochemical immunosensor

The developed electrochemical immunosensor was exposed in different concentrations of Reb A ranging from 0.1996 to 1.5748 ppm. The increase in concentration of Reb A resulted in inverse proportionality in current as depicted in figure 5.16 [b]. Differential pulse voltammetry method was used for quantifying Reb A. The measure current response as potential is applied potential linearly decreased with R^2 of 0.9687.

[a] [b]

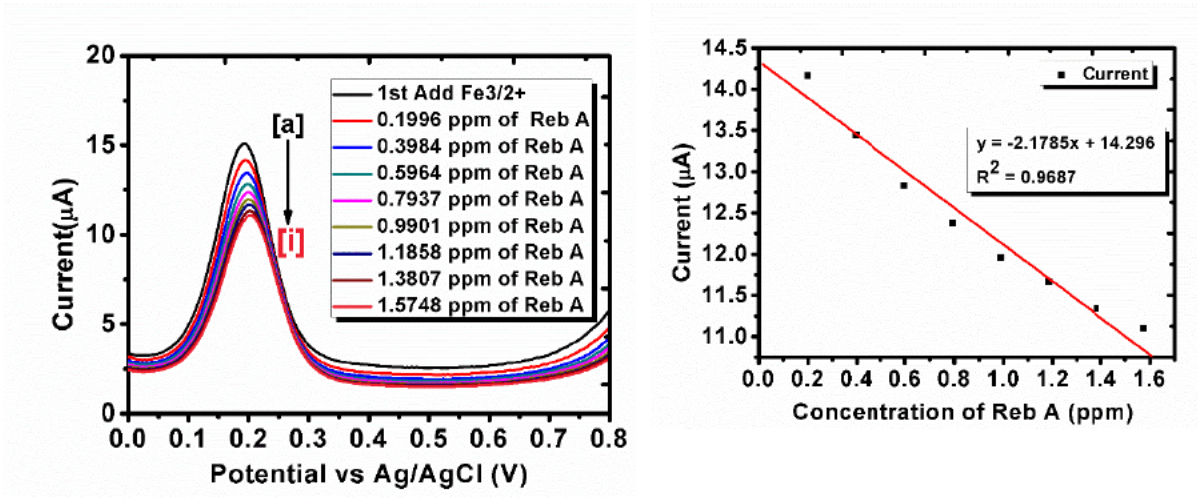

Figure 5-16: [a]: DPV of Reb A at pH 11.0 borate buffer using Pt/GO/MWCNTs/T1R2 immunosensor, **[b]:** Graphical representation of the linear relationship between the concentration of Reb A and Oxidation peak current, with fairly low limits of detection and quantification

5.2 Computational modelling and Simulation

5.2.1 Homology Modelling

The human sweet taste receptor generated is represented as a 3-D structure as shown in Figure 5.17 [a], the 3-D structure of T1R2 was further subjected to optimization tools for energy minimization and the active sites were determined and validated using Site-Hound web programme (Xie and Hwang 2015). Thereafter, the stereo-chemical qualities of the predicted structures were assessed using the Ramachandran plots in Maestro Schrodinger suite, affirming the validation of the homolog as shown in Figure 5.17 [b].

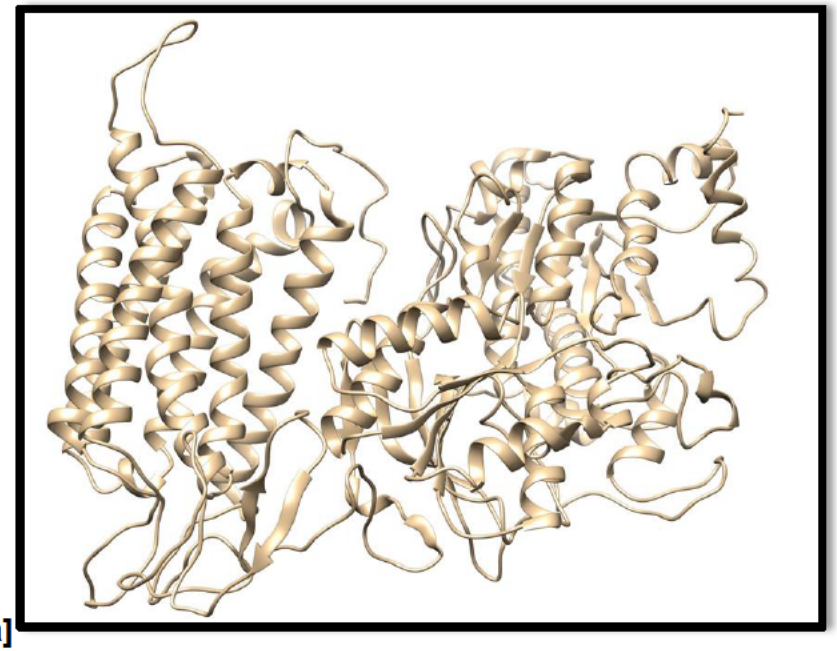

[a]

[b]

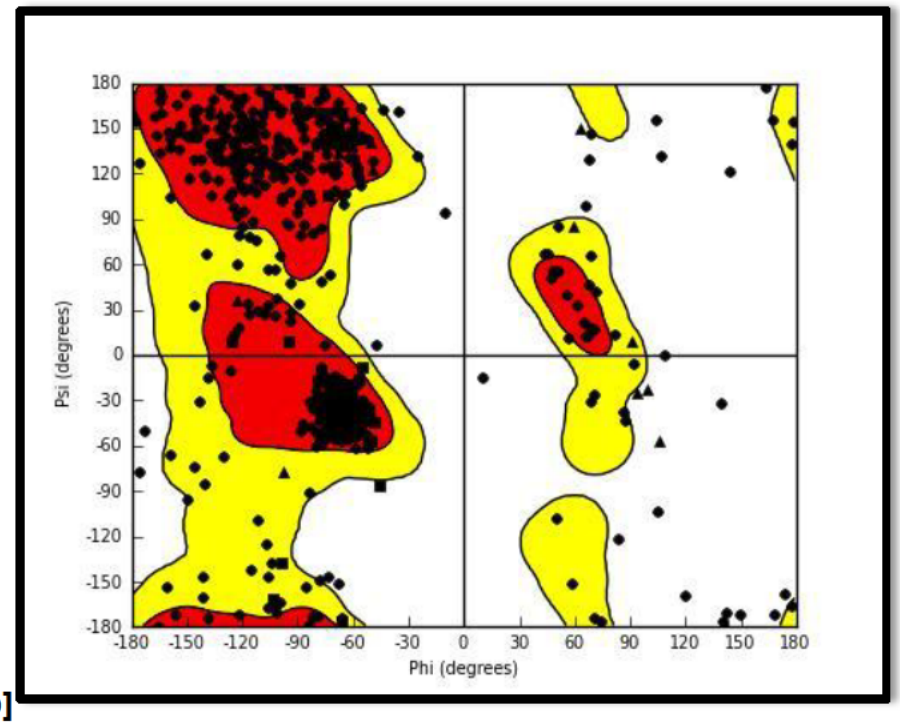

Figure 5-17: [a]: Homology model of the Human Taste Receptor 1 (T1R2) containing 839 amino acid residues. **[b]:** The Ramachandran Plot of the Human Taste Receptor 1 homolog.

Closest active sites were selected and used for further modelling studies. The MolProbity structure validation tool was employed to validate the model (Guex and Peitsch 1997), showing that 86.7 % (i.e. 726 out of 827 residues) were in the favoured regions while 94.9 % (i.e. 794 out of 837 residues). were in the allowed region, which left a list of 5 % outliers (i.e. 43 out of 837 residues). None of the employed active sites for modelling in this study are part of the mentioned outliers, thus providing solid evidence that the predicted 3D structure of the human T1R2 is of a good quality.

5.2.2 Molecular Docking

Molecular Docking studies were based on Protein-Ligand docking using Auto-dock to predict predominant molecular binding sites between protein (T1R2) and ligand (Reb A). Auto-dock uses the “search and score” grid-base method where T1R2 was held

RIGID while Reb A was allowed to be flexible around the ligand. Figure 5.18 below shows protein-ligand complex for molecular docking through Autodock.

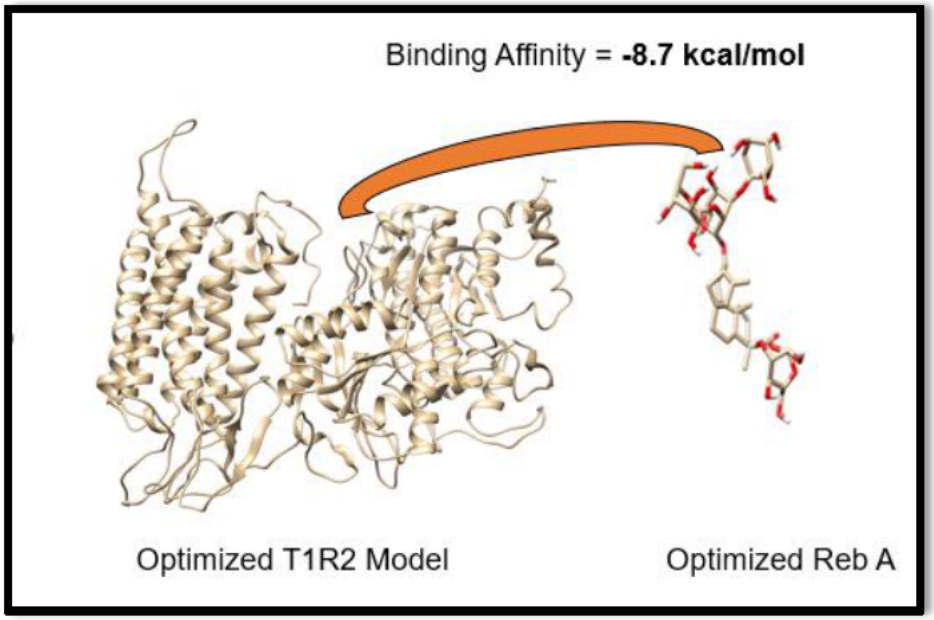

Figure 5-18 : Protein-Ligand model by Auto-dock.

In our docking simulation, The human T1R2 homolog was docked onto Reb A, retrieved from the ZINC database (National Center for Biotechnology Information 2019), and docked into the predicted binding site of the human T1R2 homolog–using Autodock Vina (Trott and Olson 2010). This software performs the prediction of the bound conformation based on free energy, which was calculated on the basis of the empirical force field and the Lamarckian Genetic Algorithm (Morris *et al.* 2009).

Docking studies performed between Reb A and human T1R2 Homolog indicated the strong binding affinity displaying a mutual host-guest relationship with a binding affinity of -8.7 kcal/mol as shown in Figure 5.18. Reb A also showed strong binding affinity human T1R2 when docked against both Homolog models of T1R2 and T1R2 subunits of human sweet taste receptors (Mayank and Jaitak 2015). This is how molecular modelling was used to substantiate the use of T1R2 human sweet taste receptor as

the biological recognition element immobilized on the surface for the working electrode for electrochemical immunosensing of Reb A.

5.2.3 Molecular Dynamic (MD) simulations

5.2.3.1 Simulation preparation and optimization

All atom molecular dynamics simulations have been performed on the docked complexes using AMBER 18 molecular dynamics package (Cornell *et al.* 1996; Case *et al.* 2005). The bonded and non-bonded description of the interactions between the various atoms has been described using the AMBER 18 force fields, which include the GAFF (Nerenberg and Head-Gordon 2018) force field parameters. Due to the lack of parameters needed for the ligand (Reb A) in the Cornell *et al.* force field (Cornell 1995), the missing parameters were created. Optimization of the Reb A was performed at the HF/6-31G* level with the Gaussian 03 package (Frisch MJ *et al.* 2004). The standard AMBER force field for bioorganic systems (ff03) (Duan *et al.* 2003) was used to define the topology and parameter files for the protein and Reb A using "GAFF" (Wang *et al.* 2004b) force field parameters based on the atom types of the force field model developed by Cornell *et al.* (Cornell *et al.* 1996). The topology and coordinate files were generated using the antechamber module of AMBER 18, and the missing hydrogen atoms were added and saved for the protein using the LeaP module inside AMBER 18. Thereafter, the docked T1R2-Reb A complex was solvated in the octahedron box of the TIP3P water model (59), as well as the neutralization, which was performed by adding the counterions to mimic the biological environment more closely. Cubic periodic boundary conditions were imposed, and the long-range electrostatic interactions were treated with the particle-mesh Ewald method implemented in AMBER 18 with a non-bonding cut-off distance of 10 Å.

The system stability and overall convergence of simulations were monitored in terms of Root Mean-Square Deviation (RMSD) and potential energy of the protein backbone atoms. The RMSD and potential energy enabled us to verify that equilibration was achieved as illustrated in Figure 5.19.

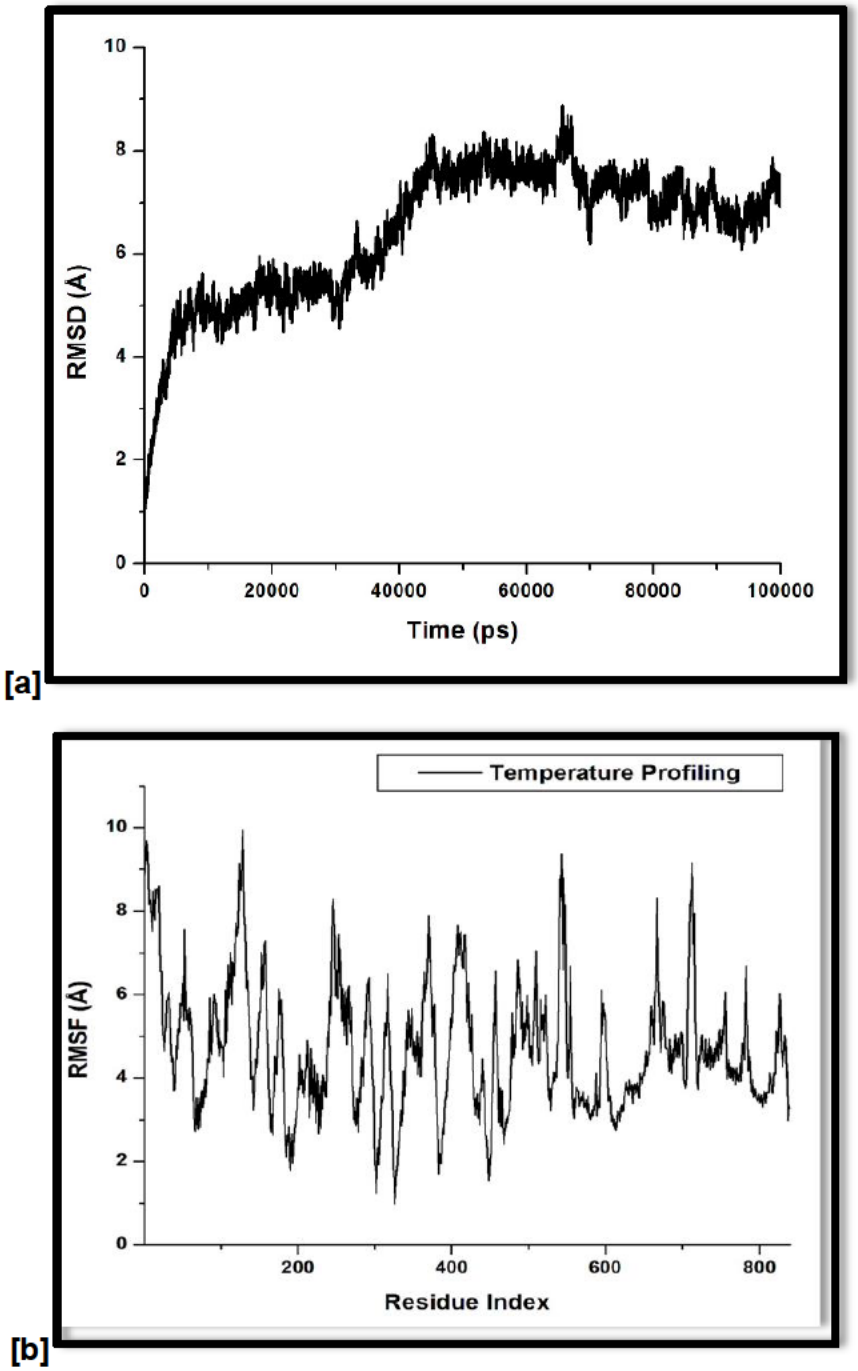

Figure 5-19:[a] Root Mean Square Deviation (RMSD) and **[b]** Root mean Square Fluctuation (RMSF) plots of the T1R2-Reb-A complex.

Here, the system was well equilibrated where the RMSD value of the system did not all exceed 1Å after stabilising at approximately 15000 ps. The Root Mean Square

Fluctuations (RMSF) of the average structure from the trajectory reports the residue and atomic fluctuations to check if the simulation results are in accordance with the crystal structure. The RMSF plot shows the temperature profiles of each amino acid residue.

The interaction of biomolecules and nanostructures employed in the layer-by-layer fabrication of the proposed immunosensor for Reb A were understood at a molecular level by calculating adsorption energies. The most stable system being GO/MWCNTs whereas the least stable system was GO/ZnONPs with the corresponding adsorption energies of -170.45 kcal/mol and -13.85 kcal/mol, respectively (Table 5.2). The GO/Reb A system was relatively stable with an adsorption energy of -47.94 kcal/mol, whereas the system stability was lowered by the introduction of ZnONPs (-44.57 kcal/mol).

Table 5-2: Layer-by-layer fabrication in the development of the GO/MWCNTs/ZnO/T1R2/Reb A with corresponding adsorption energies in kcal/mol

System	ΔG (Adsorption energy) kcal/mol
GO/Analyte	-47.940
GO/MWCNTs	-170.447
GO/ZnO (1 Np)	-116.161
GO/ZnO (10 Nps)	-13.852
GO/MWCNTs/ZnO(10Nps)	-76.642
GO/ZnO/Reb A	-44.568
GO/MWCNTs/ZnO/Reb A	-63.539
GO/Antibody/Analyte	-38.3258
GO/MWCNTs/ZnO/T1R2/Reb A	-44.286

The following Figures 5.20 to 5.26 are 3D representations of the systems viewed in various representations, using Material Studio along with their corresponding adsorption energies in kcal/mol. This was aimed at mimicking the layer-by-layer electrode fabrication stages employed in this study.

GO/Reb A system	ΔG (Adsorption energy) kcal/mol
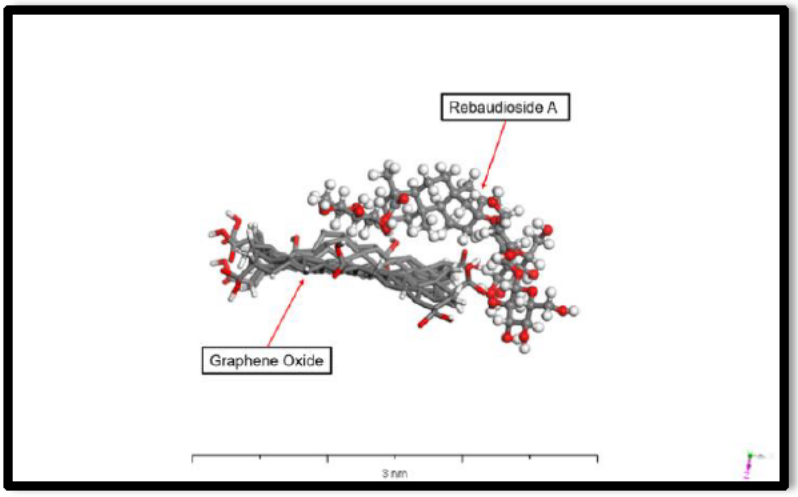	-47,940 kcal/mol

Figure 5-20: Representation of GO/Reb A system comprising of GO in stick model while Reb A is in the ball and stick model with calculated adsorption energy (ΔG) of -47,940 kcal/mol at 3 nm scale.

MWCNTs/GO system	ΔG (Adsorption energy) kcal/mol
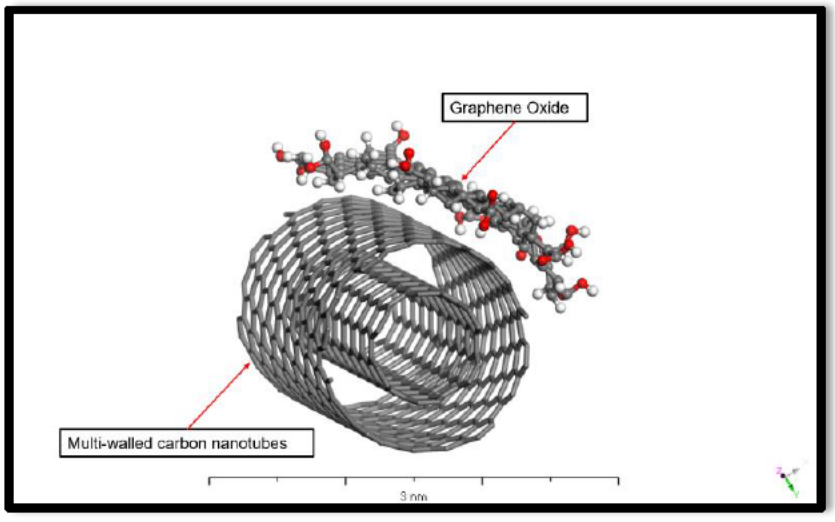	-170.447 kcal/mol

Figure 5-21: Representation of MWCNTs/GO system comprising of MWCNTs in stick model while GO is in the ball and stick model with calculated adsorption energy (ΔG) of -170.447 kcal at 3 nm scale.

ZnONPs/GO system	ΔG (Adsorption energy) kcal/mol
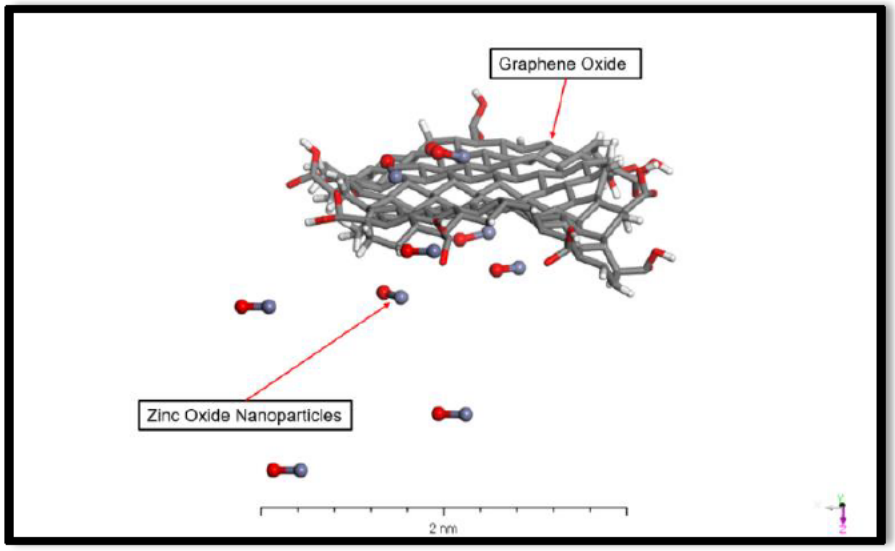	-13.852 kcal/mol

Figure 5-22: Representation of ZnONPs/GO system comprising of GO in stick model while ZnONPs is in the ball and stick model with calculated adsorption energy (ΔG) of -13.852 kcal/mol at 2 nm scale.

ZnONPs/GO/Reb A system	ΔG (Adsorption energy) kcal/mol
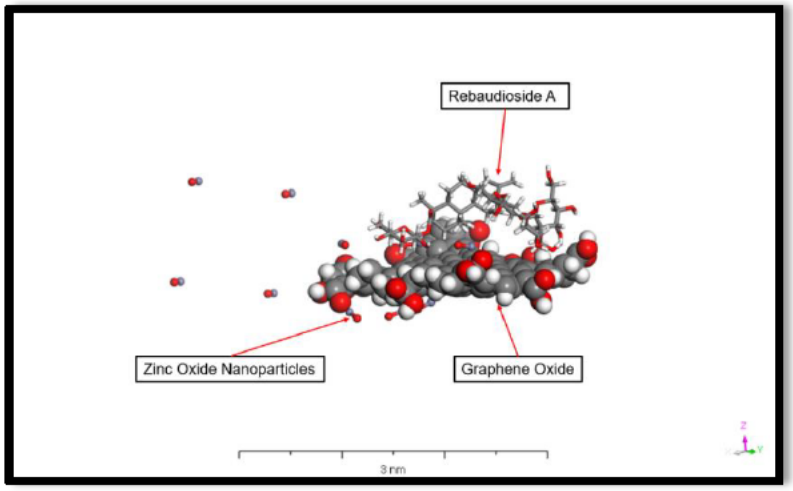	-44.568 kcal/mol

Figure 5-23: Computational modelling representation of ZnONPs/GO/Reb A system comprising of CPK model graphene oxide, ball and stick model ZnONPs and stick format Reb A. The adsorption energy of the system was calculated to be -44.568 kcal/mol.

ZnONPs/GO/MWCNTs/RebA system	ΔG (Adsorption energy) kcal/mol
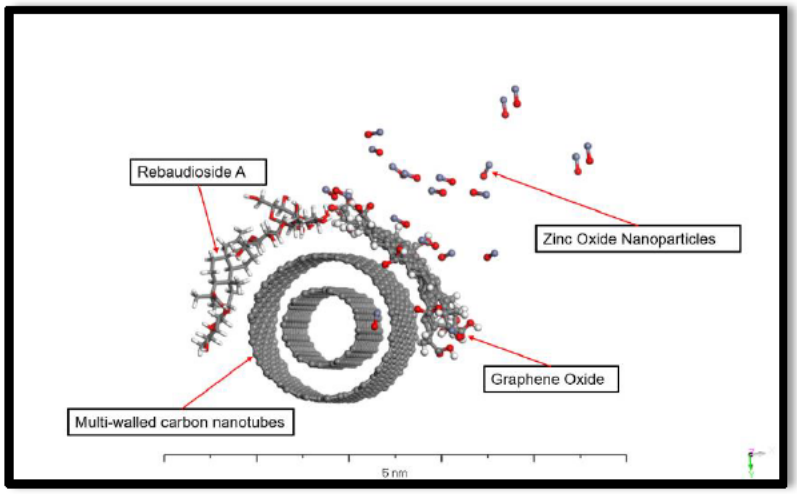	-63.539 kcal/mol

Figure 5-24: Computational modelling representation of ZnONPs/GO/MWCNTs/RebA system comprising of the ball and stick model GO, ball and stick model ZnONPs, ball and stick model MWCNTs and stick format Reb A. The adsorption energy of the system was calculated to be -63.539 kcal/mol.

ZnONPs/GO/T1R2/Reb A system	ΔG (Adsorption energy) kcal/mol
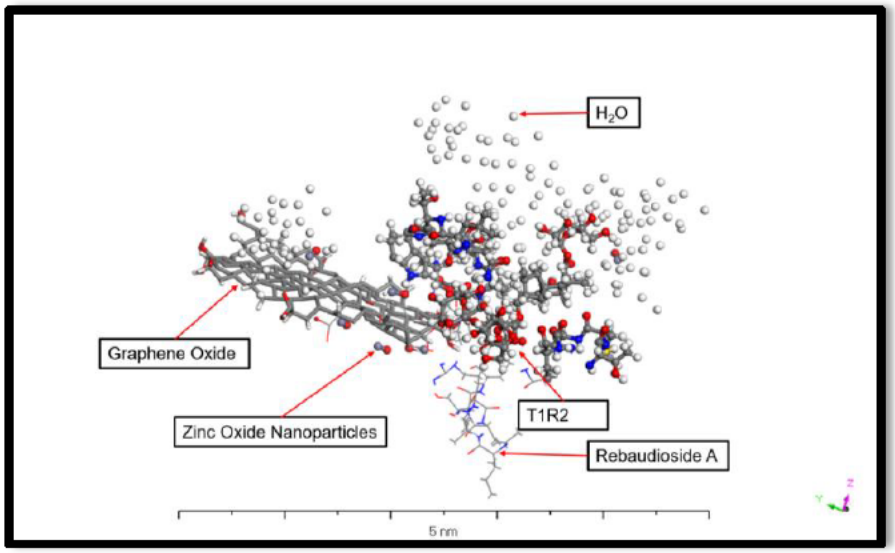	-38.3258 kcal/mol

Figure 5-25: Computational modelling representation of ZnONPs/GO/T1R2/Reb A system comprising of stick model GO, ball and stick model ZnONPs, ball and stick model T1R2 and line format Reb A. The system was solvated in water and adsorption energy was calculated to be -38.3258 kcal/mol.

ZnONPs/GO/MWCNTs/T1R2/Reb A	ΔG (Adsorption energy) kcal/mol
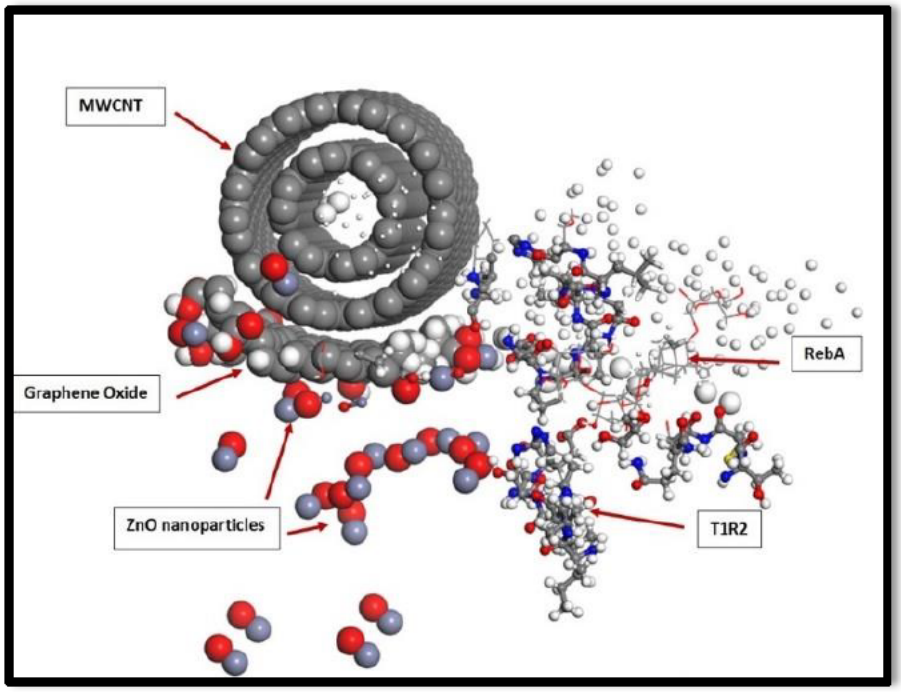	-44.286 kcal/mol

S

Figure 5-26: Computational modelling representation of ZnONPs/GO/MWCNTs/T1R2/Reb A system comprising of CPK model GO, ZnONPs and MWCNTs, ball and stick model T1R2 and line format Reb A. The system was solvated in water and adsorption energy was calculated to be -44.286 kcal/mol.

Experimentally, the similar trend was observed when electrochemically studying Reb A with different modifications at the surface of the Pt-E as previously presented in Figure 5.11. The aim of computational chemistry was to get deeper molecular level understanding of the immunosensor components and correlate these results to experimental findings.

CHAPTER 6: CONCLUSION AND RECOMMENDATIONS

This study presents insights into the development of a novel human sweet taste receptor nanocomposite modified electrochemical immunosensing device for the detection of Reb A. In Addition, the interaction between the biomolecules at the nanostructure interface were explored using computational methods.

The electrochemical immunosensor for detecting Reb A was successfully developed, using a step-by-step electrode fabrication strategy, followed by a series of characterization tools. The role played by the morphology and size characterization of nanoparticles in signal amplification was studied through HR-TEM, showing that the ZnONPs were evenly anchored around the walls of the MWCNTs. On the other hand, the hydrodynamic diameter obtained through asymmetric field flow fractionation (AF4) was slightly greater than that of ICP-MS, being 118 nm and 93 nm, respectively. This discrepancy is due mainly to the inherent theoretical principles involved in the respective techniques.

The electrochemical behaviour of the developed immunosensor was evaluated qualitatively and quantitatively, by employing cyclic and differential pulse voltammetry respectively. In this work, the GO/MWCNTs/T1R2/Pt was represented as sufficient tool for detecting Reb A, with the nanocomposite displaying adequate catalytic efficiency in contrast to the bare electrode. Under optimized conditions, the developed immunosensor had a linear range of detection from 0.1996 mg/L to 1.5748 mg/L and with a limit of detection of 0.6346 mg/L for Reb A.

This study also utilized molecular docking to better understand the ligand-protein interaction. For this purpose, the Reb A was docked against the rigid T1R2 human sweet taste receptor with a binding affinity of -8,7 kcal/mol and the free binding energy of -60.445 kcal/mol. The adsorption energies of the different modification stages were also deduced from density functional theory calculations.

The synergies between the experimental and computational methods employed in this study, can be attributed to a positive correlation of the results obtained for the electrochemical layer-by-layer electrode surface modification with the calculated

results obtained for the corresponding layer-by-layer adsorption energies employed for the electrode modification steps. An increase in the oxidation current of the Reb A in the presence of MWCNTs showed higher adsorption capabilities as opposed to the unmodified MWCNTs systems. A major finding of this study is the inclusion of MWCNTs showed a better adsorption energy (ΔG = -76.64 kcal/mol), in contrast to a nanocomposite in the absence of the MWCNT's (ΔG = -13.85 kcal/mol).

The results of this study may contribute to the development of an immunosensor that can potentially be used to quantify steviol glycosides in the food and beverage industry.

REFERENCES

Ahmad, M., Yingying, S., Nisar, A., Sun, H., Shen, W., Wei, M. and Zhu, J. 2011. Synthesis of hierarchical flower-like ZnO nanostructures and their functionalization by Au nanoparticles for improved photocatalytic and high performance Li-ion battery anodes. *Journal of Materials Chemistry*, 21 (21): 7723-7729.

Alarcón, S. H., Palleschi, G., Compagnone, D., Pascale, M., Visconti, A. and Barna-Vetró, I. 2006. Monoclonal antibody based electrochemical immunosensor for the determination of ochratoxin A in wheat. *Talanta*, 69 (4): 1031-1037.

Alves, T., Kolodziej, C., Burda, C. and Franco Jr, A. 2018. Effect of particle shape and size on the morphology and optical properties of zinc oxide synthesized by the polyol method. *Materials & Design*, 146: 125-133.

Atitar, M. F., Belhadj, H., Dillert, R. and Bahnemann, D. W. 2015. The relevance of ATR-FTIR spectroscopy in semiconductor photocatalysis. In: *Emerging Pollutants in the Environment-Current and Further Implications*. IntechOpen.

Ayyappa, B., Kanchi, S., Singh, P., Sabela, M. I., Dovey, M. and Bisetty, K. 2015. Analytical evaluation of steviol glycosides by capillary electrophoresis supported with molecular docking studies. *Journal of the Iranian Chemical Society*, 12 (1): 127-136.

Bakeev, K. A. 2010. *Process analytical technology: spectroscopic tools and implementation strategies for the chemical and pharmaceutical industries*. John Wiley & Sons.

Balgobind, K., Kanchi, S., Sharma, D., Bisetty, K. and Sabela, M. I. 2016. Hybrid of ZnONPs/MWCNTs for electrochemical detection of aspartame in food and beverage samples. *Journal of Electroanalytical Chemistry*, 774: 51-57.

Bathinapatla, A., Kanchi, S., Singh, P., Sabela, M. I. and Bisetty, K. 2016. An ultrasensitive performance enhanced novel cytochrome c biosensor for the detection of rebaudioside A. *Biosensors and Bioelectronics*, 77: 116-123.

Becheri, A., Dürr, M., Nostro, P. L. and Baglioni, P. 2008. Synthesis and characterization of zinc oxide nanoparticles: application to textiles as UV-absorbers. *Journal of Nanoparticle Research*, 10 (4): 679-689.

Beitollahi, H., Ivari, S. G. and Torkzadeh-Mahani, M. 2018. Application of antibody–nanogold–ionic liquid–carbon paste electrode for sensitive electrochemical immunoassay of thyroid-stimulating hormone. *Biosensors and Bioelectronics*, 110: 97-102.

Berendsen, H. J. C., Postma, J. P. M., Vangunsteren, W. F., Dinola, A. and Haak, J. R. 1984. Molecular-dynamics with coupling to an external bath. *Journal of Chemical Physics*, 81 (8): 3684-3690.

Bergs, D., Burghoff, B., Joehnck, M., Martin, G. and Schembecker, G. 2012. Fast and isocratic HPLC-method for steviol glycosides analysis from Stevia rebaudiana leaves. *Journal für Verbraucherschutz und Lebensmittelsicherheit*, 7 (2): 147-154.

Borisov, S. M. and Wolfbeis, O. S. 2008. Optical biosensors. *Chemical reviews*, 108 (2): 423-461.

Bunte, S. W. and Sun, H. 2000. Molecular modeling of energetic materials: the parameterization and validation of nitrate esters in the COMPASS force field. *The Journal of Physical Chemistry B*, 104 (11): 2477-2489.

Carakostas, M., Curry, L., Boileau, A. and Brusick, D. 2008. Overview: the history, technical function and safety of rebaudioside A, a naturally occurring steviol glycoside, for use in food and beverages. *Food and Chemical Toxicology*, 46 (7): S1-S10.

Case, D. A., Cheatham, T. E., Darden, T., Gohlke, H., Luo, R., Merz, K. M., Onufriev, A., Simmerling, C., Wang, B. and Woods, R. J. 2005. The amber biomolecular simulation programs. *Journal of Computational Chemistry*, 26 (16): 1668-1688.

Casewit, C., Colwell, K. and Rappe, A. 1992. Application of a universal force field to organic molecules. *Journal of the American chemical society*, 114 (25): 10035-10046.

Chang, C.-S. and Yeh, T. S. 2014. Detection of 10 sweeteners in various foods by liquid chromatography/tandem mass spectrometry. *journal of food and drug analysis*, 22 (3): 318-328.

Charsley, E., Price, D., Hunter, N., Gabbott, P., Kett, V., Gaisford, S., Priestley, I., Duncan, J., Royall, P. and Scowen, I. 2019. *Principles of thermal analysis and calorimetry*. Royal society of chemistry.

Cheemalapati, S., Palanisamy, S., Mani, V. and Chen, S.-M. 2013. Simultaneous electrochemical determination of dopamine and paracetamol on multiwalled carbon nanotubes/graphene oxide nanocomposite-modified glassy carbon electrode. *Sensors and Actuators B: Chemical*, 117: 297-304.

Cornell, W. D., Cieplak, P., Bayly, C. I., Gould, I. R., Merz, K. M., Ferguson, D. M., Spellmeyer, D. C., Fox, T., Caldwell, J. W. and Kollman, P. A. 1996. A second generation force field for the simulation of proteins, nucleic acids, and organic molecules (vol 117, pg 5179, 1995). *Journal of the American Chemical Society*, 118 (9): 2309-2309.

Cornell, W. D., Cieplak, P., Bayly, C. I., Gould, I. R., Merz, K. M., Ferguson, D. M., Spellmeyer, D. C., Fox, T., Caldwell, J. W., and Kollman, P. A. 1995. A 2nd generation force-field for the simulation of proteins, nucleic-acids, and organic-molecules. *Journal of the American Chemical Society*, 117 (19): 5179-5197.

Donovan, A. R., Adams, C. D., Ma, Y., Stephan, C., Eichholz, T. and Shi, H. 2016. Detection of zinc oxide and cerium dioxide nanoparticles during drinking water treatment by rapid single particle ICP-MS methods. *Analytical and bioanalytical chemistry*, 408 (19): 5137-5145.

Duan, Y., Wu, C., Chowdhury, S., Lee, M. C., Xiong, G. M., Zhang, W., Yang, R., Cieplak, P., Luo, R., Lee, T., Caldwell, J., Wang, J. M. and Kollman, P. A. 2003. point-charge force field for molecular mechanics simulations of proteins based on condensed-phase quantum mechanical calculations. *Journal of Computational Chemistry*, 24: 1999–2012.

Dubascoux, S., Le Hecho, I., Hassellöv, M., Von Der Kammer, F., Gautier, M. P. and Lespes, G. 2010. Field-flow fractionation and inductively coupled plasma mass spectrometer coupling:

History, development and applications. *Journal of Analytical Atomic Spectrometry*, 25 (5): 613-623.

Erkucuk, A., Akgun, I. and Yesil-Celiktas, O. 2009. Supercritical CO2 extraction of glycosides from Stevia rebaudiana leaves: Identification and optimization. *The Journal of Supercritical Fluids*, 51 (1): 29-35.

Felix, F., Baccaro, A. and Angnes, L. 2018. Disposable Voltammetric Immunosensors Integrated with Microfluidic Platforms for Biomedical, Agricultural and Food Analyses: A Review. *Sensors*, 18 (12): 4124.

Frick, J. M., Ambrosi, A., Pollo, L. D. and Tessaro, I. C. 2018. Influence of Glutaraldehyde Crosslinking and Alkaline Post-treatment on the Properties of Chitosan-Based Films. *Journal of Polymers and the Environment*: 1-10.

Frisch MJ, T. G., Schlegel HB, Scuseria GE, Robb MA,, Cheeseman JR, M. J., Vreven T, Kudin KN, Burant, JC, M. J., Iyengar SS, Tomasi J, Barone V, Mennucci B,Cossi M, Scalmani G, Rega N, Petersson GA, Nakatsuji H, Hada, M, E. M., Toyota K, Fukuda R, Hasegawa J, Ishida M,, Nakajima T, H. Y., Kitao O, Nakai H, Klene M, Li X, Knox, JE, H. H., Cross JB, Bakken V, Adamo C, Jaramillo J,, Gomperts R, S. R., Yazyev O, Austin AJ, Cammi R,, Pomelli C, O. J., Ayala PY, Morokuma K, Voth GA,, Salvador P, D. J., Zakrzewski VG, Dapprich S, Daniels, AD, S. M., Farkas O, Malick DK, Rabuck AD, Raghavachari, K, F. J., Ortiz JV, Cui Q, Baboul AG, Clifford S,, Cioslowski J, S. B., Liu G, Liashenko A, Piskorz P,, Komaromi I, M. R., Fox DJ, Keith T, Al-Laham MA, Peng, CY, N. A., Challacombe M, Gill PMW, Johnson B, and Chen W, W. M., Gonzalez C, Pople JA. 2004. http://www.gaussian.com/g_misc/g03/citation_g03.htm. *Gaussian Inc, Wallingford, CT*,

Gaisford, S., Kett, V. and Haines, P. 2016. *Principles of thermal analysis and calorimetry*. Royal society of chemistry.

Gardana, C., Scaglianti, M. and Simonetti, P. 2010. Evaluation of steviol and its glycosides in Stevia rebaudiana leaves and commercial sweetener by ultra-high-performance liquid chromatography-mass spectrometry. *Journal of Chromatography A*, 1217 (9): 1463-1470.

Gnanasangeetha, D. and SaralaThambavani, D. 2013. One pot synthesis of zinc oxide nanoparticles via chemical and green method. *Res J Mater Sci*, 2320: 6055.

Guex, N. and Peitsch, M. C. 1997. SWISS-MODEL and the Swiss-Pdb Viewer: an environment for comparative protein modeling. *Electrophoresis*, 18 (15): 2714-2723.

Habtamu, H. B., Sentic, M., Silvestrini, M., De Leo, L., Not, T., Arbault, S., Manojlovic, D., Sojic, N. and Ugo, P. 2015. A sensitive electrochemiluminescence immunosensor for celiac disease diagnosis based on nanoelectrode ensembles. *Analytical chemistry*, 87 (24): 12080-12087.

Hearn, L. and Subedi, P. 2009. Determining levels of steviol glycosides in the leaves of Stevia rebaudiana by near infrared reflectance spectroscopy. *Journal of Food Composition and Analysis*, 22 (2): 165-168.

Hou, S.-l., Ma, Z.-e., Meng, H., Xu, Y. and He, Q.-h. 2019. Ultrasensitive and green electrochemical immunosensor for mycotoxin ochratoxin A based on phage displayed mimotope peptide. *Talanta*, 194: 919-924.

Huang, Y., Lu, D., Liu, H., Liu, S., Jiang, S., Pang, G.-c. and Liu, Y. 2019. Preliminary research on the receptor–ligand recognition mechanism of umami by an hT1R1 biosensor. *Food & function*, 10 (3): 1280-1287.

Humphrey, W., Dalke, A. and Schulten, K. 1996. VMD: Visual molecular dynamics. *Journal of Molecular Graphics*, 14 (1): 33-38.

Jackson, A. U., Tata, A., Wu, C., Perry, R. H., Haas, G., West, L. and Cooks, R. G. 2009. Direct analysis of Stevia leaves for diterpene glycosides by desorption electrospray ionization mass spectrometry. *Analyst*, 134 (5): 867-874.

Jadhao, D., Katekhaye, S. and Thorat, B. 2011. Improved RP-HPLC method for quantitative estimation of stevioside in Stevia rebaudiana Bertoni Burm. *Int. J. Phyto. Pharm*, 1: 27-34.

Jain, A., Shin, Y. and Persson, K. A. 2016. Computational predictions of energy materials using density functional theory. *Nature Reviews Materials*, 1 (1): 15004.

Jaitak, V. 2015. Interaction model of steviol glycosides from Stevia rebaudiana (Bertoni) with sweet taste receptors: A computational approach. *Phytochemistry*, 116: 12-20.

Jaitak, V., Bandna, B. S. and Kaul, V. K. 2009. An efficient microwave-assisted extraction process of stevioside and rebaudioside-A from Stevia rebaudiana (Bertoni). *Phytochemical Analysis*, 20 (3): 240-245.

Jakalian, A., Bush, B. L., Jack, D. B. and Bayly, C. I. 2000. Fast, efficient generation of high-quality atomic Charges. AM1-BCC model: I. Method. *Journal of Computational Chemistry*, 21 (2): 132-146.

Javed, R., Usman, M., Yücesan, B., Zia, M. and Gürel, E. 2017. Effect of zinc oxide (ZnO) nanoparticles on physiology and steviol glycosides production in micropropagated shoots of Stevia rebaudiana Bertoni. *Plant Physiology and Biochemistry*, 110: 94-99.

Jayakrishnan, D. S. 2012. Electrodeposition: the versatile technique for nanomaterials. In: *Corrosion Protection and Control Using Nanomaterials*. Elsevier, 86-125.

Jorgensen, W. L., Chandrasekhar, J., Madura, J. D., Impey, R. W. and Klein, M. L. 1983. Comparison of simple potential functions for simulating liquid water. *Journal of Chemical Physics*, 79 (2): 926-935.

Kakigi, Y., Suzuki, T., Icho, T., Uyama, A. and Mochizuki, N. 2013. Classification of stevia sweeteners in soft drinks using liquid chromatography and time-of-flight mass spectrometry. *Food Additives & Contaminants: Part A*, 30 (12): 2043-2049.

Kalkhof, S. and Sinz, A. 2008. Chances and pitfalls of chemical cross-linking with amine-reactive N-hydroxysuccinimide esters. *Analytical and bioanalytical chemistry*, 392 (1-2): 305-312.

Karimi-Maleh, H., Ahanjan, K., Taghavi, M. and Ghaemy, M. 2016. A novel voltammetric sensor employing zinc oxide nanoparticles and a new ferrocene-derivative modified carbon

paste electrode for determination of captopril in drug samples. *Analytical Methods*, 8 (8): 1780-1788.

Karplus, M. and McCammon, J. A. 2002. Molecular dynamics simulations of biomolecules. *Nature Structural & Molecular Biology*, 9 (9): 646.

Kaufman, B. A., Newman, S. M., Hallberg, R. L., Slaughter, C. A., Perlman, P. S. and Butow, R. A. 2000. In organello formaldehyde crosslinking of proteins to mtDNA: identification of bifunctional proteins. *Proceedings of the National Academy of Sciences*, 97 (14): 7772-7777.

Kaur, B., Pandiyan, T., Satpati, B. and Srivastava, R. 2013. Simultaneous and sensitive determination of ascorbic acid, dopamine, uric acid, and tryptophan with silver nanoparticles-decorated reduced graphene oxide modified electrode. *Colloids and Surfaces B: Biointerfaces*, 111: 97-106.

Kedik, S., Fedorov, S., Yanul', N., Prokhorova, L., Smirnova, E. and Panov, A. 2003. Chromatographic determination of stevioside in raw plant material. *Pharmaceutical Chemistry Journal*, 37 (10): 529-532.

King, D. M., Liang, X., Carney, C. S., Hakim, L. F., Li, P. and Weimer, A. W. 2008. Atomic layer deposition of UV-absorbing ZnO films on SiO2 and TiO2 nanoparticles using a fluidized bed reactor. *Advanced functional materials*, 18 (4): 607-615.

Kolb, N., Herrera, J., Ferreyra, D. and Uliana, R. 2001. Analysis of sweet diterpene glycosides from Stevia rebaudiana: improved HPLC method. *Journal of Agricultural and Food Chemistry*, 49 (10): 4538-4541.

Kroger, M., Meister, K. and Kava, R. 2006. Low-calorie sweeteners and other sugar substitutes: a review of the safety issues. *Comprehensive reviews in food science and food safety*, 5 (2): 35-47.

Kumar, H., Kaul, K., Bajpai-Gupta, S., Kaul, V. K. and Kumar, S. 2012. A comprehensive analysis of fifteen genes of steviol glycosides biosynthesis pathway in Stevia rebaudiana (Bertoni). *Gene*, 492 (1): 276-284.

Kumar, S., Song, T., Gautam, S., Chae, K., Kim, S. and Jang, K. 2015. Structural, magnetic and electronic structure properties of Co doped ZnO nanoparticles. *Materials Research Bulletin*, 66: 76-82.

Kwon, S. J., Kim, E., Yang, H. and Kwak, J. 2006. An electrochemical immunosensor using ferrocenyl-tethered dendrimer. *Analyst*, 131 (3): 402-406.

Laber, C. H., Essner, J. B., Scott, T. A., Polo-Parada, L. and Baker, G. A. 2016. Domestic pressure cooker as inexpensive hydrothermal vessel: Demonstrated utility for eco-friendly synthesis of non-toxic carbon dots. *Nano-Structures & Nano-Objects*, 6: 52-58.

Li, J., Chen, Z. and Di, D. 2012. Preparative separation and purification of Rebaudioside A from Stevia rebaudiana Bertoni crude extracts by mixed bed of macroporous adsorption resins. *Food chemistry*, 132 (1): 268-276.

Li, L., Xu, J., Zheng, X., Ma, C., Song, X., Ge, S., Yu, J. and Yan, M. 2014. Growth of gold-manganese oxide nanostructures on a 3D origami device for glucose-oxidase label based electrochemical immunosensor. *Biosensors and Bioelectronics*, 61: 76-82.

Liang, T., Fu, Q., Shen, A., Wang, H., Jin, Y., Xin, H., Ke, Y., Guo, Z. and Liang, X. 2015. Preparation and chromatographic evaluation of a newly designed steviol glycoside modified-silica stationary phase in hydrophilic interaction liquid chromatography and reversed phase liquid chromatography. *Journal of Chromatography A*, 1388: 110-118.

Lim, S. A. and Ahmed, M. U. 2016. Electrochemical immunosensors and their recent nanomaterial-based signal amplification strategies: a review. *RSC Advances*, 6 (30): 24995-25014.

Liu, Y., Cai, Z., Sheng, L., Ma, M., Xu, Q. and Jin, Y. 2019. Structure-property of crosslinked chitosan/silica composite films modified by genipin and glutaraldehyde under alkaline conditions. *Carbohydrate polymers*, 215: 348-357.

Lorenzo, C., Serrano-Díaz, J., Plaza, M., Quintanilla, C. and Alonso, G. L. 2014. Fast methodology of analysing major steviol glycosides from Stevia rebaudiana leaves. *Food chemistry*, 157: 518-523.

Mauri, P., Catalano, G., Gardana, C. and Pietta, P. 1996. Analysis of stevia glycosides by capillary electrophoresis. *Electrophoresis*, 17 (2): 367-371.

Mayank and Jaitak, V. 2015. Interaction model of steviol glycosides from Stevia rebaudiana (Bertoni) with sweet taste receptors: A computational approach. *Phytochemistry*, 116: 12-20.

Mayo, S. L., Olafson, B. D. and Goddard, W. A. 1990. DREIDING: a generic force field for molecular simulations. *Journal of Physical chemistry*, 94 (26): 8897-8909.

Midson, S., Korenyi-Both, A. and Clarke, K. 2017. Lubricious thin-film coatings for forging applications: a literature review.

Migneault, I., Dartiguenave, C., Bertrand, M. J. and Waldron, K. C. 2004. Glutaraldehyde: behavior in aqueous solution, reaction with proteins, and application to enzyme crosslinking. *Biotechniques*, 37 (5): 790-802.

Moina, C. and Ybarra, G. 2012. Fundamentals and applications of immunosensors. In: *Advances in immunoassay technology*. IntechOpen.

Montaño, M. D., Olesik, J. W., Barber, A. G., Challis, K. and Ranville, J. F. 2016. Single Particle ICP-MS: Advances toward routine analysis of nanomaterials. *Analytical and bioanalytical chemistry*, 408 (19): 5053-5074.

Morris, G. M., Goodsell, D. S., Halliday, R. S., Huey, R., Hart, W. E., Belew, R. K. and Olson, A. J. 1998. Automated docking using a lamarckian genetic algorithm and an empirical binding free energy function. *Journal of Computational Chemistry*, 19 (14): 1639-1662.

Morris, G. M., Huey, R., Lindstrom, W., Sanner, M. F., Belew, R. K., Goodsell, D. S. and Olson, A. J. 2009. AutoDock4 and AutoDockTools4: Automated docking with selective receptor flexibility. *J Comput Chem*, 30 (16): 2785-2791.

National Center for Biotechnology Information. 2019. *PubChem Database*.

Nerenberg, P. S. and Head-Gordon, T. 2018. New developments in force fields for biomolecular simulations. *Current opinion in structural biology*, 49: 129-138.

Nochaiya, T., Sekine, Y., Choopun, S. and Chaipanich, A. 2015. Microstructure, characterizations, functionality and compressive strength of cement-based materials using zinc oxide nanoparticles as an additive. *Journal of Alloys and Compounds*, 630: 1-10.

Ouimet, C. M., Dawod, M., Grinias, J., Assimon, V. A., Lodge, J., Mapp, A. K., Gestwicki, J. E. and Kennedy, R. T. 2018. Protein cross-linking capillary electrophoresis at increased throughput for a range of protein–protein interactions. *Analyst*, 143 (8): 1805-1812.

Pagadala, N. S., Syed, K. and Tuszynski, J. 2017. Software for molecular docking: a review. *Biophysical reviews*, 9 (2): 91-102.

Pavlíček, V. and Tůma, P. 2017. The use of capillary electrophoresis with contactless conductivity detection for sensitive determination of stevioside and rebaudioside A in foods and beverages. *Food chemistry*, 219: 193-198.

Poda, A., Bednar, A., Kennedy, A., Harmon, A., Hull, M., Mitrano, D., Ranville, J. and Steevens, J. 2011. Characterization of silver nanoparticles using flow-field flow fractionation interfaced to inductively coupled plasma mass spectrometry. *Journal of Chromatography A*, 1218 (27): 4219-4225.

Polarz, S., Roy, A., Merz, M., Halm, S., Schröder, D., Schneider, L., Bacher, G., Kruis, F. E. and Driess, M. 2005. Chemical vapor synthesis of size-selected zinc oxide nanoparticles. *Small*, 1 (5): 540-552.

Pourmortazavi, S. M., Marashianpour, Z., Karimi, M. S. and Mohammad-Zadeh, M. 2015. Electrochemical synthesis and characterization of zinc carbonate and zinc oxide nanoparticles. *Journal of Molecular Structure*, 1099: 232-238.

Prakash, I., Upreti, M., Dubois, G. E., King, G. A. and Mehta, A. 2015. *Rebaudioside a composition and method for purifying rebaudioside a*: Google Patents.

Pundir, C. and Malik, A. 2019. Bio-sensing of organophosphorus pesticides: A review. *Biosensors and Bioelectronics*: 111348.

Rajasekaran, T., Ramakrishna, A., Udaya Sankar, K., Giridhar, P. and Ravishankar, G. 2008. Analysis of predominant steviosides in Stevia rebaudiana Bertoni by liquid chromatography/electrospray ionization-mass spectrometry. *Food Biotechnology*, 22 (2): 179-188.

Ramanathan, M., Porter, D. F. and Khavari, P. A. 2019. Methods to study RNA–protein interactions. *Nature methods*, 16 (3): 225-234.

Rappe, A., Colwell, K. and Casewit, C. 1993. Application of a universal force field to metal complexes. *Inorganic Chemistry*, 32 (16): 3438-3450.

Ricci, F., Volpe, G., Micheli, L. and Palleschi, G. 2007. A review on novel developments and applications of immunosensors in food analysis. *Analytica chimica acta*, 605 (2): 111-129.

Ryckaert, J. P., Ciccotti, G. and Berendsen, H. J. C. 1977. Numerical-integration of cartesian equations of motion of a system with constraints - molecular-dynamics of n-alkanes. *Journal of Computational Physics*, 23 (3): 327-341.

Saleh, S. M., Soliman, A. M., Sharaf, M. A., Kale, V. and Gadgil, B. 2017. Influence of solvent in the synthesis of nano-structured ZnO by hydrothermal method and their application in solar-still. *Journal of Environmental Chemical Engineering*, 5 (1): 1219-1226.

Samah, N., Hisham, A. and Rahim, S. 2013. Determination of stevioside and rebaudioside A in Stevia rebaudiana leaves via preparative high performance liquid chromatography (prep-HPLC). *International Journal*, 4 (2)

Samanta, P. 2017. Review on wet chemical growth and anti-bacterial activity of zinc oxide nanostructures. *J Tissue Sci Eng*, 8 (197): 2.

Saravanakkumar, D., Sivaranjani, S., Kaviyarasu, K., Ayeshamariam, A., Ravikumar, B., Pandiarajan, S., Veeralakshmi, C., Jayachandran, M. and Maaza, M. 2018. Synthesis and characterization of ZnO–CuO nanocomposites powder by modified perfume spray pyrolysis method and its antimicrobial investigation. *Journal of Semiconductors*, 39 (3): 033001.

Shafii, B., Vismeh, R., Beaudry, R., Warner, R. and Jones, A. D. 2012. Large-scale profiling of diterpenoid glycosides from Stevia rebaudiana using ultrahigh performance liquid chromatography/tandem mass spectrometry. *Analytical and bioanalytical chemistry*, 403 (9): 2683-2690.

Shah, R., De Jager, L. S. and Begley, T. H. 2012. Simultaneous determination of steviol and steviol glycosides by liquid chromatography-mass spectrometry. *Food Additives & Contaminants: Part A*, 29 (12): 1861-1871.

Sharma, D., Sabela, M. I., Kanchi, S., Bisetty, K., Skelton, A. A. and Honarparvar, B. 2018. Green synthesis, characterization and electrochemical sensing of silymarin by ZnO nanoparticles: experimental and DFT studies. *Journal of Electroanalytical Chemistry*, 808: 160-172.

Sirelkhatim, A., Mahmud, S., Seeni, A., Kaus, N. H. M., Ann, L. C., Bakhori, S. K. M., Hasan, H. and Mohamad, D. 2015. Review on Zinc Oxide Nanoparticles: Antibacterial Activity and Toxicity Mechanism. *Nano-Micro Letters*, 7 (3): 219-242.

Skoog, D. A., Holler, F. J. and Crouch, S. R. 2017. *Principles of instrumental analysis*. Cengage learning.

Skoog, D. A., West, D. M., Holler, F. J. and Crouch, S. 2013. *Fundamentals of analytical chemistry*. Nelson Education.

Sogne, V., Meier, F., Klein, T. and Contado, C. 2017. Investigation of zinc oxide particles in cosmetic products by means of centrifugal and asymmetrical flow field-flow fractionation. *Journal of Chromatography A*, 1515: 196-208.

Song, X., Liu, Y., Zheng, Y., Ding, K., Nie, S. and Yang, P. 2016. Synthesis of butterfly-like ZnO nanostructures and study of their self-reducing ability toward Au 3+ ions for enhanced photocatalytic efficiency. *Physical Chemistry Chemical Physics*, 18 (6): 4577-4584.

Sun, H. 1998. COMPASS: An ab Initio Force-Field Optimized for Condensed-Phase ApplicationsOverview with Details on Alkane and Benzene Compounds. *The Journal of Physical Chemistry B*, 102 (38): 7338-7364.

Sun, H., Ren, P. and Fried, J. 1998. The COMPASS force field: parameterization and validation for phosphazenes. *Computational and Theoretical Polymer Science*, 8 (1-2): 229-246.

Trott, O. and Olson, A. J. 2010. AutoDock Vina: Improving the speed and accuracy of docking with a new scoring function, efficient optimization and multithreading. *Journal of Computational Chemistry*, 31 (2): 455-461.

Ulicny, J. and Kozar, T. 2018. Roadmap for Computer-Aided Modeling of Theranostics and Related Nanosystems. In: Proceedings of *EPJ Web of Conferences*. EDP Sciences, 05017.

Vafaee, M. and Ghamsari, M. S. 2007. Preparation and characterization of ZnO nanoparticles by a novel sol–gel route. *Materials Letters*, 61 (14-15): 3265-3268.

Velasco-Lozano, S., López-Gallego, F., Mateos-Díaz, J. C. and Favela-Torres, E. 2016. Cross-linked enzyme aggregates (CLEA) in enzyme improvement–a review. *Biocatalysis*, 1 (1): 166-177.

Wang, J., Wolf, R. M., Caldwell, J. W., Kollman, P. A. and Case, D. A. 2004a. Development and testing of a general amber force field. *Journal of computational chemistry*, 25 (9): 1157-1174.

Wang, J. M., Wolf, R. M., Caldwell, J. W., Kollman, P. A. and Case, D. A. 2004b. Development and testing of a general amber force field. *Journal of Computational Chemistry*, 25 (9): 1157-1174.

Wingard, R. E., Brown, J. P., Enderlin, F. E., Dale, J. A., Hale, R. L. and Seitz, C. T. 1980. Intestinal degradation and absorption of the glycosidic sweeteners stevioside and rebaudioside A. *Experientia*, 36 (5): 519-520.

Woelwer-Rieck, U., Lankes, C., Wawrzun, A. and Wüst, M. 2010. Improved HPLC method for the evaluation of the major steviol glycosides in leaves of Stevia rebaudiana. *European Food Research and Technology*, 231 (4): 581-588.

Xie, Z.-R. and Hwang, M.-J. 2015. Methods for Predicting Protein–Ligand Binding Sites. In: *Molecular modeling of proteins*. Springer, 383-398.

Yadav, A., Prasad, V., Kathe, A., Raj, S., Yadav, D., Sundaramoorthy, C. and Vigneshwaran, N. 2006. Functional finishing in cotton fabrics using zinc oxide nanoparticles. *Bulletin of Materials Science*, 29 (6): 641-645.

Yang, D.-j. and Chen, B. 2009. Simultaneous Determination of Nonnutritive Sweeteners in Foods by HPLC/ESI-MS. *Journal of Agricultural and Food Chemistry*, 57 (8): 3022-3027.

Yu, L., Zhang, Y., Hu, C., Wu, H., Yang, Y., Huang, C. and Jia, N. 2015. Highly sensitive electrochemical impedance spectroscopy immunosensor for the detection of AFB1 in olive oil. *Food chemistry*, 176: 22-26.

Zak, A. K., Majid, W. A., Darroudi, M. and Yousefi, R. 2011. Synthesis and characterization of ZnO nanoparticles prepared in gelatin media. *Materials Letters*, 65 (1): 70-73.

Zawadzka, A., Płóciennik, P., El Kouari, Y., Bougharraf, H. and Sahraoui, B. 2016. Linear and nonlinear optical properties of ZnO thin films deposited by pulsed laser deposition. *Journal of Luminescence,* 169: 483-491.

Zygler, A., Wasik, A. and Namieśnik, J. 2009. Analytical methodologies for determination of artificial sweeteners in foodstuffs. *TrAC Trends in Analytical Chemistry*, 28 (9): 1082-1102.

APPENDIX A :TABLE : ANALYTICAL PROCEDURES FOR SIMULTANEOUS DETERMINATION OF REBAUDIOSIDE A IN SAMPLES OF DIFFERENT FOOD PRODUCTS

Analyte	Sample	Technique	Mobile Phase/Electrolyte	Column/Capillary/ Electrode/Detector/Nanocomposite	[Analyte]	Ref.
Rebaudioside A	Different food samples	Electrochemical biosensor y	pH 11.0 in a 0.1 M borate buffer	Cytochrome c/AuNPs-GO/MWCNTs nanocomposite	The biosensor exhibited a 10-fold enhancement of the signal with Limit of detection (LOD) ranging from 0.001-0.05 mM	(Bathinapatla *et al.* 2016)
Rebaudioside A and Stevioside	Real stevia samples	Capillary Electrophoresis (CE)	1 M and 0.1 M Sodium Hydroxide, phosphate buffer and deionized water	30-mM heptakis-(2,3,6-tri-o-methyl beta-cyclodextrin) as a separating agent, fused silica capillary with 50 lm inner diameter and 363 lm outer diameter, and a diode array detector (DAD) at	$LOD_{Reb\ A}$= 2.017×10^{-5} M LOD_{Stv}= 7.386×10^{-5} M	(Ayyappa *et al.* 2015)

Rebaudioside A and Steviolbioside	*Stevia rebaudiana* leaves	Capillary electrophoresis (CE), High-performance liquid chromatography, Mass spectrometry.	20 mM sodium tetraborate buffer, pH 8.3, and 30 mM sodium dodecyl sulphate.	The fused-silica capillary was 56 cm (50 cm to the detector) X 50 pm ID, equipped with a 3D extended light path (bubble cell) from Hewlett-Packard, equipped with diode array detector (DAD)	Under these conditions, the detector response for each glycoside was linear over the range 0.2-5 mg/mL (0.4-20 ng injected)	(Mauri *et al.* 1996)
Stevioside	*Rebaudiana* Plant	Reversed-phase HPLC	Methanol and 0.1% orthophosphoric acid (v/v) (70:30)	Model G1316A thermostat column and UV array detector	LOD=0.02µg/mL LOQ=0.05µg/mL	(Jadhao *et al.* 2011)
Stevioside and Rebaudioside A	*Stevia Rebaudiana* leaves	Soxhlet extraction method via HPLC.	Acetonitrile: water (80 :20, v/v)	Waters XBridge C18 column ((150 mm x 4.6 mm I.D., 5µm), UV detector range, 205-215 nm.	This was a qualitative study, Retention times of 4.23 and 4.28 min for Stv and Reb A respectively.	(Samah *et al.* 2013)
Rebaudioside A	*Stevia rebaudiana* leaves	Isocratic HPLC	Water/Acetonitrile (65: 35, v/v)	PurospherÒ STAR RP-18 endcapped 3 lm HibarÒ RT 250-4.6 column at 50 °C, UV spectrophotometer detector at 210 nm.	LOD =0.0004 mg /mL LOQ =0.0038 mg/mL.	(Bergs *et al.* 2012)

Stevioside and rebaudioside A	Dried leaves of *Stevia rebaudiana*	Solvent extraction followed by HPLC	Acetonitrile/water (80:20, v/v)	NH_2 column (250 × 4.6 mm), UV detection in 210 nm	3.78 and 9.75% content of Stevioside, and 1.62 and 7.27% content of Rebaudioside A (weight)	(Kolb *et al.* 2001)
Stevioside and rebaudioside A	*Stevia* plants	Water extraction, solid phase extraction reversed-phase HPLC	[a] [Acetonitrile/ water (85:15 v/v)] [b] [Acetonitrile/water (75:25 v/v)]	[a] [Luna HILIC (250 9 4.6 mm) column] [b] [Luna NH2 100 A column (250 9 4.6 mm)]	The concentration for Stv and Reb A were 7.90 g ± 0.29 and 4.93 g ± 0.44 per 100 g	(Woelwer-Rieck *et al.* 2010)
Stevioside and rebaudioside A	*Stevia rebaudiana* leaves	Super critical fluid extraction HPLC	Water/Acetonitrile (20: 80)	Cosmosil® 5NH2-MS column (4.6mm×150mm), UV detector	LOD_{Stv} = 1.19 µg/mL LOQ_{Stv} = 3.98 µg/mL $LOD_{Reb\ A}$ = 1.98 µg/mL $LOQ_{Reb\ A}$ = 3.98 µg/mL	(Erkucuk *et al.* 2009)
Stevioside	Food beverages	Liquid chromatography/tandem mass chromatography (LC-MS/MS)	Gradient elution of 10 mM ammonium acetate in water and 10 mM ammonium acetate in methanol	Phenomenex Luna PhenylHexyl (5 mm, 4.6 mm × 150 mm) column, AB SCIEX QTRAP 4000 triple quadrupole tandem mass spectrometer.	LOQ_{Stv} = 0.1 µg/kg	(Chang and Yeh 2014)

Rebaudioside A	Soft drinks	LC and time-of-flight MS (LC-TOF-MS)	Gradient elution of formic acid in the water and solvent B was acetonitrile.	Asahipak NH2P-50 2D column (150 × 2.1 mm inner diameter), Triple TOF 5600 system (AB Sciex, Framingham, MA, USA)	This was a qualitative characterization study of several SGs in soft drinks were Reb A extracts abundant.	(Kakigi *et al.* 2013)
Stevioside and Rebaudioside A	*Stevia* leaves	Ultrahigh performance liquid chromatography–tandem mass spectrometry (UHPLC-MS)	Isocratic elution of 50 % 10 mM aqueous ammonium acetate and 50 % Acetonitrile	QTRAP 3200 mass spectrometer (AB/Sciex) equipped with SIL-HTc column oven	LOD_{Stv} = 5.7 ng/mL LOQ_{Stv} = 19.1 ng/mL $LOD_{Reb\ A}$ = 5.0 ng/mL $LOQ_{Reb\ A}$ = 16.8 ng/mL	(Shafii *et al.* 2012)
Oligosaccharides, nucleic acid bases, and nucleosides	N/A	Hydrophilic interaction liquid chromatography (HILIC) mode, and FTIR	Mobile phase H2O/ACN at 50/50 (v/v).	Rebaudioside A immobilized on silica surface through “thiol-ene” click chemistry (Click TE-Reb A) Column, Waters 2998 diode array detector (DAD)	This was a qualitative study, developed and characterized Reb A stationary phase showed selectivity and efficient RT for polar compounds.	(Liang *et al.* 2015)
Rebaudioside A and Stevioside	*Stevia* leaves and	Ultra-high-performance liquid chromatography	isocratic with 5 mmol/L ammonium	A 1.8 µm HSS C18 column (100mm×2.1mm, Waters),	$LOD_{Reb\ A}$ = 0.1-10 µg/mL LOD_{Stv} = 0.05-10 µg/mL	(Gardana *et al.* 2010)

	commercial sweetener.	coupled with electrospray ionization mass spectrometry (UHPLC-MS)	acetate pH 6: CH_3CN (45:55, v/v)			
Stevioside, rebaudioside A and rebaudioside C	*S. rebaudiana* leaves	Near-infrared reflectance spectroscopy (NIRS), using HPLC as a reference method	Isocratic elution using acetonitrile/water (80/20, v/v)	Zorbax NH2 column (5 mm, 250 mm ×4.6 mm), multiple UV wavelength detectors	Total combined concentration for the three main SGs ranged from 4.3–11.1% (w/w)	(Hearn and Subedi 2009)
Stevioside, Steviolbioside and Rebaudioside A	S. *rebaudiana* leaves	[a] [HPLC] and [b][LC-MS-ESI]	[a] & [b] [Isocratic elution using of acetonitrile: water (3:2)]	[a] [C_{18} column of size 25x4.6 mm] [b] [C18 Column (SGE, 25X1.6mm), Waters 2696 photodiode array detector (DAD)]	The content of Steviolbioside was 6.48% and Rebaudioside-A was 0.099% on a dry weight basis in *ex vitro* and *in vitro* leaves.	(Rajasekaran *et al.* 2008)
Stevioside and Rebaudioside A	*Stevia rebaudiana* Bertoni leaves	HPLC	Isocratic elution in Acetonitrile and Water (8: 2) and Gradient elution with many ramps.	Develosil ODSHG 140 Å (250 mm × 4.6 mm × i.d., 5 lm) and Luna HILIC (150 mm × 4.6 mm i.d., 5 lm) columns, DAD detector,	LOD_{Stv} = 1.07 mg/L LOQ_{Stv} = 3.55 mg/L $LOD_{Reb\ A}$ = 1.07 mg/L $LOQ_{Reb\ A}$ = 3.56 mg/L	(Lorenzo *et al.* 2014)

				was set at 210, 256, 330, 360 and 450 nm.		
Rebaudioside A and stevioside	Food products	Electrospray ionisation liquid chromatography-mass spectrometry	Gradient elution with mobile phase A consisted of 10mM NH4OAc in water/ACN (50/50 v/v), and mobile phase B consisted of 10mM NH4OAc in water/ACN (5/95 v/v)	Restek (Bellefonte, PA, USA) Pinnacle II Amino column with guard (100mm×2.1mm×3 mm, 110A˚), MS detector	The method had a limit of detection of 0.01–0.34 µg/g and repeatability at the limit of quantitation of 2%–15% relative standard deviation.	(Shah *et al.* 2012)
Major Steviol Glycosides (Stevioside and Rebaudioside A)	Plants of *Stevia rebaudiana* (Bertoni)	High-performance thin-layer chromatography (HPTLC) analysis	Ethyl acetate-ethanol-water (80:20:12, v/v/v)	Precoated silica gel HPTLC 60 F254 (20×10 cm) plate of 0.20 mm layer thickness.	This was a qualitative study that led to the cloning of seven genes of SGs biosynthesis pathway and analysed a total of fifteen genes in relation to SGs in *stevia.*	(Jaitak *et al.* 2009; Kumar *et al.* 2012)
Stevioside	Food samples	High-performance liquid chromatography (HPLC) coupled with	A buffer solution was prepared by dissolving 0.8 mL of	The spherical analytical column was packed with 5	The correlation coefficient of the calibration curve was	(Yang and Chen 2009)

		electrospray ionization mass spectrometric detection (ESI-MS)	formic acid and 1.5 mL of triethylamine in1Lof water. The HPLC mobile phase A was prepared by mixing methanol with buffer solution and acetone (69:24:7, v/v/v), whereas the HPLC mobile phase B was prepared by mixing methanol with buffer solution and acetone (11:82:7, v/v/v).	µm C_{18} silica (250 mm × 4.5 mm i.d.)	better than 0.998 (n) 6), in the range of 0.50 to 15.0 µg/mL for stevioside. LOD≤ 0.10 µg/mL LOQ≤ 0.30 µg/mL	
Stevioside	*Stevia rebaudiana* Bertoni	Thin-layer chromatography, high-performance liquid chromatography, and proton NMR	Gradient elution was performed using the mobile phase was a mixture of deionized water,	Luna NH2 column (250×4.6 mm, 5 mm), the UV detector was tuned to 210 nm.	The lower concentration limit for stevioside detection in the samples was 0.1 g/l	(Kedik *et al.* 2003)

			pH 5.5 (A) and acetonitrile (B).			
Rebaudioside A	*Stevia Rebaudiana* Bertoni crude extracts.	Macro-porous adsorption resin (MAR) and high-performance liquid chromatography (HPLC)	Acetonitrile (A)-70% and potassium dihydrogen phosphate (10 mM) (B)-30% was used as the mobile phase.	MAR mixed bed of HPD750–LSA40–LSA30–DS40. NH2 column (AT LICHROM, 150 × 4.6 mm, 5 lm), with 210 nm DAD detector wavelength.	Under the optimal conditions, the separation degree for RA (DAS) increased from 0.771 to 1.54. The study also improved the purity of the extracted Reb A from 60 % to 97 %.	(Li *et al.* 2012)
Diterpene glycosides	*Stevia* leaves	Desorption electrospray ionization (DESI) mass spectrometry.	The solvent used in this study was MeOH: H2O (1: 1).	A 3 mL sample (stevia) of the commercial sample (1 mg/mL made up in MeOH: H2O (1: 1); 3 mg absolute amount) was spotted onto a porous Teflon substrate.	The compounds observed included: steviolbioside/rubusoside (isomers), m/z 641 $(M-H)^-$ and 677 $(M+Cl)^-$; Dulcoside, A m/z 787 $(M-H)^-$; stevioside/rebaudioside B (isomers), m/z 803 $(M-H)^-$ and 839 $(M+Cl)^-$; rebaudioside C, m/z 949 $(M-H)^-$ 985 $(M+Cl)^-$;	(Jackson *et al.* 2009)

rebaudioside A/E (isomers), m/z 965 $(M-H)^-$ and 1001 $(M+Cl)^-$.

APPENDIX B : TABLE : A SUMMARY OF ANTIBODIES EMPLOYED IN ELECTROCHEMISTRY FOR DEVELOPMENT OF IMMUNOSENSORS

Target analyte	Molecular recognition element (Antibody)	Detection and Quantification limit	[Ref]
four umami ligands (sodium glutamate (MSG), disodium inosinate (IMP), disodium guanylate (GMP), and disodium succinate (SUC))	human umami receptor hT1R1	The sensing ability towards umami ligands was in the order: GMP > MSG > IMP > SUC	(Huang *et al.* 2019)
goat anti-biotin IgG	anti-biotin IgG	The detection range of this immunosensing scheme is between 0.1 and 30 µg/mL	(Kwon *et al.* 2006)
anti-tTG antibody	tissue transglutaminase (tTG)	The detection limit was 0.5 ng/mL	(Habtamu *et al.* 2015)
ochratoxin A (OTA)	anti-OTA monoclonal antibody	The detection limits were 0.05-2.5 and 0.1-7.5 µg/L, for direct and indirect immunoassay formats.	(Alarcón *et al.* 2006)

prostate protein antigen (PSA), a biomarker of prostatic cancer	glucose oxidase (GOx)	The developed method had a detection limit of 0.0012 ng/mL	(Li *et al.* 2014)
thyroid stimulating hormone (TSH).	thyroid stimulating hormone antibody (anti-TSH) o	The determination had a detection limit of 0.1 ± 0.02 ng/mL.	(Beitollahi *et al.* 2018)
mycotoxin ochratoxin A	anti-OTA-McAb	The immunosensor had a LOD of 2.04 fg/ml	(Hou *et al.* 2019)

APPENDIX C: TABLE: BITTERNESS TESTING OF DIFFERENT SGS AGAINST TASTE RECEPTOR (T1R2) IN HUMAN

Steviol Glycosides	Dock score of T1R2 (D1)/(kcal/mol)	Chemical structure of Steviol Glycoside
Rebaudioside A	-12.334	

Molecular formula & molar mass: $C_{44}H_{70}O_{23}$ and 967,01g/mol.

Solubility: high solubility in water

Appearance: white powder

Application: Reb A has a high-intensity sweetener and because of its high solubility in water, finds its widespread application in food science.

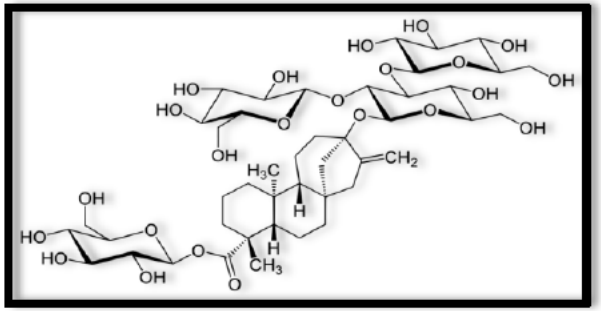

Rebaudioside E -10.658

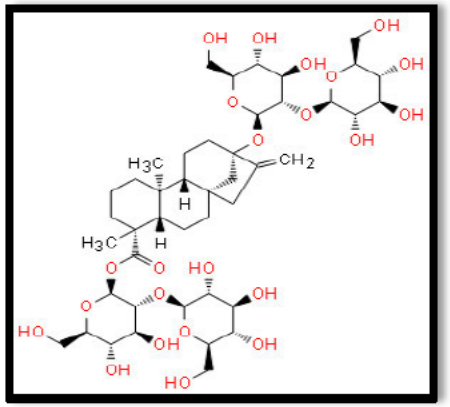

Molecular formula & molar mass:

Solubility:

Appearance:

Rebaudioside D -9.764

Molecular formula & molar mass: $C_{50}H_{80}O_{28}$ &

Solubility: Poor solubility in water

Appearance: powder in physical appearance

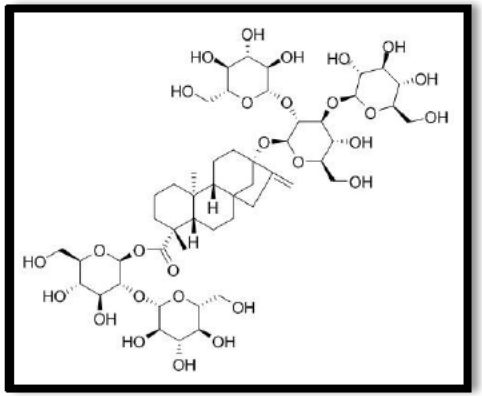

Rebaudioside B -9.100

Molecular formula & molar mass: $C_{38}H_{60}O_{18}$ & 804.87 g/mol

Solubility:

Appearance: powder

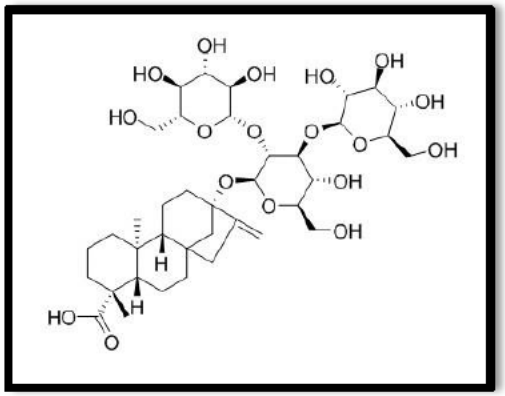

Stevioside -9.711

Molecular formula & molar mass: $C_{38}H_{60}O_{18}$ & 804.87 g/mol

Solubility: high solubility in water

Appearance: white powder

Application: Stevioside is the most abundant SG from stevia, although it has limited application in food due to its bitter aftertaste. High doses of Stevioside are used in the treatment of hypertension and type 2 diabetes.

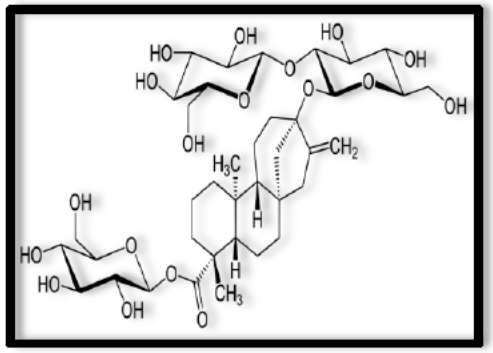

Steviolbioside -8.096

Molecular formula & molar mass: $C_{32}H_{50}O_{13}$ & 642.73 g/mol

Solubility:

Appearance:

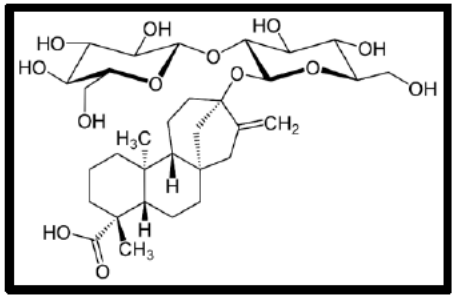

Dulcoside A -6.910

Molecular formula & molar mass: $C_{38}H_{60}O_{17}$ & 788.87 g/mol

Solubility:

Appearance:

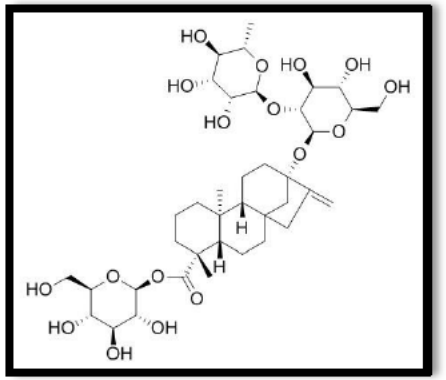

Isosteviol -4.198

Molecular formula & molar mass: $C_{20}H_{20}O_3$ & 318.45 g/mol

Solubility:

Appearance: White to faint beige powder to crystals

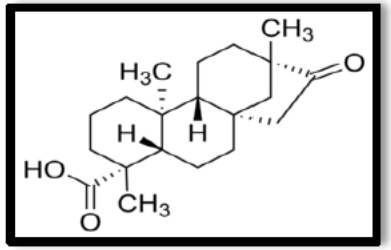

Steviol -3.426

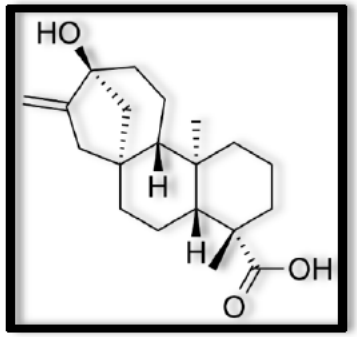

Molecular formula & molar mass: $C_{20}H_{30}O_3$ & 318.46 g/mol.

Solubility:

Appearance: